



**US Army Corps of Engineers®**  
 Engineer Research and Development Center



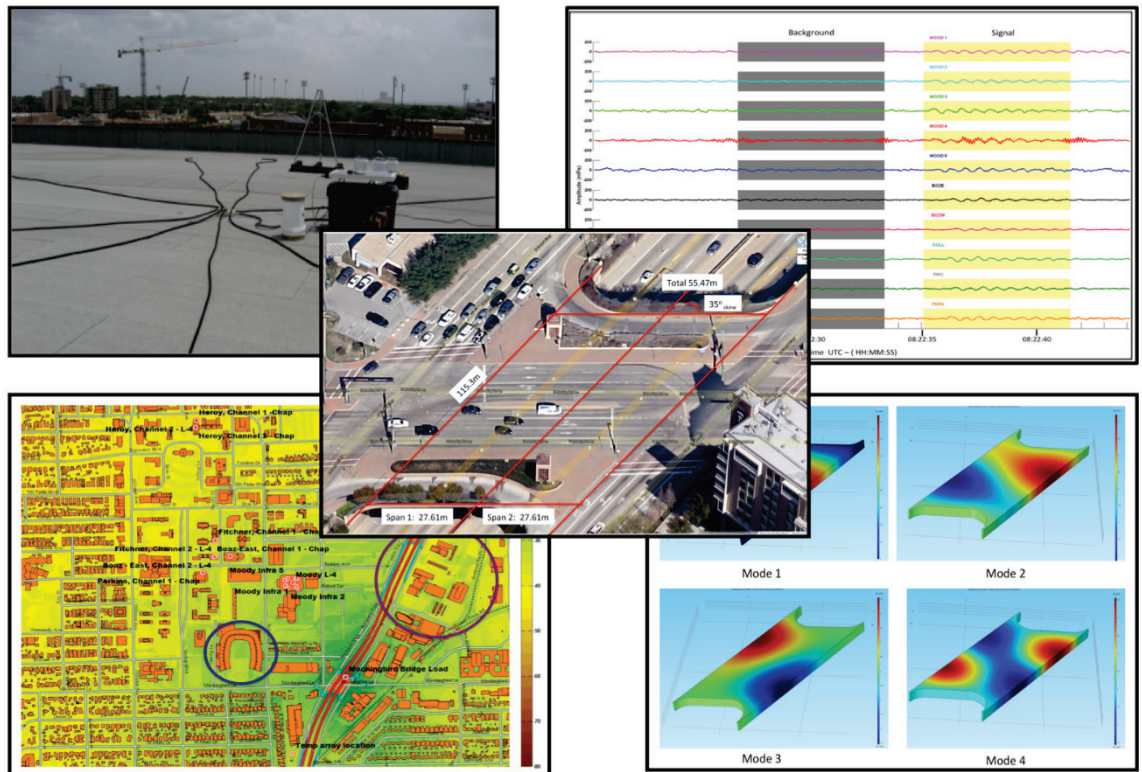
*Remote Assessment of Critical Infrastructure*

# Persistent Monitoring of Urban Infrasound Phenomenology

Report 2: Investigation of Structural Infrasound Signals in an Urban Environment

Sarah L. McComas, Michael E. Pace, Henry Diaz-Alvarez, Chris Simpson, and Mihan H. McKenna

November 2016



**The U.S. Army Engineer Research and Development Center (ERDC)** solves the nation's toughest engineering and environmental challenges. ERDC develops innovative solutions in civil and military engineering, geospatial sciences, water resources, and environmental sciences for the Army, the Department of Defense, civilian agencies, and our nation's public good. Find out more at [www.erdclibrary.usace.army.mil](http://www.erdclibrary.usace.army.mil).

To search for other technical reports published by ERDC, visit the ERDC online library at <http://acwc.sdp.sirsi.net/client/default>.

# **Persistent Monitoring of Urban Infrasound Phenomenology**

## **Report 2: Investigation of Structural Infrasound Signals in an Urban Environment**

Sarah L. McComas, Henry Diaz-Alvarez, Chris Simpson, and Mihan H. McKenna

*Geotechnical and Structures Laboratory  
U.S. Army Engineer Research and Development Center  
3909 Halls Ferry Road  
Vicksburg, MS 39180-6199*

Michael E. Pace

*Information Technology Laboratory  
U.S. Army Engineer Research and Development Center  
3909 Halls Ferry Road  
Vicksburg, MS 39180-6199*

Report 2 of a series

Approved for public release; distribution is unlimited.

Prepared for Headquarters, U.S. Army Corps of Engineers  
Washington, DC 20314-1000

Under ERDC, Military Engineering, Remote Assessment of Critical Infrastructure  
Project Number 451182

## Abstract

Historically, infrasound arrays have been deployed in rural environments where anthropological noise sources are limited. As interest in monitoring sources at local distances grows in the infrasound community, it is vital to understand how to monitor infrasound sources in an urban environment. Arrays deployed in urban centers have to overcome the decreased signal-to-noise ratio and the reduced amount of real estate available to deploy an array. To advance the understanding of monitoring infrasound sources in urban environments, local and regional infrasound arrays were deployed on rooftops of the campus of Southern Methodist University (SMU) to collect data for one seasonal cycle. The data were evaluated for structural source signals (continuous-wave packets). When a signal was identified, the back azimuth to the source was determined through frequency wavenumber analysis. This information was used to identify hypothesized structural sources; these sources were verified through direct measurement followed by structural numerical modeling. Wave propagation modeling was completed to understand how the urban infrastructure affects infrasound propagation by tying the direct source measurements to the original infrasound observations. The wave propagation study was focused on a single season. This study demonstrated that infrasound arrays deployed in urban environments could detect structural sources with success.

**DISCLAIMER:** The contents of this report are not to be used for advertising, publication, or promotional purposes. Citation of trade names does not constitute an official endorsement or approval of the use of such commercial products. All product names and trademarks cited are the property of their respective owners. The findings of this report are not to be construed as an official Department of the Army position unless so designated by other authorized documents.

**DESTROY THIS REPORT WHEN NO LONGER NEEDED. DO NOT RETURN IT TO THE ORIGINATOR.**

# Contents

<b>Abstract .....</b>	<b>ii</b>
<b>Figures and Tables.....</b>	<b>v</b>
<b>Preface.....</b>	<b>ix</b>
<b>Unit Conversion Factors .....</b>	<b>x</b>
<b>List of Abbreviations.....</b>	<b>xi</b>
<b>1 Introduction.....</b>	<b>1</b>
1.1 Global infrasound monitoring .....	2
1.2 Regional infrasound monitoring .....	3
1.3 Local infrasound monitoring .....	3
<b>2 Problem Statement .....</b>	<b>4</b>
2.1 Infrasound in urban environments.....	4
2.2 Historical examples of structural monitoring with infrasound .....	4
2.3 Challenges .....	4
2.4 Motivation .....	5
<b>3 Research Methodology.....</b>	<b>7</b>
3.1 Data collection.....	7
3.1.1 <i>Deployment method</i> .....	7
3.1.2 <i>Rooftop arrays</i> .....	7
3.2 Structural sources .....	12
3.2.1 <i>Identifications and characterization</i> .....	12
3.2.2 <i>Array impulse responses</i> .....	14
3.2.3 <i>Source confirmation</i> .....	17
3.3 Wave propagation study.....	18
<b>4 Results .....</b>	<b>20</b>
4.1 Summary of detections .....	20
4.2 Mockingbird Bridge case study.....	26
4.2.1 <i>Mockingbird Bridge – acoustic model</i> .....	29
4.2.2 <i>Mockingbird Bridge – direct source measurement</i> .....	34
4.3 Lovers Lane case study.....	36
4.3.1 <i>Lovers Lane technical specifications</i> .....	36
4.3.2 <i>Lovers Lane – acoustic model</i> .....	38
4.4 Wave propagation study.....	40
4.4.1 <i>Simplified atmosphere</i> .....	42
4.4.2 <i>Realistic atmosphere</i> .....	51
<b>5 Conclusions and Implications .....</b>	<b>60</b>

---

5.1	Future work .....	60
5.1.1	<i>Rooftop arrays</i> .....	60
5.1.2	<i>Wave propagation study</i> .....	61
	<b>References .....</b>	<b>62</b>
	<b>Appendix A: Field Deployment Photographs .....</b>	<b>65</b>
	<b>Appendix B: Channel Map .....</b>	<b>75</b>
	<b>Appendix C: Detection Data .....</b>	<b>77</b>
	<b>Report Documentation Page</b>	

# Figures and Tables

## Figures

Figure 1. Overview of Southern Methodist University campus rooftop arrays. Each yellow pushpin indicates the location of individual array elements.....	8
Figure 2. A view of the inside of one instrumentation box that includes batteries, digitizer, radio, and Chaparral sensor. This type of instrumentation box was installed on each rooftop site. Moody's instrumentation box was deployed with the Chaparral sensors outside the box. ....	9
Figure 3. Photograph of Moody rooftop array. Highlights include the roof infrastructure, roof vents and the raised edge, which could create a complex noise environment for the array.....	10
Figure 4. Photographs of the multi-rooftop array. Highlights include the roof infrastructure, roof vents and raised edges, which could create a complex noise environment for the array.....	11
Figure 5. Photograph of the Heroy rooftop array. Highlights include the roof infrastructure, roof vents and raised edges, which could create a complex noise environment for the array. <i>Heroy - 1</i> is the hose array for the infrasound sensor on channel 1 and solar panel and GPS for the Heroy array. <i>Heroy - 2</i> is the hose array and manifold for the infrasound sensor on channel 2. <i>Heroy - Seismic</i> is the seismic sensor located under the yellow upside down drink cooler. ....	12
Figure 6. Example of packetized signal highlighted in grey. In the grey section the signal is coherent across the three channels of data. Data example from a single array, which observed the Pratt Truss Bridge (McKenna et al 2009a).....	13
Figure 7. Multi-rooftop array impulse response. ....	15
Figure 8. Moody array impulse response.....	16
Figure 9. Summary of all detections in Table 1 in comparison to back azimuth to source. The circumference axis is the back-azimuth to source in degrees and the radial axis is number of detections. The maximum number of detections is from the Mockingbird Bridge with the Moody array between azimuth 150° and 155° and the multi-rooftop array at 130° .....	22
Figure 10. Summary of limited detections in Table 1 in comparison to back azimuth to source by removing the main azimuths associated with the Mockingbird Bridge for each array (Moody 150°-170° and multi-rooftop 130°-145°). This allows investigation of local detection maxima. The circumference axis is the back azimuth to source in degrees and the radial axis is number of detections. The maximum number of detections are from the Mockingbird Bridge with the Moody array between azimuth 135° and the multi-rooftop array at 125°. Other local maxima are Moody at 200°- 205°, Moody and multi-rooftop at 230°- 240°, Moody and multi-rooftop at 290° and Moody at 340° .....	23
Figure 11. Comparison of wind direction effect on observations of Mockingbird Bridge signal. The data that populate the chart are from Table 3. The circumference axis is the wind direction in degrees, and the radial axis is number of detections. Southerly winds appear to provide a slight increased detection capability for the rooftop arrays. ....	25
Figure 12. Comparison of number of detections from Mockingbird Bridge to wind speed, which shows limited effect. Table 3, provides data to populate this chart. ....	25
Figure 13. Comparison of number of detections, wind speeds and wind directions. ....	26

Figure 14. Examples of signal and background time series. The signal azimuth from array to source was between 132° and 137°. The light yellow window highlights the signal of interest and the dark grey window highlights background noise. Each different color trace indicates a different array element.....	27
Figure 15. A comparison of the background noise (red) and signal (black) FT of the example time series in Figure 14. The grey box highlights a frequency peak at 1.6 Hz, that is seen in the signal FT and not background noise FT.....	28
Figure 16. Overview map highlighting hypothesized source Mockingbird Bridge between crossing azimuths from the multi-rooftop array (blue lines) and Moody array (red lines). Green squares are infrasound sensor positions, blue lines are azimuth lines 130° and 145°, and red lines are azimuth lines 147° and 168°.....	28
Figure 17. Aerial imagery of the Mockingbird Bridge from Google Earth. The red lines highlight the main structural supports of the bridge.....	29
Figure 18. A cross-section view of the Mockingbird Bridge deck. The orange sections highlight the structural features that allow the bridge deck to act as a monolithic structure (TX DOT 1993). .....	30
Figure 19. A Google street view of the Mockingbird Bridge driving north on I-75. The red highlights the confined air, which is the model space. ....	30
Figure 20. Pressure acoustic model. The warmer the color the greater the pressure on the surface.....	32
Figure 21. The first four vibrational modes at each monthly average low (upper) and high (lower) temperature. ....	33
Figure 22. Overview map of the direct source measurement sensor deployment. Each green marker is a location of a vertical seismometer.....	34
Figure 23. Example of background noise.....	35
Figure 24. Example of traffic signal.....	36
Figure 25. Map that highlights the relationship of Lovers Lane Bridge to the rooftop arrays, which is located 1.57 km at an azimuth of 47° from North. Green squares highlight infrasound sensor position and the red line is the 47° line of azimuth.....	37
Figure 26. Size comparison between Lovers Lane Bridge and Mockingbird Bridge. The area of the Mockingbird Bridge is 24% greater than the area of the Lovers Lane Bridge.....	38
Figure 27. Pressure acoustic model of Lovers Lane Bridge. The warmer the color, the greater pressure on the surface. ....	39
Figure 28. Narrow bandpass (BP) filter example for rooftop array data, which demonstrates the targeted data processing use to identify the Lovers Lane Bridge. Data processing specifications – bandpass filter: 8.1 - 8.3 Hz, window size: 40 min; Results – F-K analysis, azimuth: 57°, apparent velocity: .484 km/s. ....	40
Figure 29. Overview map of model area. Green, purple and yellow circles mark array locations, pink rectangle marks source location, and orange color marks building locations. ....	41
Figure 30. Upper-half of figure compares model output to Google Maps Street View. Comparison of roof heights and shapes are similar. Lower half of figure is a representative photograph of the 3-D terrain developed over the model space.....	42
Figure 31. Example of model input source. Pictured is a 10-Hz center frequency Ricker Pulse source.....	43
Figure 32. Peak pressure maps; Source Location: Center. Right: 10-Hz Source, Left: 5-Hz Source. Color scale – db relative to 1 Pa.....	46

Figure 33. Peak pressure maps; Source Location: Southwest. Right: 10-Hz Source, Left: 5-Hz Source. Color scale - db relative to 1 Pa. ....46

Figure 34. Peak pressure maps; Source Location: Southeast. Right: 10-Hz Source, Left: 5-Hz Source. Color scale - db relative to 1 Pa. ....47

Figure 35. Peak pressure maps; Source Location: Northwest. Right: 10-Hz Source, Left: 5-Hz Source. Color scale - db relative to 1 Pa. ....47

Figure 36. Peak pressure maps; Source Location: Northeast. Right: 10-Hz Source, Left: 5-Hz Source. Color scale - db relative to 1 Pa. ....48

Figure 37. Input source to wave propagation model is a Ricker pulse with a 1.66 Hz center frequency. ....49

Figure 38. Model output time series and power spectrum for each building in the urban array. ....50

Figure 39. Peak pressure output over model space zoomed to study area. Color bar is dB relative to 1 Pa. The purple circle highlights a shadow zone from a high-rise building. The blue circle highlights a reflection/amplification zone from the SMU football stadium. ....51

Figure 40. Effective sound speed (temperature only) plots that were averaged hours for five days between 7/1/13 0:00 and 7/5/13 UTC (6/30/13 18:00 to 7/5/13 17:00 CST). The ground measurement is provided by the Love Field Airport metrological station and the upper points are provided by NOAA RUC data sets. ....53

Figure 41. Effective sound speed (temperature only) plots that were averaged hours for five days between 7/1/13 0:00 and 7/5/13 UTC (6/30/13 18:00 to 7/5/13 17:00 CST). The ground measurement is provided by the Love Field Airport metrological station and the upper points are provided by NOAA RUC data sets. ....54

Figure 42. Peak pressure output over model with simplified atmosphere. ....55

Figure 43. Peak pressure output over model with realistic atmosphere. ....56

Figure 44. Peak pressure difference between the simplified atmosphere model and the realistic atmosphere model relative to the simplified model. ....57

Figure 45. A cross-section view of the peak pressure difference between the simplified atmosphere model and the realistic atmosphere model; relative to the simplified model. The 0-m location is the northeast corner of the model and the 2,500-m location is the southeast corner of the model. ....58

Figure 46. A cross-section view of the peak pressure difference between the simplified atmosphere model and the realistic atmosphere model; relative to the simplified model. The 0-m location is the northeast corner of the model and the 2,500-m location is the northwest corner of the model. ....58

Figure A1. Overview map for array deployment sites, highlighting building names. ....65

Figure A2. Moody array - Channel 1. ....66

Figure A3. Moody array - Channel 2. ....67

Figure A4. Moody array - Channel 3. ....68

Figure A5. Moody array - Channel 4. ....69

Figure A6. Moody array - Channel 5. ....70

Figure A7. Multi-rooftop array at Perkins Hall. ....71

Figure A8. Multi-rooftop array at Boaz Hall. ....72

Figure A9. Multi-rooftop array Collins Hall. ....73

Figure A10. Multi-rooftop array at Finchner Hall. ....74

## Tables

Table 1. Summary of all detections recorded on rooftop arrays. Signal type: Continuous Wave (CW) and Impulsive (IMP). .....	21
Table 2. Potential other source azimuths observed in data; repeated azimuths in detection data when binned to five-degree bins.....	23
Table 3. Selected days analyzed with number of detections marked for the Mockingbird Bridge combined with the wind speed and direction on the selected days (Wunderground.com 2012). .....	24
Table 4. The four main vibrational modes identified from the acoustic model of the Mockingbird Bridge. ....	31
Table 5. Average high and low temperatures for each month in Dallas, Texas (Intellicast.com 2014).....	32
Table 6. The four main vibrational modes identified from the acoustic model of the Lovers Lane Bridge. ....	39
Table 7. The simple atmospheric profile used in the propagation model. ....	43
Table 8. The limiting factors for bounding frequency analysis of the simple atmosphere model. ....	45
Table 9. The limiting factors for bounding frequency analysis of the realistic atmosphere model. ....	54
Table B1. Rooftop array installation locations and the channel map for each array elements.....	76
Table C1. Detection data from rooftop arrays. ....	78

## Preface

This study was conducted for the Office of the Assistant Secretary of the Army for Acquisition, Logistics, and Technology (ASAALT) under Project “Infrasound Distribution and Monitoring in Man-Made Environments” and “Remote Assessment of Critical Infrastructure.” The technical monitor was Military Engineering.

The work was performed by the Structural Engineering Branch (StEB) of the Geosciences and Structures Division (GSD), U.S. Army Engineer Research and Development Center, Geotechnical and Structures Laboratory (ERDC-GSL). Southern Methodist University researchers Dr. Chris Hayward, Dr. Paul Golden, Art Ender, and Jesse Howard supported the research, and Ashley Shugart reviewed the data. At the time of publication, Charles W. Ertle was Chief, StEB; James L. Davis was Chief, GSD; and Pamela G. Kinnebrew was the Technical Director for Military Engineering. The Deputy Director of ERDC-GSL was Dr. William P. Grogan and the Director was Bartley P. Durst.

COL Bryan S. Green was the Commander of ERDC, and Dr. Jeffery P. Holland was the Director.

## Unit Conversion Factors

Multiply	By	To Obtain
atmosphere (standard)	101.325	kilopascals
bars	100	kilopascals
degrees Fahrenheit	$(F-32)/1.8$	degrees Celsius
feet	0.3048	meters
inches	0.0254	meters
yards	0.9144	meters

## List of Abbreviations

Comprehensive Test Band Treaty	CTBT
Finite-Element Model	FEM
Fourier Transform	FT
Frequency Wavenumber analysis	F-K
Geotechnical and Structures Laboratory	GSL
Global Positioning System	GPS
Hertz	Hz
Information and Technology Laboratory	ITL
Kilometer	km
Light Detection and Ranging	LIDAR
Meter	m
Parallel Stair-casing TOPography in 3D	PSTOP3D
Southern Methodist University	SMU
Signal to Noise Ratio	SNR
Three-Dimensional	3-D
United States Army Engineer Research and Development Center	U.S. Army ERDC

# 1 Introduction

Infrasound signals are acoustic signals below 20 Hz and can be monitored at distances of tens to thousands of kilometers (Hedlin et al. 2012). These signals are generated by natural sources (surf, earthquakes, volcanoes, etc.), explosions (nuclear and non-nuclear), infrastructure sources (bridges, dams, large buildings, etc.), and other human sources (trains, highway traffic, etc.) (Campus and Christie 2010; McKenna et al. 2009a; Guzas and Tricys 2010). The source type as well as the signal propagation medium has an effect on the propagation distance and signal characteristics seen at the receiver; for infrasound, this medium is the atmosphere. The atmosphere has four main layers, troposphere (0 – 12 km), stratosphere (12 – 50 km), mesosphere (50 – 80 km), and thermo-sphere (80 – 320 km). The effective sound speed profile through a layered atmosphere,  $C_{eff}$ , is controlled by the temperature profile, wind speed and wind direction (McKisic 1997). These parameters control infrasound signal propagation with a signal initially propagating upward until it reaches a higher effective sound speed than the origin, at which point the signal turns and returns to the earth. This return is conscribed by the atmospheric layer where the signal turns.

$$C_{eff} = C_t + \mathbf{n} \cdot \mathbf{v} \quad (1)$$

$$C_t \sim 20.07\sqrt{T}$$

where

$T$  = absolute temperature (°K)

$\mathbf{n} \cdot \mathbf{v}$  = component of wind speed in the direction of propagation

Infrasound signal propagation depends on atmospheric conditions. Direct measurement of the weather provides insight to the conditions in the lower atmosphere (0 – 30 km) and atmospheric models provide insight in the upper atmosphere (30 – 320 km) conditions. In the lower atmosphere layers (troposphere and lower stratosphere), these conditions are considered local, dynamic weather. One current method for collecting these weather parameters is through radiosonde measurements. These measurements can be taken at regular intervals near the source or receiver locations

or through ground weather stations. The upper atmosphere (upper stratosphere, mesosphere, and thermosphere) is less time variant than the lower atmosphere. The variations are driven by solar heating and diurnal/semidiurnal tides with predictable seasonal variation. Since these upper atmospheric features are predictable, they can be well characterized with statistical climatology models of the atmosphere, such as the Mass Spectrometer Incoherent Scatter/Horizontal Wind Model (MSIS/HWM). The Naval Research Laboratory Ground to Space (NRL-G2S) models produce a smoothed continuous atmospheric profile that fuses the lower atmosphere measurements and the upper atmosphere models (Drob et al. 2003; Hedlin et al. 2012; Picone et al. 2002).

Infrasound signals are optimally observed with an array of pressure sensors instead of a lone pressure sensor. An array of sensors takes advantage of the property that infrasound signals are coherent in time and space when sampled several wavelengths apart as compared to the incoherent non-acoustic pressure fluctuations (e.g., wind noise) typical of background noise (Bedard and Georges 2000). Array processing techniques can improve signal-to-noise ratio and provide back azimuth to source location. Given the variety of sources that generate infrasound, sets of array designs and detection ranges can be grouped into three main types of applications identified in the literature (i.e., global, regional, and local) (Arrowsmith and ReVelle 2007).

## **1.1 Global infrasound monitoring**

The International Monitoring System (IMS) takes advantage of the long periods and wavelengths expected during nuclear tests (underground: ~1 – 20 Hz, typically below 10 Hz and atmospheric: 0.002 – 20 Hz, typically below 10 Hz) with stations deployed around the globe to monitor these large-scale events (Campus and Christie 2010). These tele-infrasonic sources (>1000 km) are often composed of stratospheric and thermospheric returns (McKenna et al. 2007). The IMS, under the Comprehensive Nuclear-Test-Ban Treaty (CTBT), has designed a global-scale infrasound network to monitor and locate nuclear tests around the globe. The network contains 60 infrasound stations, 170 seismic stations, 11 hydroacoustic stations, and 80 radionuclide stations distributed evenly over the globe. Each infrasound station has an infrasound array with an aperture of 1 to 3 km with 4 to 8 elements sampled at 20 Hz.

## 1.2 Regional infrasound monitoring

Regional infrasound signals are in the classical infrasound frequency range (0.1 to 20 Hz) with a monitoring distance range between 100 km and 1,000 km. Observations at these distances include tropospheric, stratospheric or thermospheric returns (McKenna et al. 2008). The propagation is controlled by stable stratospheric or thermospheric atmosphere conditions as well as smaller-scale waveguides in the troposphere that may be predicted through modeling. Arrays designed for sources at these distances have a smaller aperture, down to approximately 100 m, as a result of the higher frequency content of the signals.

## 1.3 Local infrasound monitoring

Local infrasound signals extend from the infrasound frequency space, below 20 Hz, to the lower limits of acoustics frequency space, 100 Hz, which can be monitored at ranges of 0 to 100 km (Stubbs et al. 2005). These arrivals are dominated by tropospheric returns that propagate within the zone of silence (McKenna et al. 2012), a region in which geometrical ray paths are not predicted through climatological atmospheric models. Low-altitude turning ducts allow for the propagation of signals within the zone of silence and are expected to be affected by local weather conditions and terrain along the source-to-receiver propagation path. Modeling of these arrivals becomes increasingly more complex because of these effects. Array deployments for these distance and frequency ranges have small apertures (<60 m) in order to detect the short wavelengths of the higher frequencies. Arrays typically contain 3 to 5 elements and are sampled at a minimum of 200 Hz to capture the higher frequency content.

## **2 Problem Statement**

### **2.1 Infrasound in urban environments**

Historical observations indicate that urban environments are rich with infrasonic signals (Bedard 2000). Infrasound arrays can be deployed in the noisy urban environment to monitor structures (bridges or buildings) within the environment. Source generation mechanisms, propagation path effects, and the ability to monitor specific sources in this environment are still not completely understood. During this study, techniques were developed for monitoring infrasound generated by structures in an urban environment to include characterization of structural source signals in the study area with focus on a single season.

### **2.2 Historical examples of structural monitoring with infrasound**

The first observation of an infrasound signal from a structure was a cantilever bridge detected at a distance of 3 km with a center frequency of 8.5 Hz (Donn 1974). The second example was a Pratt-Truss bridge observed at a distance of 27 km with a center frequency of 2 Hz, but included 6 Hz and 13 Hz (McKenna et al. 2009a). Both studies confirmed the observations with vibrational mode measurements at the source. It was hypothesized that the bridges were excited by wind rather than traffic. The studies indicated that continuous wave structural sources produced packets of signals that vary in duration based on fluctuations of the low atmosphere duct. This early work indicated success in monitoring bridges in rural environments. The next natural progression is to investigate monitoring bridges and other major structures in urban environments.

### **2.3 Challenges**

As noted, infrasound arrays have traditionally been deployed in rural areas. Deployment of arrays in urban areas can add complexities, such as an increased noise environment, the lack of appropriate real estate to deploy an array, and security considerations. Infrasound arrays have traditionally been deployed in low noise environments to optimize the signal-to-noise ratio (SNR), but in an urban environment, low-noise deployment areas are not always possible or feasible. There is a trade-off

between a low-noise environment and a good site for source detection. The second issue is the real estate constraint of the urban landscape. During the study, a novel instrumentation approach was taken to overcome this challenge. The arrays were deployed on building rooftops. The rooftop deployment improved the security of the array sites and made theft and vandalism of instrumentation more difficult. Theft and vandalism of instrumentation is a greater concern in urban settings as compared to the traditional rural deployments.

Beyond the challenges of deploying infrasound arrays in the urban environments, there are considerable propagation path effects in the lower atmosphere over urban centers often referred to as the Urban Heat Island Effect (Hidalgo et al. 2008). This effect is directly attributable to the abundance of heat absorbing materials in urban areas compared to rural areas, which leads to warmer urban areas in both the summer and winter (Hidalgo et al. 2008). This shift in temperature can produce microclimatic changes in the troposphere and thus affect the altitude of infrasound returns at local detection ranges. Long-term deployment of infrasound arrays in an urban environment provides an opportunity to quantify the effect of these microclimatic variations.

The information gained from this study can be used to develop techniques, tactics, and procedures for fielding arrays to overcome the challenges urban environments present.

## **2.4 Motivation**

Infrasound provides a basis to monitor structural sources remotely due to minimal signal attenuation at great distances (0 – 1000s km based on source), depending on the energy level and frequency content of the source. Researchers in this field are currently evaluating the use of infrasound to assess bridge foundation issues and overall health of the riverine environment (Taylor et al. 2013).

Scouring of bridge foundations during flood events is the number one cause of bridge failure according to the Federal Highway Administration (FHWA) (Taylor et al. 2013; Whitlow et al. 2013). Remotely monitoring for scour foundation events is important given that approximately 83 percent of the 608,000 bridges in the United States are built over waterways.

Limited methods are currently available for monitoring scour, such as either monitoring from the bridge itself or from instruments installed on a structure around the bridge. These systems do not offer a truly remote assessment capability compared to remote infrasound signals associated with the bridge structure.

Infrasound arrays have also been shown to be effective in detecting a barge collision with a bridge or changes in the river signal during a high water event (Jordan et al. 2013). This type of monitoring may provide remote assessment and tracking of activity in a riverine environment. The remote monitoring bridge foundations and river activity with infrasound is in its infancy, but as it matures, the urban infrasound research directly supports this research area. Since many urban centers are on major waterways, urban monitoring capability will be critical as an emerging capability.

Expanding infrasound structural monitoring capability beyond the rural environments will expand the applicability of this technology.

## **3 Research Methodology**

To advance the understanding of monitoring infrasound sources in urban environments, a year-long infrasound deployment was executed in an urban setting to determine the feasibility of detecting structural sources. The resulting data collected were analyzed for structural sources. When a potential source was identified, it was confirmed through direct measurements of the hypothesized source and numerical modeling of that source. Additionally, wave propagation modeling was performed to understand the effects of urban-scape on infrasound propagation.

### **3.1 Data collection**

#### **3.1.1 Deployment method**

Infrasound arrays deployed in an urban center have to overcome many unique challenges. Traditional infrasound arrays are fielded in places selected for ideal SNR levels and adequate real estate for the array size. Urban real estate is at a premium, and there is a tradeoff between signal level and noise level relative to the distance from an urban source. During this project, an investigation was completed of methods for fielding arrays on rooftops in urban centers, minimizing the array footprint and lowering risk of theft as a result of controlled access.

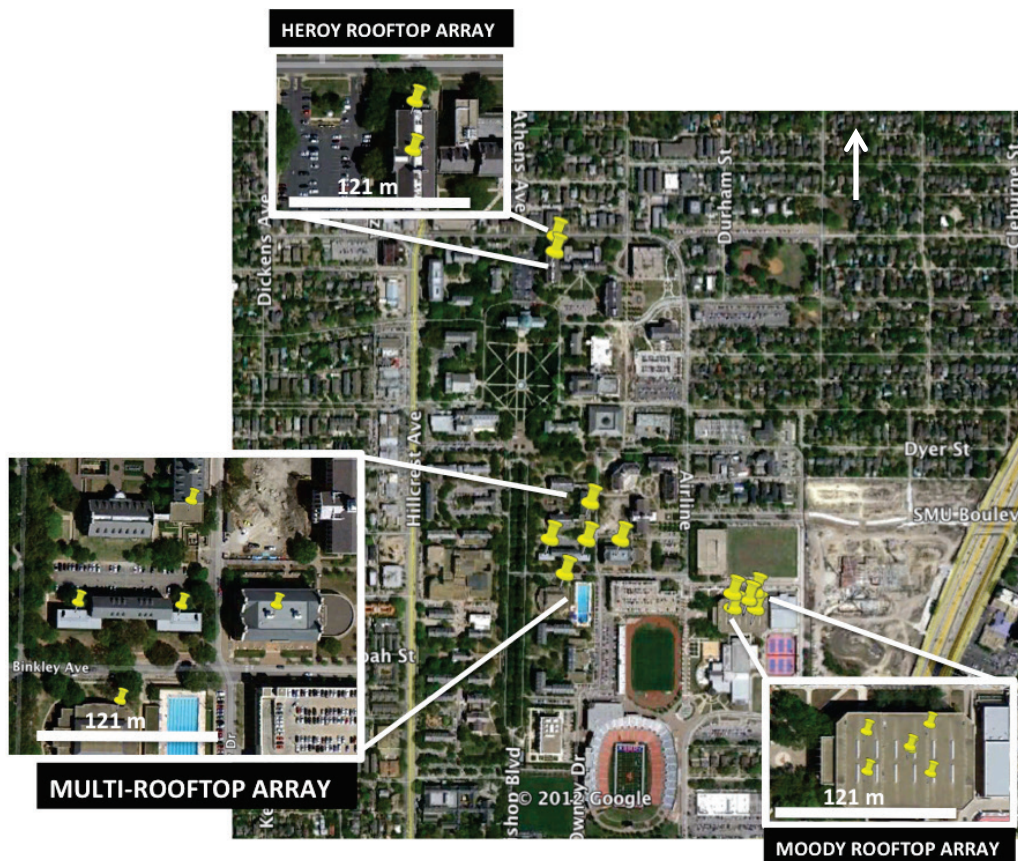
#### **3.1.2 Rooftop arrays**

From 28 June to 2 July 2012 under the Urban Infrasound Program, the U.S. Army Engineer Research and Development Center (ERDC) and Southern Methodist University (SMU) deployed three arrays (two local and one regional) on rooftops across the SMU campus, with finalization of telemetry on 2 July 2012 (Figure 1). The SMU campus is located approximately 4 km northeast of downtown Dallas, TX, is surrounded by houses, businesses, and light manufacturing in a heavily populated urban environment, and is in close proximity to a six-lane highway, light rail tracks, mid-rise buildings, and large bridges.

One array was five-element square with an aperture of 38 m located on a single rooftop, the Moody rooftop array. The second array was spread

across five rooftops with an aperture of 120 m, the multi-rooftop array. The third array was two-element line on a single rooftop with sensor separation of 30 m, the Heroy rooftop array. The Moody rooftop array was designed to monitor sources at local distances, the multi-rooftop array was designed to monitor sources at regional distances, and the Heroy stations could be combined with the other arrays to gain a larger aperture array for greater monitoring of lower frequency signals. Figure 1 contains an overview map of the array deployment sites highlighting building names. The Moody rooftop array was deployed from 2 July 2012 until 8 March 2013. Heroy and multi-rooftop arrays were deployed from 2 July 2012 until November 2013.

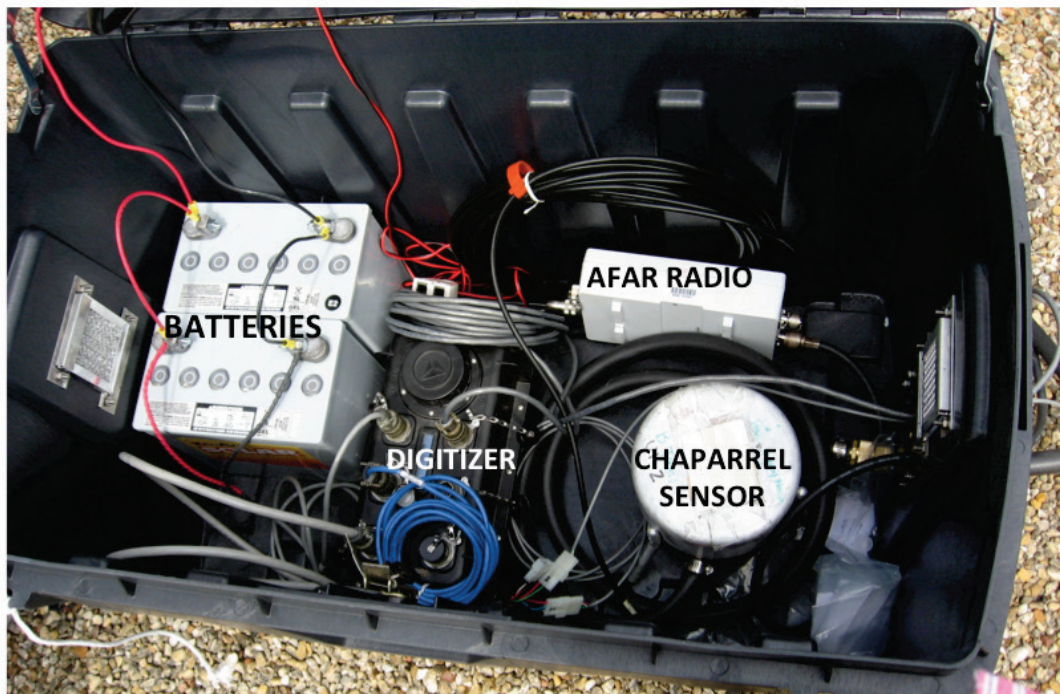
Figure 1. Overview of Southern Methodist University campus rooftop arrays. Each yellow pushpin indicates the location of individual array elements.



Each rooftop was instrumented utilizing a single instrumentation box that included the digitizer, radio, and Chaparral sensor, with the exception of the Moody array, where the Chaparral sensors were outside the instrumentation box. A typical instrumentation box is shown in Figure 2. Sensor output

was digitized by a Reftek 130 with 24-bit resolution. The raw data from each were real-time telemetered to SMU's data archive center over 2.4 GHz Wireless Afar radios with omni-directional antennas. At the data center, the raw data were converted to CSS 3.0 format and archived. Two data streams were collected from each digitizer, a 40 samples per second (SPS) stream and a 200 SPS stream, both at unity gain level. The data streams were synchronized in time with external GPS units connected to each digitizer.

Figure 2. A view of the inside of one instrumentation box that includes batteries, digitizer, radio, and Chaparral sensor. This type of instrumentation box was installed on each rooftop site. Moody's instrumentation box was deployed with the Chaparral sensors outside the box.



The Chaparral sensors were deployed with an incoherent wind noise filter. Each sensor was connected to a hose manifold with seven 7.62-m-long porous hoses laid out in a star pattern. The coherent signals are summed along the length of the hoses, but incoherent noise will destructively add along the length of the hoses (McKenna et al. 2011).

#### 3.1.2.1 *Moody rooftop array*

The Moody rooftop array was located on Moody Coliseum, SMU's basketball stadium, a large free span roof with multiple air vents. The roof is asphalt covered with tar and gravel. A photograph of the array installation is

in Figure 3 and contains five Chaparral 2.5 infrasound gauges with one Mark L-4 vertical seismometer. The five infrasound gauges were arranged in a 38-m aperture square with a center element. The center element (Moody 1) was collocated with the L-4 vertical seismometer.

Figure 3. Photograph of Moody rooftop array. Highlights include the roof infrastructure, roof vents and the raised edge, which could create a complex noise environment for the array.



### 3.1.2.2 Multi-rooftop array

Multiple building rooftops were used for this larger array configuration. Sensors were located on the rooftops of Perkins Natatorium, Boaz Hall East and West, Collins Hall, and Fincher Hall. Collins Hall and Boaz Hall East and West roofs are membrane type construction while the Perkins Natatorium and Fincher Hall roofs are asphalt covered with tar and gravel. The array installation is shown in Figure 4. This array consisted of a Chaparral 2.5 infrasound gauge and a Mark L-4 vertical seismometer on each of the rooftops. The sensors were arranged in a rectangular pattern with a center element, approximately 70 m on the short side and 120 m on the long side.

Figure 4. Photographs of the multi-rooftop array. Highlights include the roof infrastructure, roof vents and raised edges, which could create a complex noise environment for the array.



### 3.1.2.3 Heroy rooftop array

The Heroy array was deployed on the roof of the Heroy building as a test array for the subsequent rooftop deployments. The roof of this building is membrane type construction. The array installation is shown in Figure 5. This array has two Chaparral 2.5 infrasound gauges and a Mark L-4 vertical seismometer. The L-4 vertical seismometer was collocated with the northern most Chaparral gauge. The second Chaparral was located approximately 30 m south.

Full size images of the Moody and multi-rooftop array deployments are in Appendix A. The locations and channel map for each rooftop array element is documented in Appendix B.

Figure 5. Photograph of the Heroy rooftop array. Highlights include the roof infrastructure, roof vents and raised edges, which could create a complex noise environment for the array. *Heroy - 1* is the hose array for the infrasound sensor on channel 1 and solar panel and GPS for the Heroy array. *Heroy - 2* is the hose array and manifold for the infrasound sensor on channel 2. *Heroy - Seismic* is the seismic sensor located under the yellow upside down drink cooler.

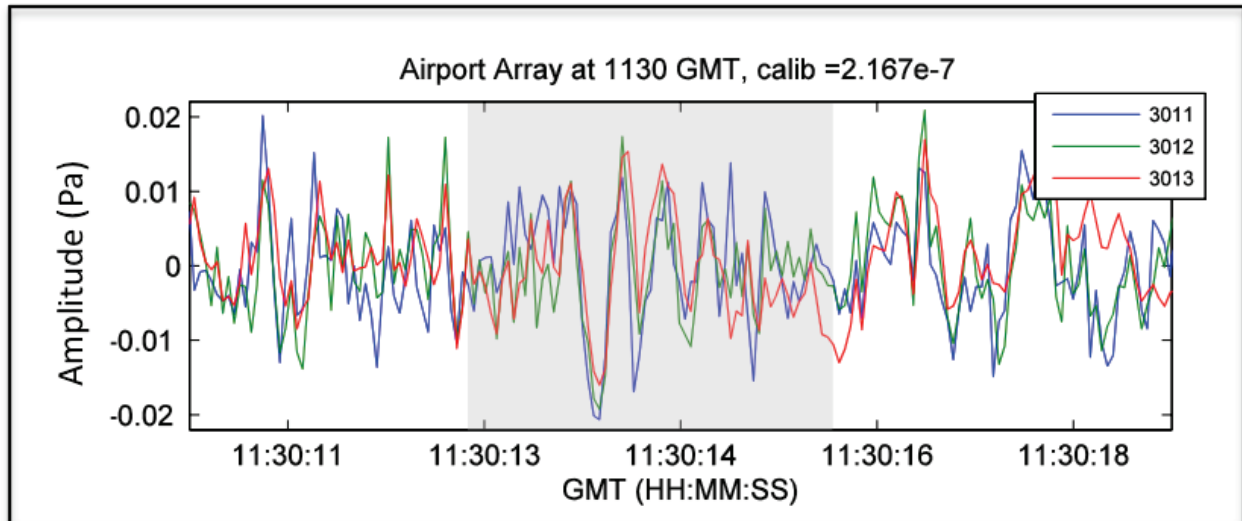


## 3.2 Structural sources

### 3.2.1 Identifications and characterization

Data were evaluated for structural sources using analyst review. This simple processing technique can be utilized in cases with unknown signatures. The first step is to filter the raw time series at the expected signal frequency range, then hand-process the data to identify the packetized/ “twinkling” signal of interest as documented in the historical literature (Donn 1974; McKenna et al. 2009a). An example of packetized signal is shown in Figure 6. After a signal is identified, signal characteristics are then captured to classify and document signals.

Figure 6. Example of packetized signal highlighted in grey. In the grey section the signal is coherent across the three channels of data. Data example from a single array, which observed the Pratt Truss Bridge (McKenna et al 2009a).



Once a signal of interest is identified, it is fully characterized for classification by identifying the frequency content, azimuth to source, Fisher-Statistic, and average Signal-to-Noise Ratio (SNR). Identification of frequency content of the signal is important for developing filters for subsequent data examination, including the development of automated detectors and identification of additional sources. The frequency content of the signal is determined by comparing the Fourier transform (FT) of the time window of the signal of interest and an equal size window over a noise segment close in time to the signal. This comparison provides the basis for quantifying the frequency content of the signal that is above background noise.

Estimation of the back azimuth to the source will be used to constrain the source location when combined with data from other arrays or knowledge of the travel-time of signals. The azimuth is calculated using frequency-wavenumber analysis (F-K analysis) (Rost and Thomas 2002). This method assumes an array collects a coherent signal across a minimum of three channels and has a small time delay between arrivals on different channels. If delays are too large, the time window for F-K analysis becomes too large, making it hard to match phases between signals. This analysis produces a contour plot with x and y components of slowness on the respective plot axes, and the contours indicate relative power. The back azimuth is

determined at the highest relative power with the approximate correct slowness for the expected return.

### 3.2.2 Array impulse responses

An array impulse response provides quantification of how the array layout (sensor position) will affect the response to a given signal, including frequency content and phase velocity across an array, highlighting the effects of spatial aliasing and array resolution. The array impulse response for each rooftop array (multi-rooftop array and Moody array) was calculated with a script developed in Matlab. This script was based on the equation for array transfer function from the *New manual of seismological observatory practice* – Chapter 9 “Seismic Arrays” (Schweitzer et al. 2011). The array transfer is calculated at each frequency point of interest, 0.1 Hz to 20 Hz incremented at 0.25 Hz, and then summed to determine the broadband impulse response.

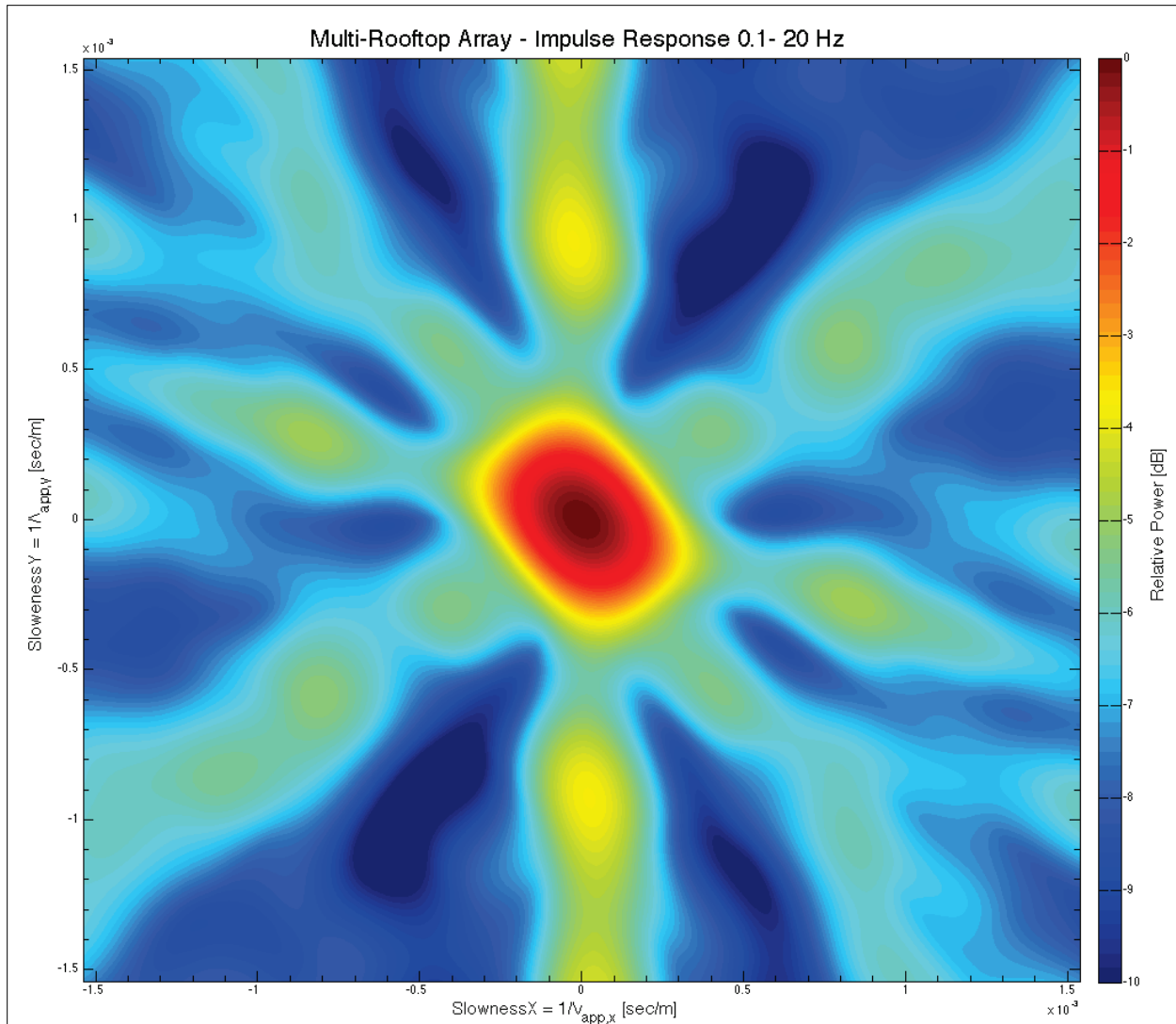
#### 3.2.2.1 Multi-rooftop array

The Multi-rooftop array response is skewed northwest/southeast, with a main lobe width in slowness  $S_x$  is  $3.1 \times 10^{-5}$  sec/m, and  $S_y$  is  $5.5 \times 10^{-4}$  sec/m at power level 1.2 dB (Figure 7). The increased main lobe width reduces the effectiveness to determine the slowness of signals from the Northwest/Southwest directions. Overall, the low power side lobes (side lobe ratio of 3.7 dB) allows for easier determination of the direction of signal. The upper limit of the wavelength that can best be analyzed with this array is 120 m, which is approximately 2. Hz.

#### 3.2.2.2 Moody array

The Moody array response is also skewed northwest/southeast, with a main lobe width in slowness  $S_x$  is  $9.5 \times 10^{-4}$  sec/m, and  $S_y$  is  $1.4 \times 10^{-3}$  sec/m at power level 1.2 dB (Figure 8). The wide main lobe will reduce the effectiveness of the array to discriminate between signals with similar slownesses and/or azimuths. Overall, the low power side lobes (side lobe ratio of 4.2 dB) allows for easier determination of signal direction. The upper limit of the wavelength that can best be analyzed with this array is 38 m, which is approximately 8.7 Hz.

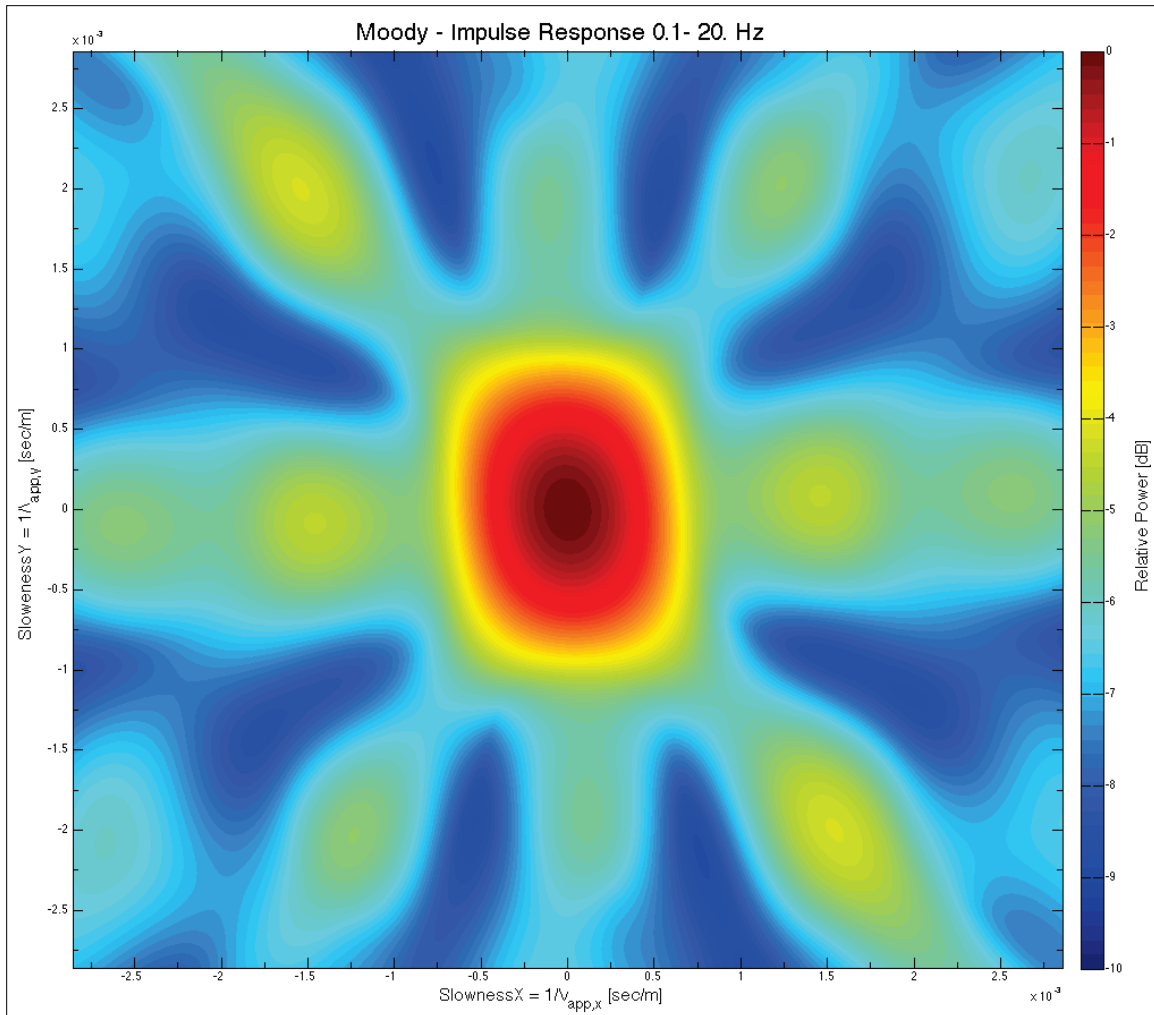
Figure 7. Multi-rooftop array impulse response.



### 3.2.2.3 Analyst review technique

Outlined is the simple analysis procedure used to identify structural sources in the data. Initial structural sources were highlighted in the raw infrasound data by filtering the data between 0.5 and 10 Hz using a 3-pole causal Butterworth filter. However, when later reviews of data were completed to target specific structures, the filter was adjusted to match a structural mode of interest (Donn 1974; Jacobs 2008; McKenna et al. 2009a). Data visualization and processing were completed using Geotool (Coyne and Henson 1995).

Figure 8. Moody array impulse response.



The specific analysis used is outlined as follows:

1. Filter raw infrasound data with 3-pole causal Butterworth band-pass filter between 0.5 and 10 Hz
2. Review data to visually identify coherent infrasound signal on a minimum of three channels per array
  - a. Impulsive sources
  - b. Continuous wave sources
3. If coherent infrasound signal is identified, then characterize signal
  - a. Determine frequency content of signal
    - (1) Create tight window over signal
    - (2) Create equal size window over background noise

- (3) Calculate FT of both windows. The difference between the two highlights the frequency content of the signal. The FT was calculated with a Hanning window.
- b. Calculate azimuth from array to source
  - (1) Create tight boxcar window over signal
  - (2) Calculate F-K with correct parameters for infrasound signal, such as frequency content and expected maximum velocity
  - (3) Note F-statistic of signal
  - (4) Note SNR of signal

The processing identified isolated, repetitive infrasound sources. When multiple arrays identified a source, azimuth lines of bearing from each of the arrays were used to estimate the source location by triangulation.

### **3.2.3 Source confirmation**

Once an infrasound signal was associated with a structural source, the association was investigated by source modeling and/or direct measurement. One of two methods was used to confirm whether the observed infrasound source correlated to the hypothesized structural source: (1) structural/acoustic finite-element model and (2) direct measurement of the source signal.

#### *3.2.3.1 Structural/acoustic Finite-Element Model*

A structural/acoustic Finite-Element Model (FEM) was created of the identified sources of interest and provided a computation of the fundamental modes of vibration based on the structure (McKenna et al. 2009c). The output of the FEM of a structural source can be coupled to the atmosphere to characterize the frequencies it radiates, which supports the confirmation of the infrasound signal to structural source measurement. A structural model of the hypothesized source was developed following the procedures presented in the introduction and outlined in McKenna et al. (2009b). This model was developed to quantify the frequencies that the structure naturally vibrates, and how these frequencies radiate into the atmosphere. The alignment of the predicted frequencies with the observations from the infrasound data was used to confirm the hypothesized structural source. If the frequencies did not align, the list of possible sources was reevaluated. The models were developed in COMSOL Multiphysics modeling software package.

### 3.2.3.2 *Direct source measurement*

When possible, hypothesized sources were confirmed by direct measurement of the natural vibrational frequency of the structure. These vibrational frequencies were compared with the measured infrasound signals; if they aligned, the hypothesized source was assumed reasonable. Measurement of the natural vibrational frequency of the bridge was completed by placing vertical seismometers on key structural components. The frequency content from the seismometer data was estimated in the same manner as described in the infrasound signal frequency content section.

## 3.3 **Wave propagation study**

Once the source-atmosphere interactions were quantified, models were developed to aid with the understanding of signal propagation over the distances consistent with the urban environment. The analysis included an assessment of how these waves are affected by the urban infrastructure (large buildings, roadways, densely space houses, etc.), and the unique weather environments that occur in the Urban Heat Island. A detailed urban terrain model was developed in a finite-difference time-domain (FDTD) code, PSTOP3D, to better understand the role that this urban terrain plays in affecting the propagation paths including the blocking of signals under some conditions (Ketcham et al. 2005; Wilson and Liu 2004; Pace et al. 2015).

Numerical modeling methods were used to extrapolate the knowledge learned about specific sources and propagation paths through the data collection. As noted earlier, a structural FEM was used to analyze the structure sources of interest in order to identify the fundamental modes of vibration of the structure (McKenna et al. 2009b). The results of this exercise guided the frequency content of source excitation that is coupled to the near field atmosphere model via COMSOL Multiphysics' structural mechanics and acoustic modules. The simulated near-field infrasound levels from the fundamental modes of the structure provided a basis for examining the robustness of the observations.

Once the source-atmosphere interactions were characterized, models were developed to understand signal propagation over distances consistent with the urban environment and included an assessment of how the acoustic energy was affected by urban infrastructure (large buildings, roadways, densely space houses, etc.). A detailed urban terrain model was developed

in PSTOP3D to quantify the role the urban terrain plays in infrasound propagation (Ketcham et al. 2005; Wilson and Liu 2004). This code bases the propagation of acoustic energy on a set of time variant partial differential equations (Ketcham et al. 2013).

$$\frac{\partial P}{\partial t} = -\rho c^2 \left( \frac{\partial v_1}{\partial x_1} + \frac{\partial v_2}{\partial x_2} + \frac{\partial v_3}{\partial x_3} - Q \right) \quad (2)$$

$$\frac{\partial v_1}{\partial t} = -\frac{1}{\rho} \left( \frac{\partial P}{\partial x_1} + \sigma v_1 \right)$$

$$\frac{\partial v_2}{\partial t} = -\frac{1}{\rho} \left( \frac{\partial P}{\partial x_2} + \sigma v_2 \right)$$

$$\frac{\partial v_3}{\partial t} = -\frac{1}{\rho} \left( \frac{\partial P}{\partial x_3} + \sigma v_3 \right)$$

where

$P(x_1, x_2, x_3, t)$  = pressure

$v(v_1, v_2, v_3, t)$  = particle velocity vector with components  $v_1$ ,  $v_2$ , and  $v_3$

$\rho(x_1, x_2, x_3)$  = spatial varying material density

$c(x_1, x_2, x_3)$  = spatial varying sound speed

$\sigma(x_1, x_2, x_3)$  = spatial varying flow resistivity

$Q$  = dilation-rate of source

This set of partial differential equations is solved with a staggered leapfrog approach with absorbing boundary conditions to reduce numerical noise in the solution (Ketcham et al. 2013; Wilson and Liu 2004).

The terrain model was constructed with refined 3-D buildings derived from 6-in. stereoscopic aerial imagery (with simplified roof shapes). Roads, bridges, paved areas (parking lots, medians, sidewalks), water features (rivers, streams, lakes), grassy/forested areas and the terrain skin are developed from 1m LIDAR (Light, Detection and Ranging) data, various planimetric data, and satellite imagery (Pace et al. 2015). This model was input into a layered atmosphere. An input source was added based on the analysis of observed data and the output of the structural-acoustic coupling model described earlier. Simulated receivers at different points in the model provided insight to complex propagation paths characteristic of urban environments.

## 4 Results

### 4.1 Summary of detections

Nineteen days of rooftop array data were analyzed from 01 August 2012 to 03 August 2013 details of each detection are documented in Appendix C. Specific dates reviewed and results from the data analysis are summarized in Table 1. The dates for analysis were selected from every season randomly with the limitation that a complete set of array data was available. Techniques used to analyze the data are outlined in the “Analyst review technique” section (3.2.2.1).

Key signal features include start time, end time, signal type, frequency content, apparent velocity, azimuth, Fisher Statistic, SNR, channels in the detection, any related signal, captures of the time series, F-K plot and FT plot. The main source observed was the Mockingbird Bridge with the most common frequency from 1.6 - 1.8 Hz and azimuths at Moody between  $147^{\circ}$ - $168^{\circ}$  and at multi-rooftop between  $130^{\circ}$ - $145^{\circ}$  (Table 1 and Figure 9). After removing these from the detection data, an additional five local detection maxima were observed with distinctive back azimuths to sources that have not been identified, (Table 2 and Figure 10).

Signals from the Mockingbird Bridge were detected on the rooftop arrays 17 of the 19 days analyzed. There appears to be little correlation between wind direction, wind speed and the number of detections (Figures 11 to 13). The wind speed and direction data in Table 3 are from the Dallas Love Field Airport approximately 6 km west of the arrays, which is reported by Weather Underground. The comparison of wind direction to the number of detections from Mockingbird Bridge does indicate a small increase of detections on days with southerly winds. The comparison of number of detections to wind speed does not have a trend. These trends would indicate there would be little to no effect of winds at local propagation distances in urban settings. These trends do not have any statistical confidence due to the limited sample size.

**Table 1. Summary of all detections recorded on rooftop arrays. Signal type: Continuous Wave (CW) and Impulsive (IMP).**

Date – Julian Day (UTC)	Number of Detections				Signal Type (CW or IMP) and Frequencies	
	Moody	Multi-Rooftop	Multi-Rooftop and Moody	Total	Moody	Multi-Rooftop
01 Aug 2012 – 214 Wednesday	22		4	26	CW: 1.6, 1.7, 1.8 IMP	CW: 1.6, 1.7, 1.8 IMP
15 Aug 2012 – 228 Wednesday	15	1	5	21	CW: 1.5, 1.6, 1.7, 1.8 IMP	IMP
01 Sep 2012 – 245 Saturday	11	1	5	17	CW: 1.6, 1.7, 1.8	CW: 1.6, 1.7, 1.8
09 Sep 2012 – 253 Sunday	19	14	25	58	CW: 1.6, 1.7, 1.8	CW: 1.6, 1.8, 2.7 IMP
31 Oct 2012 – 305 Wednesday	20	7	2	29	CW: 1.6, 1.7, 1.8, 3.1, 4.7, 5.1 IMP	CW: 1.6, 1.7, 1.8, 4.25- 4.54, 13.1 IMP
15 Nov 2012 – 320 Thursday	22			22	CW: 1.2, 1.5, 1.6, 1.7, 1.8 IMP	
1 Dec 2012 – 336 Sunday	11			11	CW: 1.6, 1.7, 1.8	
01 Jan 2013 – 001 Tuesday	18			18	CW: 1.6, 1.7, 1.8	
01 Feb 2013 – 032 Friday	16	7	8	31	CW: 1.6, 1.7, 1.8	CW: 1.6, 1.8 IMP
15 Feb 2013 – 046 Friday	17	3	8	28	CW: 1.5, 1.6, 1.7, 1.8	CW: 1.6, 1.8 IMP
01 Mar 2013 – 060 Friday	12	7	18	37	CW: 1.6, 1.7, 1.8 IMP	CW: 1.6, 1.7, 1.8 IMP
01 May 2013 – 121 Wednesday		19	2	21	CW: .4, 1.6, 1.7, 1.8 IMP	CW: .4, 1.6, 1.7, 1.8 IMP
15 May 2013 – 135 Wednesday		5		5		CW: 1.7, 1.8
03 Aug 2013 – 215 Saturday		28		28		CW: 1.7, 1.8, 2.5 IMP

Figure 9. Summary of all detections in Table 1 in comparison to back azimuth to source. The circumference axis is the back-azimuth to source in degrees and the radial axis is number of detections. The maximum number of detections is from the Mockingbird Bridge with the Moody array between azimuth 150° and 155° and the multi-rooftop array at 130°.

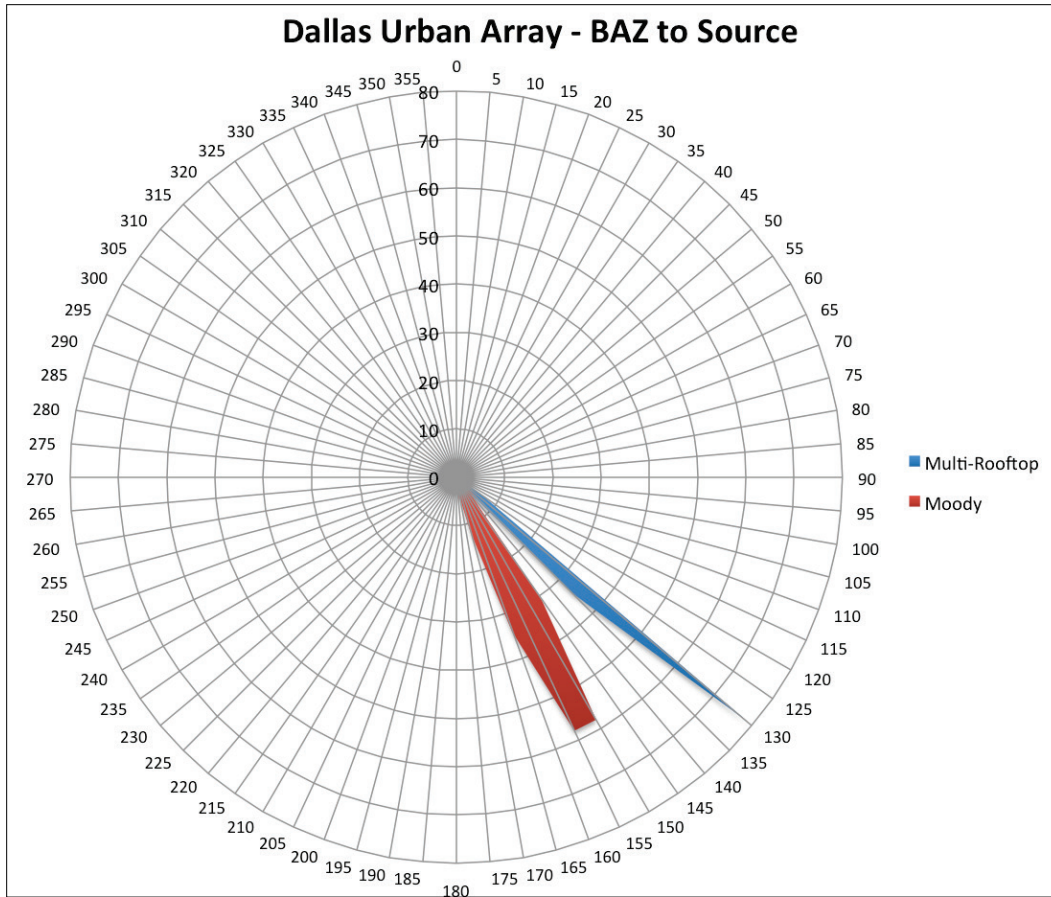


Figure 10. Summary of limited detections in Table 1 in comparison to back azimuth to source by removing the main azimuths associated with the Mockingbird Bridge for each array (Moody 150°-170° and multi-rooftop 130°-145°). This allows investigation of local detection maxima. The circumference axis is the back azimuth to source in degrees and the radial axis is number of detections. The maximum number of detections are from the Mockingbird Bridge with the Moody array between azimuth 135° and the multi-rooftop array at 125°. Other local maxima are Moody at 200°- 205°, Moody and multi-rooftop at 230°- 240°, Moody and multi-rooftop at 290° and Moody at 340°.

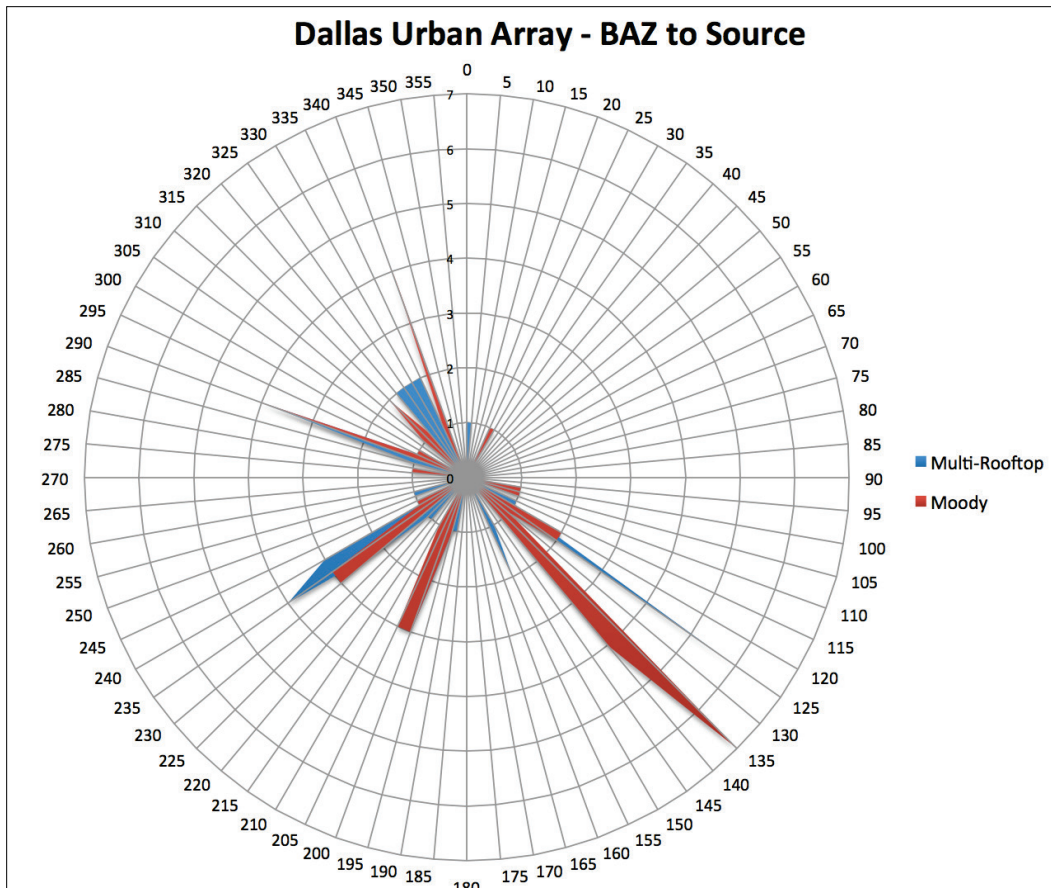


Table 2. Potential other source azimuths observed in data; repeated azimuths in detection data when binned to five-degree bins.

Array(s)	Azimuth(s) to Source
Moody	200°-205°
Moody and Multi-Rooftop	230°- 240°
Moody and Multi-Rooftop	290°
Moody	340°

Table 3. Selected days analyzed with number of detections marked for the Mockingbird Bridge combined with the wind speed and direction on the selected days (Wunderground.com 2012). The Mockingbird Bridge is located at an azimuth of 147°-168° from the Moody array and 130°-145° from the multi-rooftop array. The detections listed in this table are limited to detections from the each array for the appropriate azimuths. Detections for Mockingbird Bridge are marked approximately only one per hour even if more were available that were clearly similar to other Mockingbird Bridge detections in the hour, because the detections were too numerous to mark all. If more than 24 detections are marked in the hour then the signals looked unique or it was one of the first days investigated (253). \*Documented through initial processing methods, so individual statistics not available.

Date - Julian Day (UTC)	Number of Detections				Wind Direction	Wind Speed (mph)		
	Moody 147°- 168°	Multi-Rooftop 130°-145°	Combined	Total		Avg	Min	Max
01 Aug 2012 - 214 Wednesday	11		3	14	SSW	9	4	16
15 Aug 2012 - 228 Wednesday	11		1	12	SE	10	0	17
01 Sep 2012 - 254 Saturday	11	1	3	15	SSW	9	4	14
09 Sep 2012 - 253 Sunday	14	8	25	47	NE	3	0	9
10 Sep 2012 - 254 Monday*			18	18	SE	3	0	13
22 Sep 2012 - 266 Saturday*			25	25	SSW	3	0	8
11 Oct 2012 - 285 Thursday*			29	29	SE	5	0	10
31 Oct 2012 - 305 Wednesday	12	2	1	15	W	4	0	10
05 Nov 2012 - 310 Monday*				0	N	4	0	16
10 Nov 2012 - 315 Saturday*				0	S	15	12	18
15 Nov 2012 - 320 Thursday	14			14	ESE	6	0	16
1 Dec 2012 - 336 Sunday	11			11	S	14	9	20
01 Jan 2013 - 001 Tuesday	6			6	NNW	9	4	17
01 Feb 2013 - 032 Friday	13	4		17	E	9	3	15
15 Feb 2013 - 046 Friday	15	2	8	26	N	12	0	16
01 Mar 2013 - 060 Friday	10		9	19	NNW	7	0	15
01 May 2013 - 121 Wednesday		14	2	16	SE	10	4	14
15 May 2013 - 135 Wednesday		5		5	SSE	17	4	36
03 Aug 2013 - 215 Saturday		24		24	S	10	0	14

Figure 11. Comparison of wind direction effect on observations of Mockingbird Bridge signal. The data that populate the chart are from Table 3. The circumference axis is the wind direction in degrees, and the radial axis is number of detections. Southerly winds appear to provide a slight increased detection capability for the rooftop arrays.

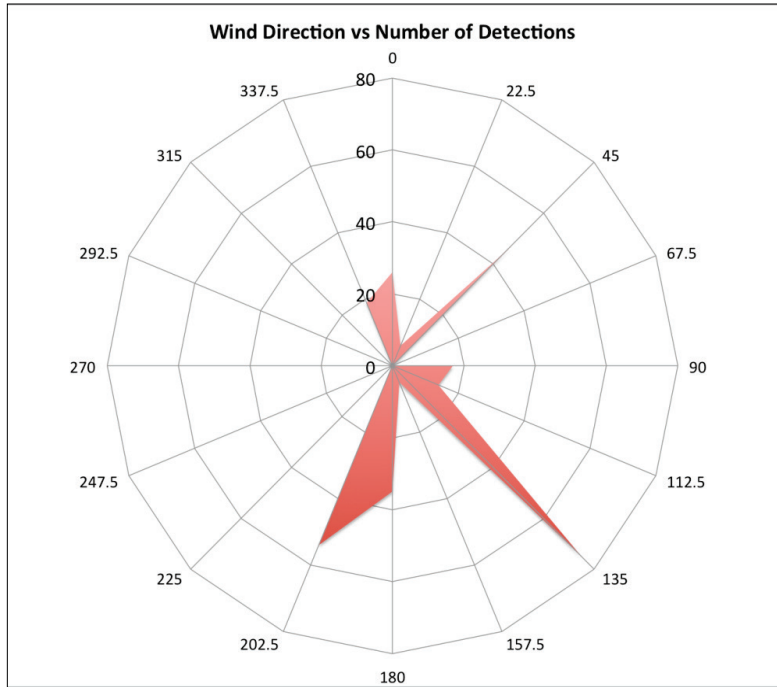


Figure 12. Comparison of number of detections from Mockingbird Bridge to wind speed, which shows limited effect. Table 3, provides data to populate this chart.

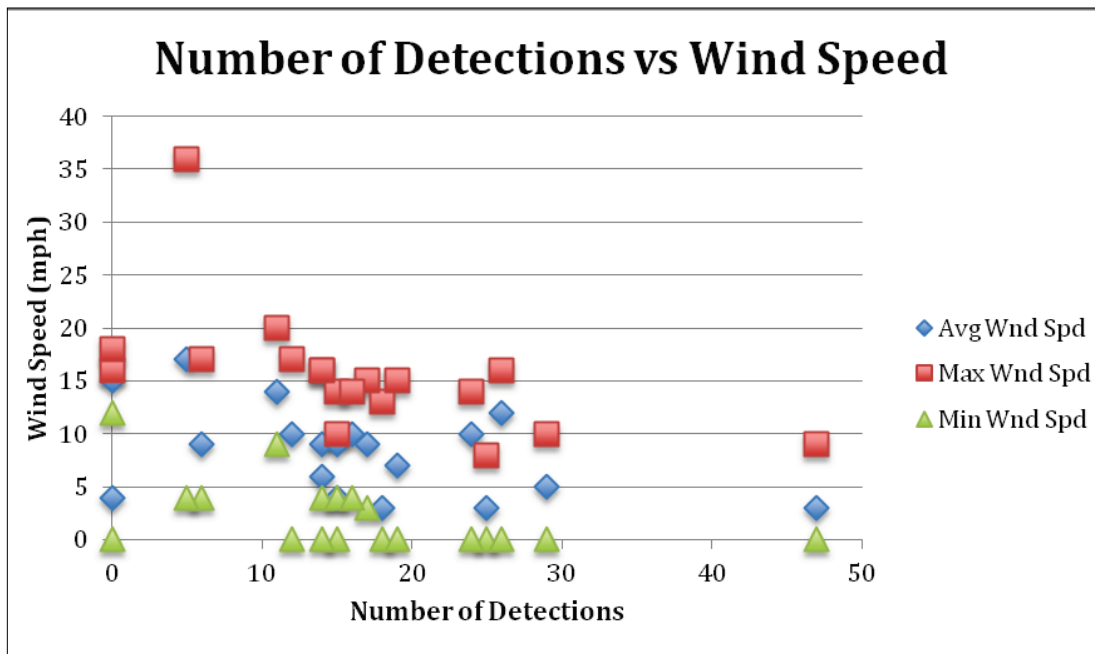
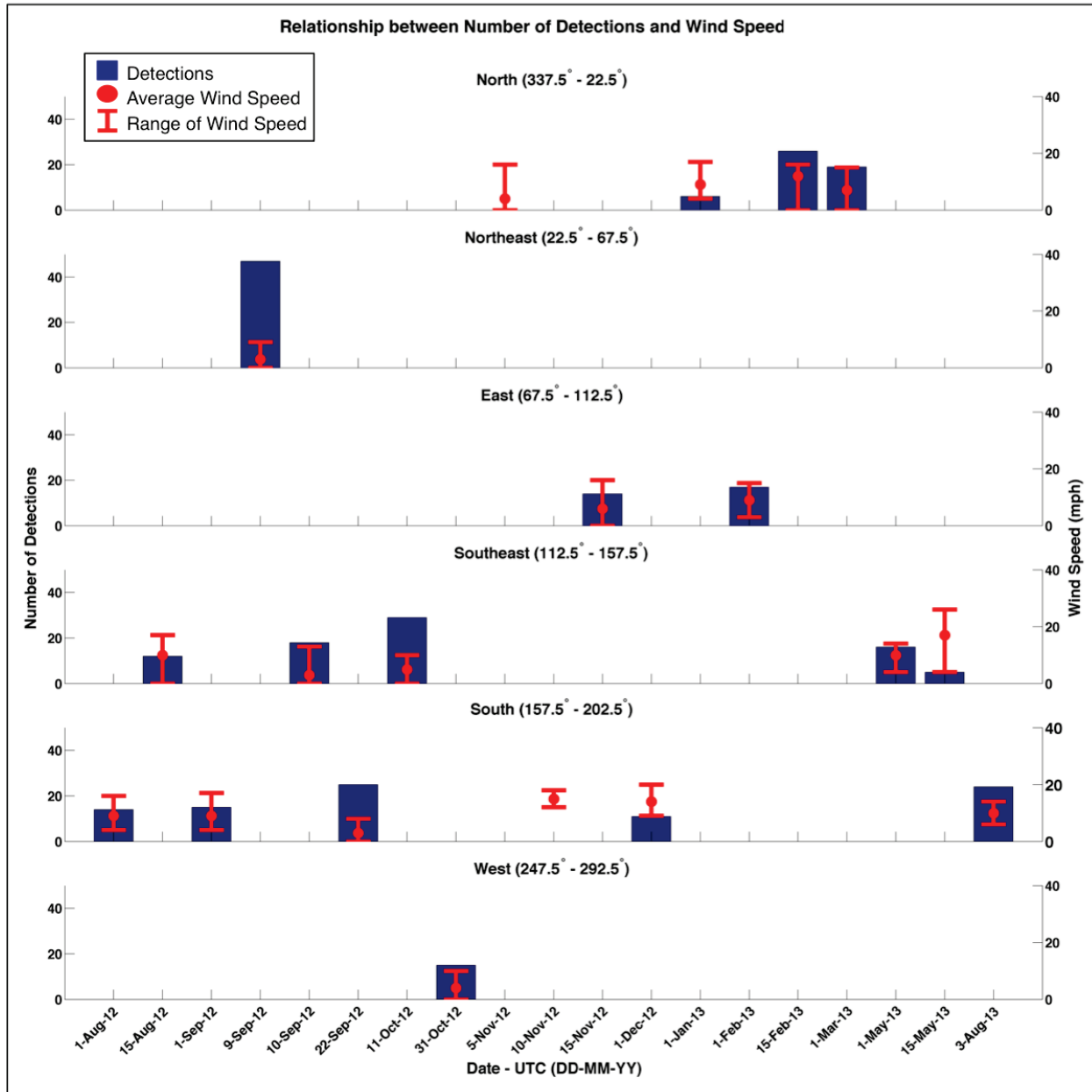


Figure 13. Comparison of number of detections, wind speeds and wind directions. The blue bars provide the given number of detections observed per day, the red dots are the averaged wind speed (mph) observed, and the red bars indicate the range of wind speed (mph) observed. Each plot is for specific wind direction, from top to bottom: North (337.5° - 22.5°), Northeast (22.5° - 67.5°), East (67.5° - 112.5°), Southeast (112.5° - 157.5°), South (157.5° - 202.5°), and West (247.5 - 292.5°).



## 4.2 Mockingbird Bridge case study

One set of source azimuths (147°-168° Moody array and 130° - 145° multi-rooftop array) are repeated over multiple days with source frequency contents between 1.5 – 1.7 Hz and 4.7 Hz. Figure 14 is an example time

series of the repeated source with the FT shown in Figure 15. Azimuth lines are drawn from the center of the multi-rooftop and Moody arrays. A hypothesized source that would fit these characteristics is the Mockingbird Bridge over U.S. Highway 75 at a distance of 0.71 km from multi-rooftop array and 0.45 km from Moody array (Figure 16). This source was confirmed through direct measurement and an acoustic model was designed to estimate the bridge's fundamental vibrational modes as discussed later.

The approach to understand and confirm the hypothesized source identified during the data analysis was to create a structural/acoustic model of the bridge as well as to measure the vibrational modes of the bridge. These vibrational modes are generally dependent on the geometry of the structure and the construction materials/methods.

**Figure 14. Examples of signal and background time series. The signal azimuth from array to source was between 132° and 137°. The light yellow window highlights the signal of interest and the dark grey window highlights background noise. Each different color trace indicates a different array element.**

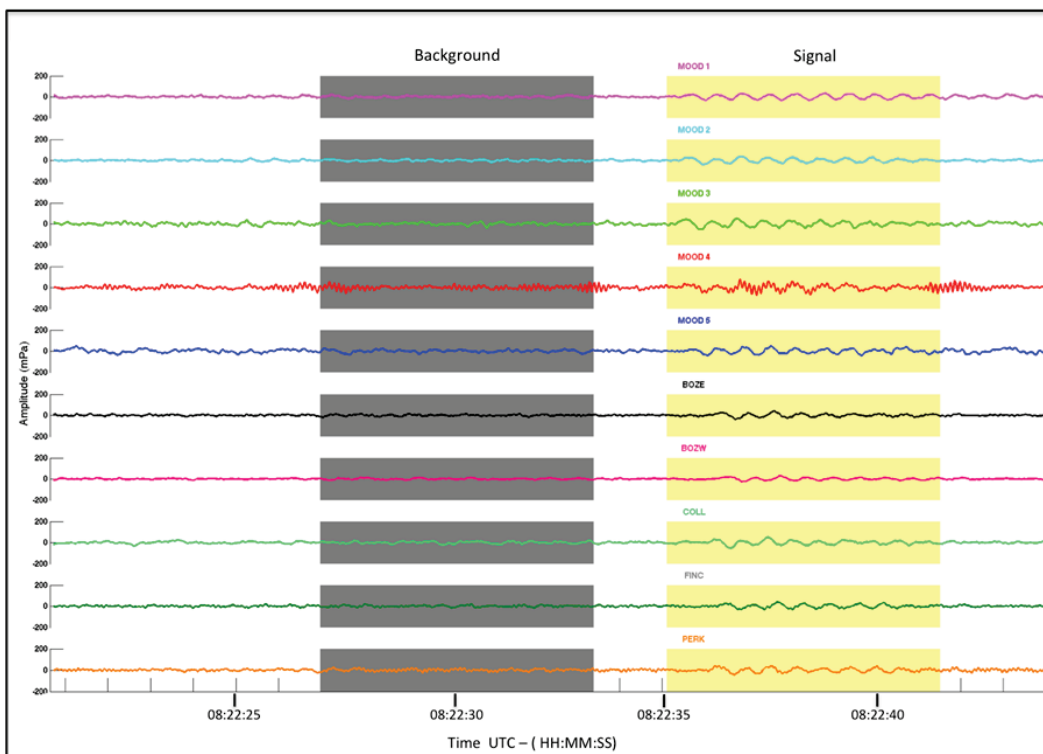


Figure 15. A comparison of the background noise (red) and signal (black) FT of the example time series in Figure 14. The grey box highlights a frequency peak at 1.6 Hz, that is seen in the signal FT and not background noise FT.

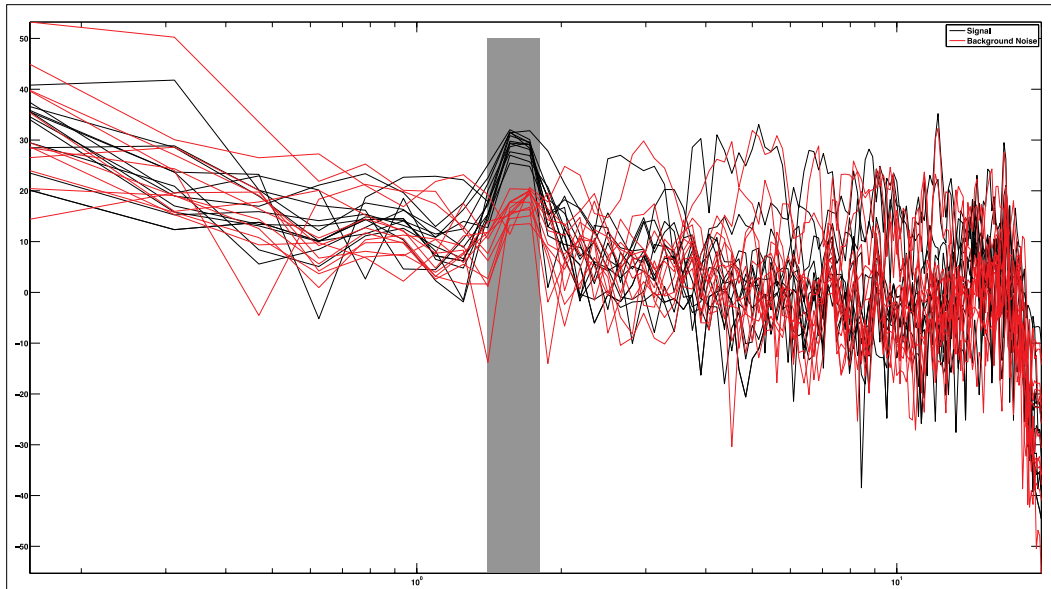
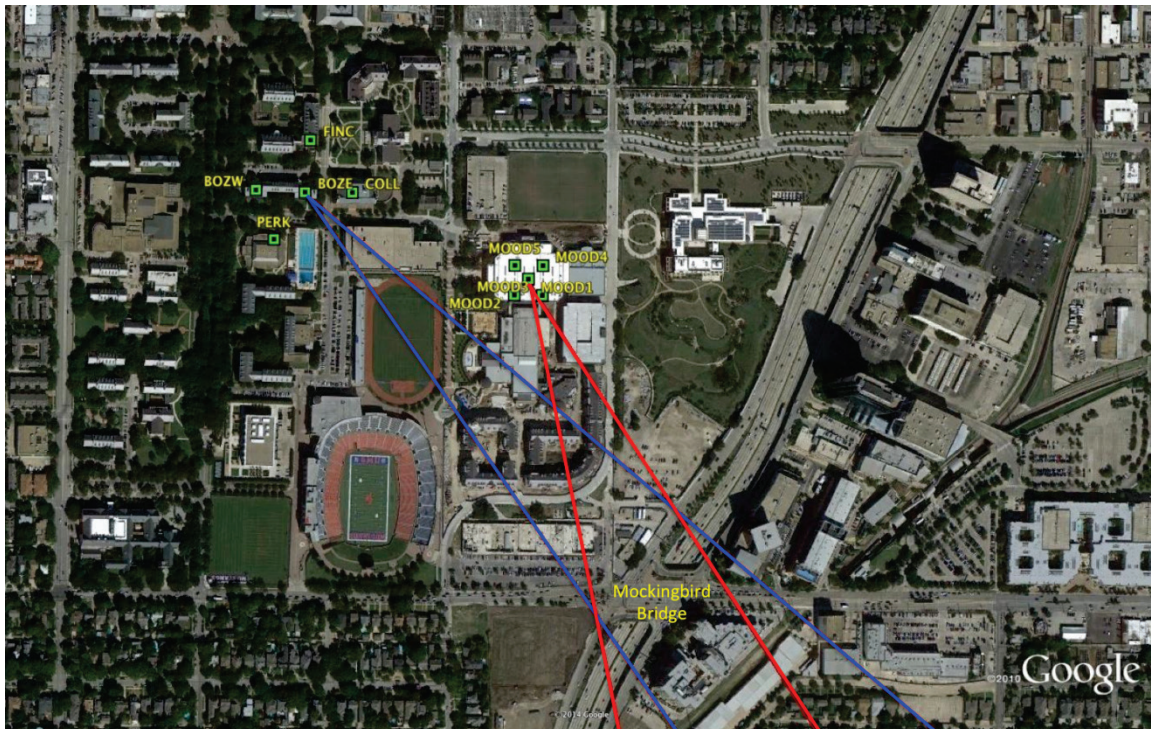


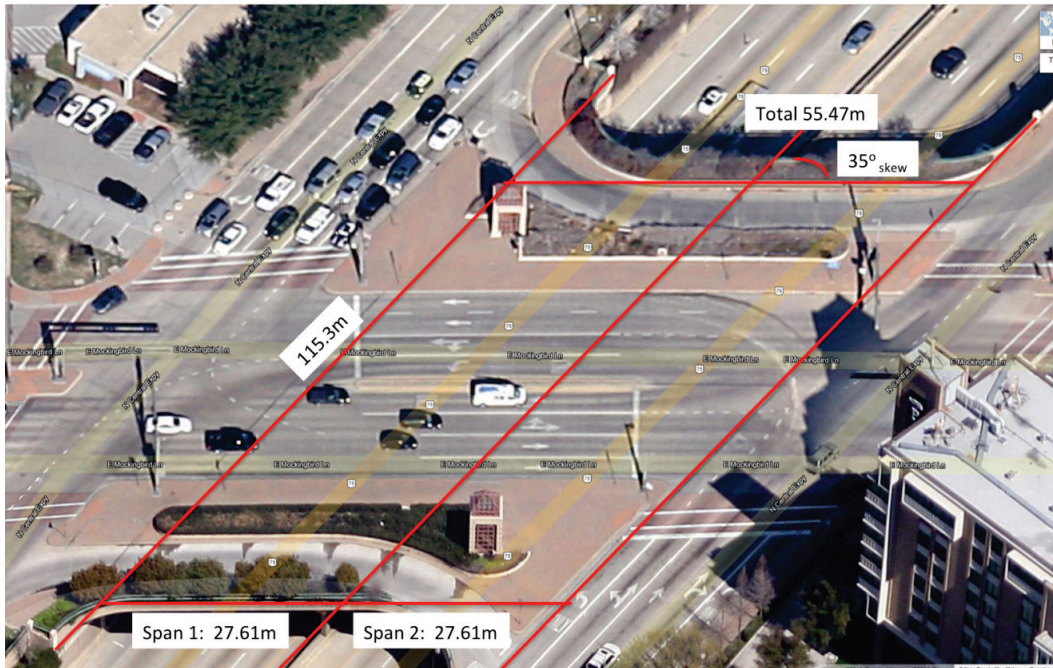
Figure 16. Overview map highlighting hypothesized source Mockingbird Bridge between crossing azimuths from the multi-rooftop array (blue lines) and Moody array (red lines). Green squares are infrasound sensor positions, blue lines are azimuth lines 130° and 145°, and red lines are azimuth lines 147° and 168°.



#### 4.2.1 Mockingbird Bridge – acoustic model

The bridge has two structural spans but is wider (115.3 m) than it is long (55.22 m) with a skew of  $35^\circ$  (Figure 17). The as-built drawings for this bridge were received from the Texas Department of Transportation (TX-Dot 1993).

Figure 17. Aerial imagery of the Mockingbird Bridge from Google Earth. The red lines highlight the main structural supports of the bridge.



The construction method used for the Mockingbird Bridge allowed for engineering judgment to simplify the modeling scheme for this bridge. The deck of the bridge is constructed using the adjacent box beam method, which means the deck will act as a monolithic structure (Figure 18). This engineering knowledge does not require development of a full structural model to understand how the structure will radiate energy. Given the dimensions and stiffness of the bridge, the structure is model as a confined air model with boundary conditions of four hard walls and two soft walls that represented the open curved ends Figure 19.

Figure 18. A cross-section view of the Mockingbird Bridge deck. The orange sections highlight the structural features that allow the bridge deck to act as a monolithic structure (TX DOT 1993).

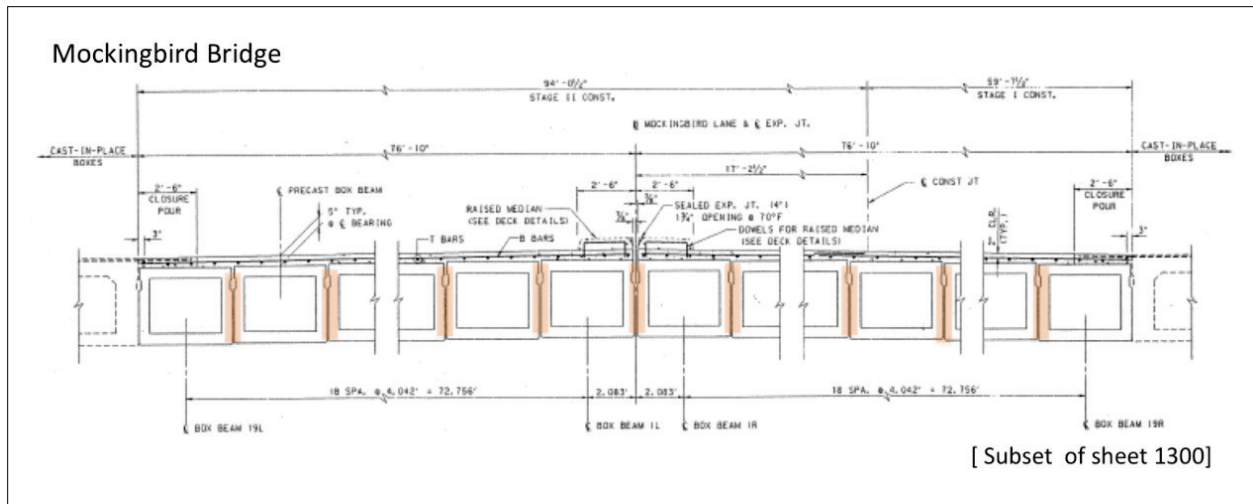
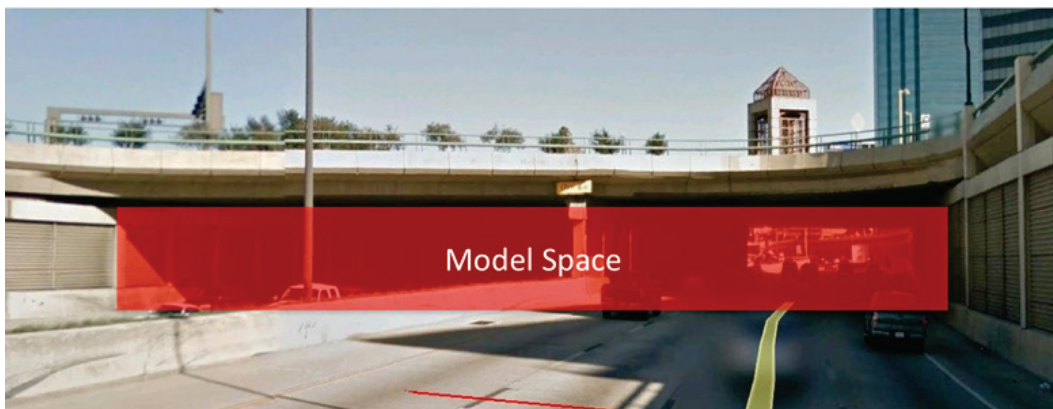


Figure 19. A Google street view of the Mockingbird Bridge driving north on I-75. The red highlights the confined air, which is the model space.



Given the confined air space of this bridge, a pressure acoustic model was developed in COMSOL– Multiphysics 4.3a Acoustic Package using the bridge dimensions, and structural geometry. The pressure acoustics module has interfaces where the sound field is described and solved by the pressure  $p$ . The pressure represents the acoustic variations (or excess pressure) to the ambient stationary pressure. The ambient pressure is, in the absence of flow, simply the static absolute pressure. A pressure acoustic model is a simplified model of the structure that is based on the bridge dimensions and the fundamental modes are determined by the cavity resonances; this method works on a limited basis that is defined by the bridge characteristics, such as the adjacent box beam design of the Mockingbird Lane Bridge. The Mockingbird Bridge model had 4 main modes of vibration,

2.0 Hz, 3.9 Hz, 4.3 Hz, and 5.2 Hz (Table 4). The acoustic model is shown in Figure 20. The shapes of each of the modes are shown with the warmer the color the greater the acoustic pressure on the surface of the model. The fundamental mode that is consistent with the signals observed on the urban array deployment consists of motion that is slightly offset from the northwest/southeast orientation of the traffic lanes. Since the first mode has the most energy associated with it, the model is consistent with the lower frequency observation. Two other modes were observed from the azimuth of this bridge; (1) Julian day 285 UTC observed signals at frequency 3.86 Hz correlates to second mode 3.87 Hz, and (2) Julian day 305 UTC observed signals at frequencies 4.25 – 4.54 Hz correlates to third mode 4.34 Hz.

A parametric temperature study of the model was completed that varied the model temperature based on average monthly temperatures in Dallas, TX. The model input temperature was varied to determine the effect on the vibrational modes of the structure. The default model temperature for basic model runs was 68°F. The ranges of temperatures evaluated for this study are provided in Table 5. The lowest temperature evaluated was 36°F, which produced modes of 1.94 Hz, 3.74 Hz, 4.20 Hz, and 4.99 Hz. The highest temperature evaluated was 96°F, which produced modes of 2.02 Hz, 3.89 Hz, 4.37 Hz, and 5.19 Hz. The warmer model temperature produces higher vibrational frequency of the structure. The difference between the low and high temperature vibrational frequencies were 0.12 Hz, 0.23 Hz, 0.26 Hz, and 0.29 Hz, respectively. The spacing between the modes stayed approximately equal for each of the trials, with a space of 1.8 Hz between modes 1 and 2, 0.5 Hz between modes 2 and 3, and 0.8 Hz between modes 3 and 4. Figure 21 highlights that temperature varied widely over an average year, but the frequencies remain fairly constant.

**Table 4. The four main vibrational modes identified from the acoustic model of the Mockingbird Bridge.**

Mode	Frequency (Hz)
1	2.0
2	3.9
3	4.3
4	5.2

Figure 20. Pressure acoustic model. The warmer the color the greater the pressure on the surface.

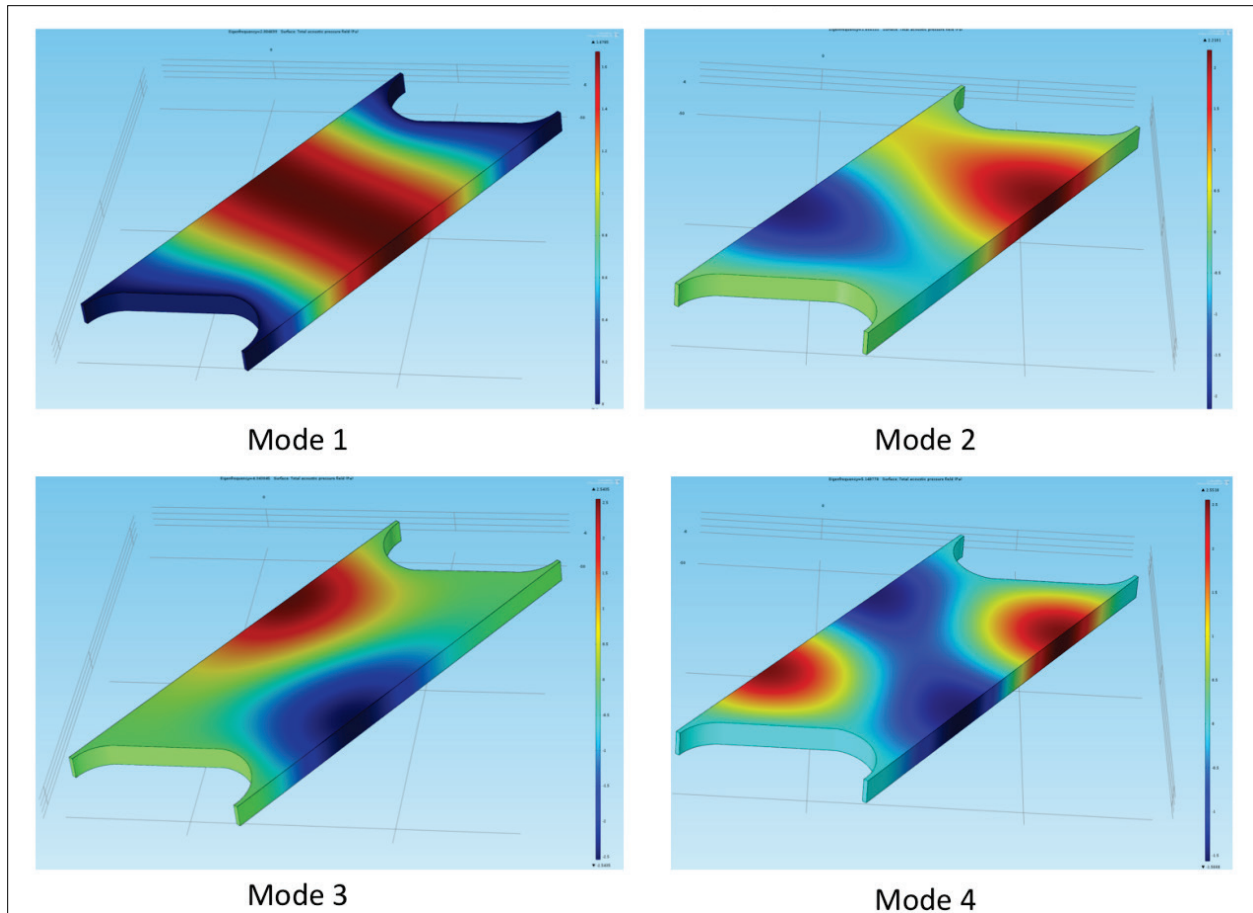
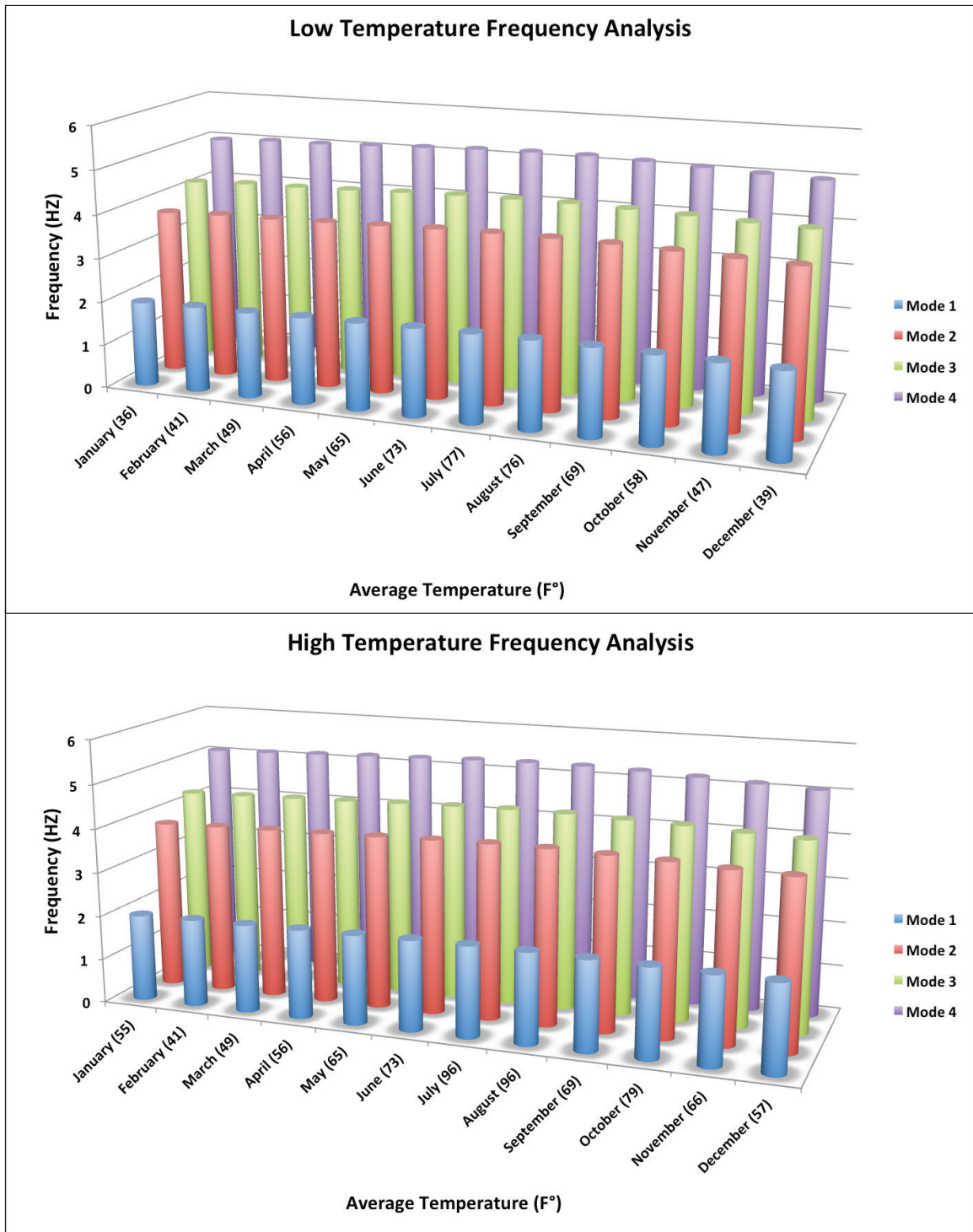


Table 5. Average high and low temperatures for each month in Dallas, Texas (Intellicast.com 2014).

Month	Average Low (F)	Average High (F)
January	36°	55°
February	41°	61°
March	49°	69°
April	56°	77°
May	65°	84°
June	73°	92°
July	77°	96°
August	76°	96°
September	69°	89°
October	58°	47°
November	47°	66°
December	39°	57°

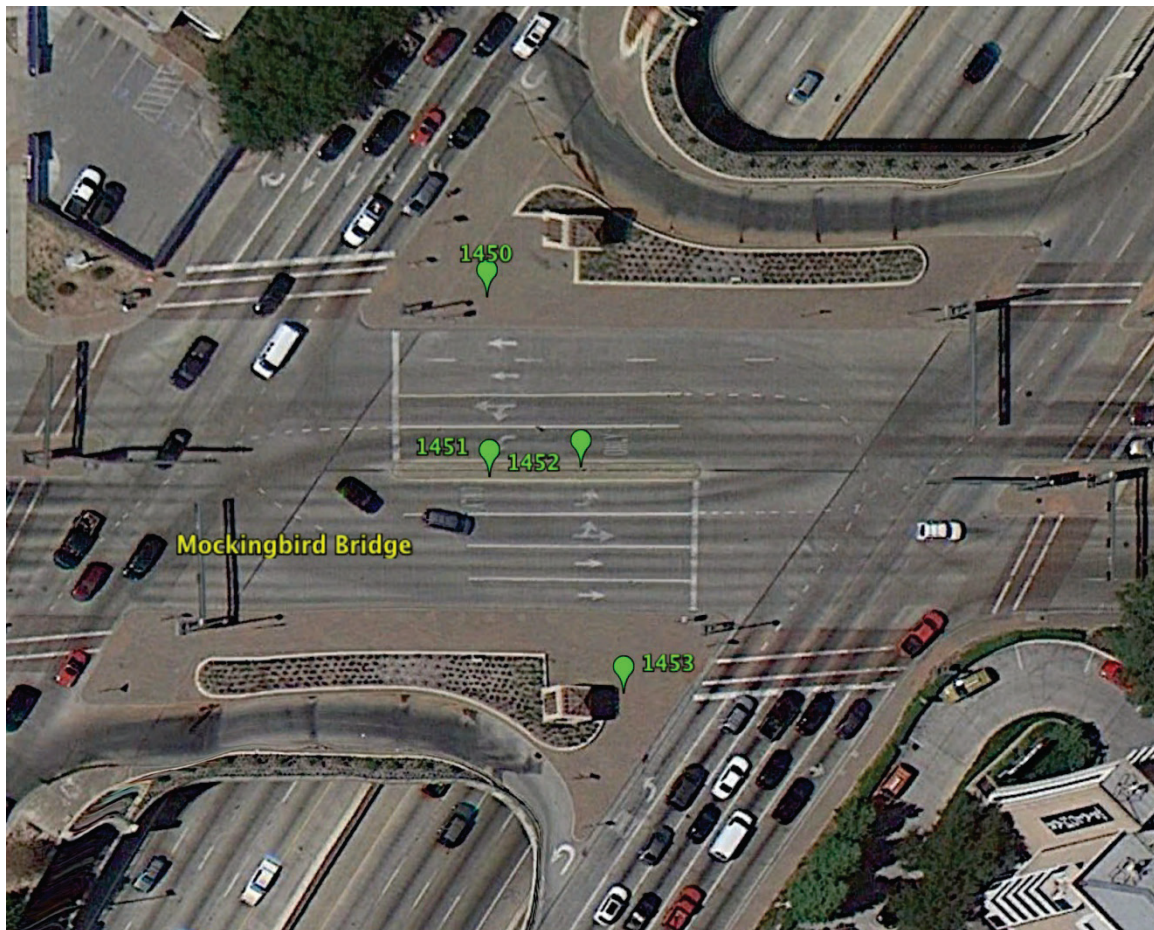
Figure 21. The first four vibrational modes at each monthly average low (upper) and high (lower) temperature.



#### 4.2.2 Mockingbird Bridge – direct source measurement

The infrasound observations and the subsequent models motivated the direct source measurements on the bridge in order to improve the understanding of vibration frequencies of the bridge. Mark L-4 vertical seismometers were deployed on the bridge on 13 March 2013 from 1000 – 1100 UTC. Each sensor was digitized with single channel Reftek 125A 24-bit recorder operating at a gain of 4x and a sample rate of 200 samples per second. Figure 22 is an overview map of the seismometers deployed on the bridge. The sensor locations were selected based on the locations of the main structural members of the bridge, with sensors 1451 and 1452 on the east and west of the center support of the bridge and sensors 1450 and 1453 on the outside edges of the bridge.

Figure 22. Overview map of the direct source measurement sensor deployment. Each green marker is a location of a vertical seismometer.



The collected direct source data were processed using Geotool. FTs were calculated over approximately 10-sec intervals. The FT was estimated using only one window, since the data were not smoothed. There were two types of data to review in this time period. One set was acquired with little or no traffic to estimate background noise levels, and the second set was acquired during time periods when traffic was present on the bridge (impulsive signals in time series).

Background noise was defined by time series that did not have any large impulses. The frequency content of the background noise had two main peaks in the FT plot at 1.5 - 1.7 Hz and 3.9 - 5.5 Hz. These frequency peaks aligned with the vibrational modes identified in the acoustical model and in the observed urban infrasound array data. Examples of the background noise time series and spectra are shown in Figure 23. Similar analyses were undertaken on a subset of the large impulses and is displayed in Figure 24. Spectral comparisons between the noise and traffic signals illustrate that frequencies above 10 Hz are affected by the traffic signal. Figure 24 highlights this effect with the addition of peaks in the spectra at 13.5 - 21.6 Hz and 29 - 33 Hz. The energy from the traffic was not observed on the urban array, but this is expected, given the high frequency content of the signal and the low source energy. In both the background noise and traffic signal examples, the four modes identified in the acoustic model are clearly observed in the direct source measurement.

Figure 23. Example of background noise. Left: Time series from the four deployed vertical seismometers. Right: FT calculated of the 10.23-sec window in time series to the left, which highlights the background noise levels in the data. Two main frequency peaks are seen in the data (A and B). Peak A is frequencies 1.5 - 1.7 Hz and peak B is frequencies 3.9 - 5.5-Hz.

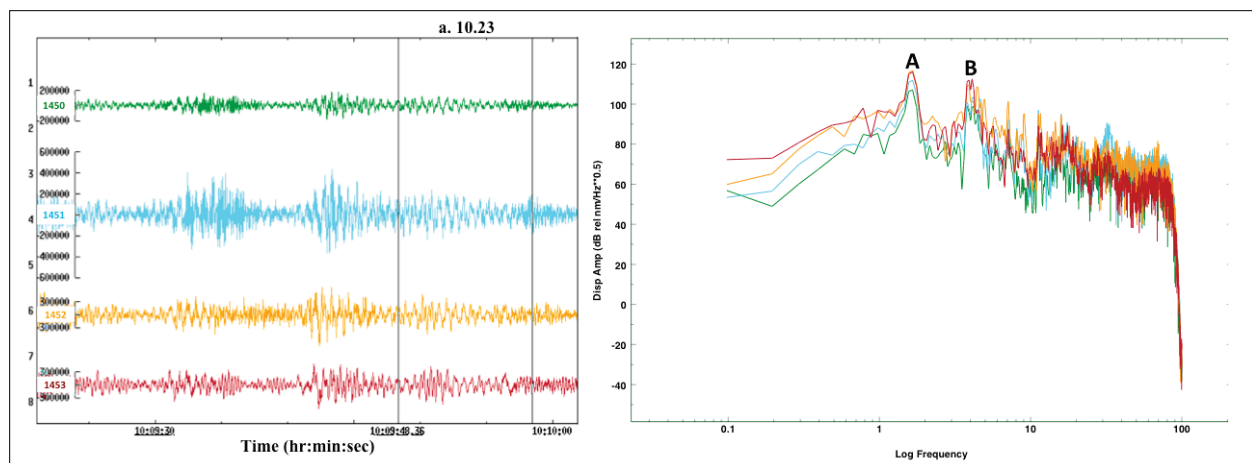
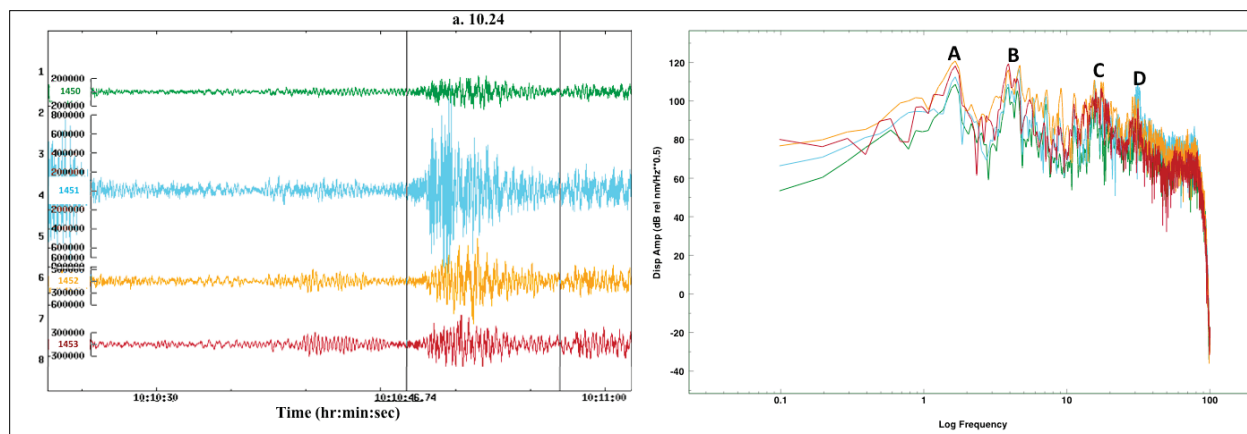


Figure 24. Example of traffic signal. Left: Time series from the four deployed vertical seismometers. Right: FT calculated of the 10.24-sec window in time series to the left, which highlights the background noise levels versus the traffic signal. Four frequency peaks are seen in the data (A, B, C, D). Peak A frequencies 1.5 - 1.7 Hz, peak B frequencies 3.9 - 5.5 Hz, peak C frequencies 13.5 - 21.6 Hz, and peak D frequencies 29 - 33 Hz.



### 4.3 Lovers Lane case study

Lovers Lane Bridge over Interstate 75 was the next largest bridge of similar construction method and distance as the bridge first observed with the rooftop arrays. The initial pass through the observational data did not identify the Lovers Lane Bridge with the rooftop arrays. This initial result was investigated by developing an acoustic model of the Lovers Lane Bridge to determine the fundamental modes of the structure, since these are the most likely frequencies observable by infrasound sensors (Donn 1974; McKenna et al. 2009a).

#### 4.3.1 Lovers Lane technical specifications

Lovers Lane Bridge is 1.57 km at an azimuth of  $47^\circ$  north of the Boaz East infrasound station (Figure 25). The as-built drawings for this bridge were obtained from TX-DOT (TX DOT 1993). This bridge had construction methods similar to the Mockingbird Bridge (i.e., a two span bridge with a total width of 89.28 m and total length of 48.57 m). Direct comparison of the area of the two bridges illustrates that the Mockingbird Bridge is 24 percent larger than Lovers Lane Bridge (Figure 26). This is expected to lead to higher fundamental resonant frequencies for Lovers Lane because the mass of the structure is a direct term in the natural frequency of vibration equation (Chopra 2001). The natural frequency of vibration equation states:

$$f_n = \frac{1}{2\pi} \sqrt{\frac{k}{m}} \quad (3)$$

where:

$f_n$  = resonant frequency (Hz)

$k$  = stiffness

$m$  = mass

Since the Mockingbird Bridge and Lovers Lane Bridge differ in total area but have similar construction practices and materials, it would be expected that the mass of Mockingbird is greater than that of Lovers Lane; therefore, Mockingbird would have lower fundamental frequencies than Lovers Lane.

Figure 25. Map that highlights the relationship of Lovers Lane Bridge to the rooftop arrays, which is located 1.57 km at an azimuth of 47° from North. Green squares highlight infrasound sensor position and the red line is the 47° line of azimuth.

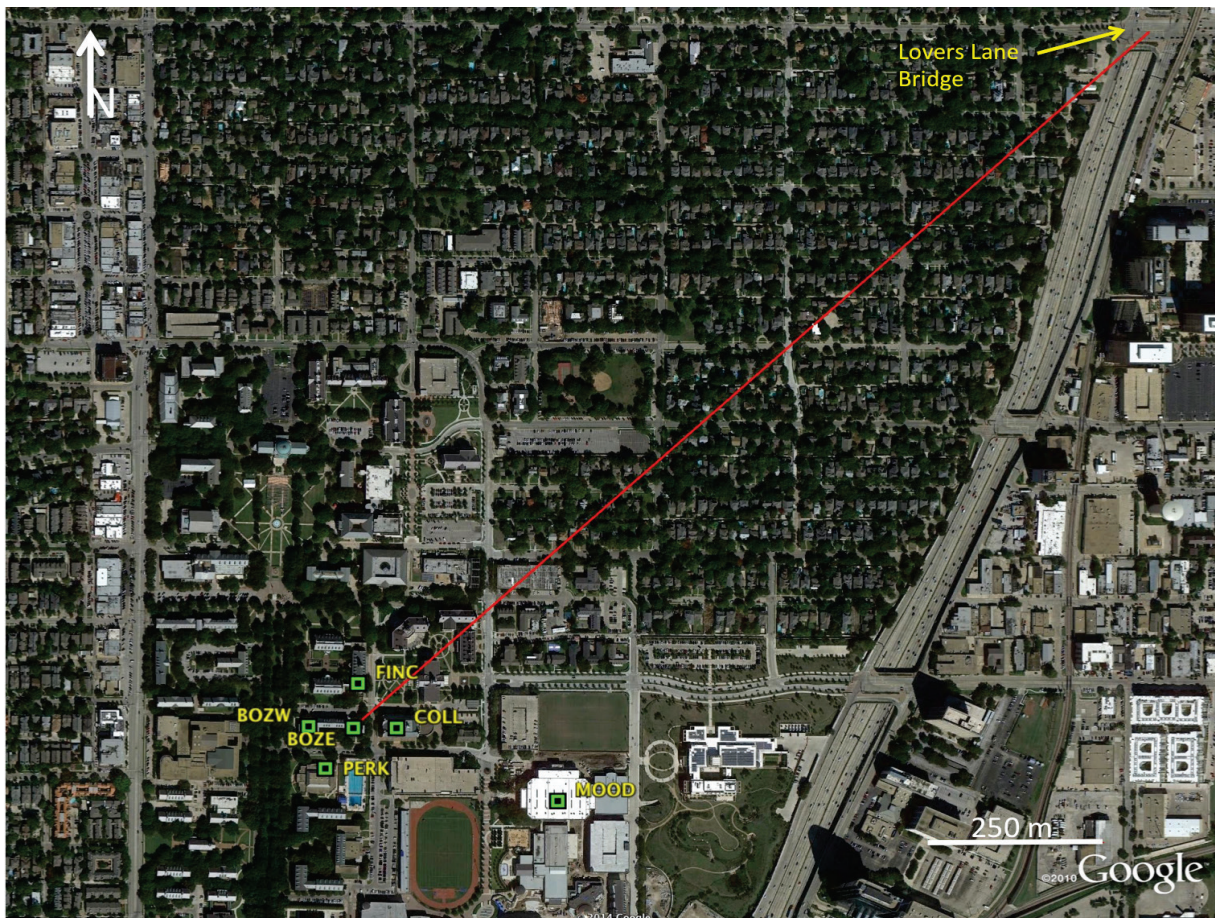
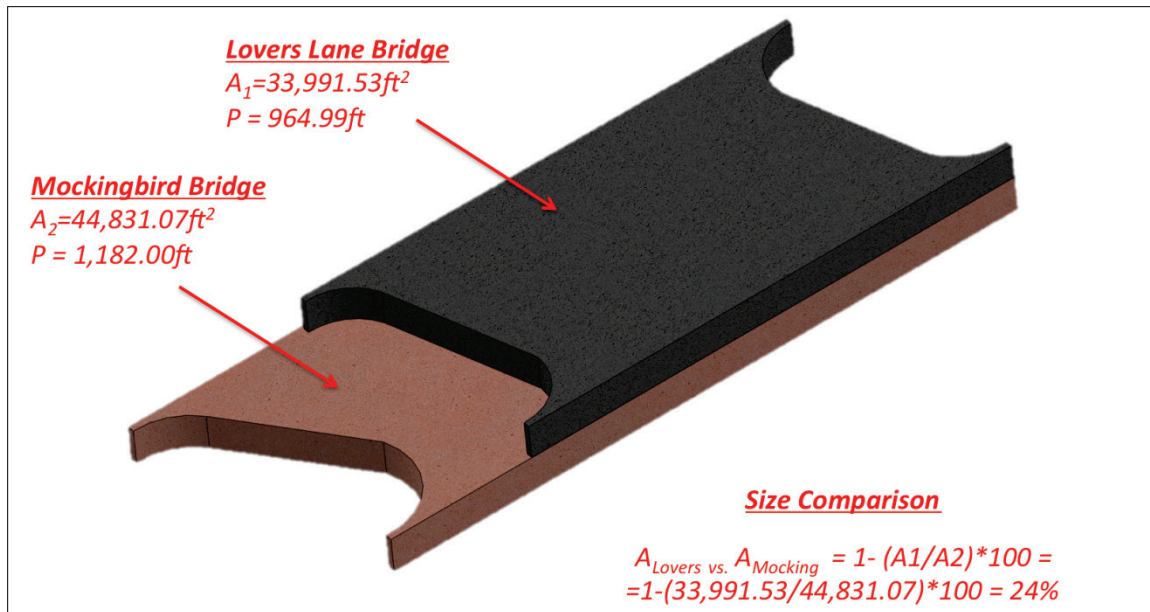


Figure 26. Size comparison between Lovers Lane Bridge and Mockingbird Bridge. The area of the Mockingbird Bridge is 24% greater than the area of the Lovers Lane Bridge.



#### 4.3.2 Lovers Lane – acoustic model

Based on the technical specification for the Lovers Lane Bridge, an acoustic model was developed in COMSOL – Multiphysics 4.3A Acoustics Package. The confined air model boundary conditions were based on a tunnel with four hard walls and two soft walls, which were the open ends of the bridge (curved ends). The mathematical representations of the used boundary conditions are

- Sound hard boundary–Neumann condition; normal component of the acceleration is zero:
  - $dp/dn=0$  (normal velocity=0)
- Sound soft boundary – Dirichlet condition;  $p = 0$  (pressure release)

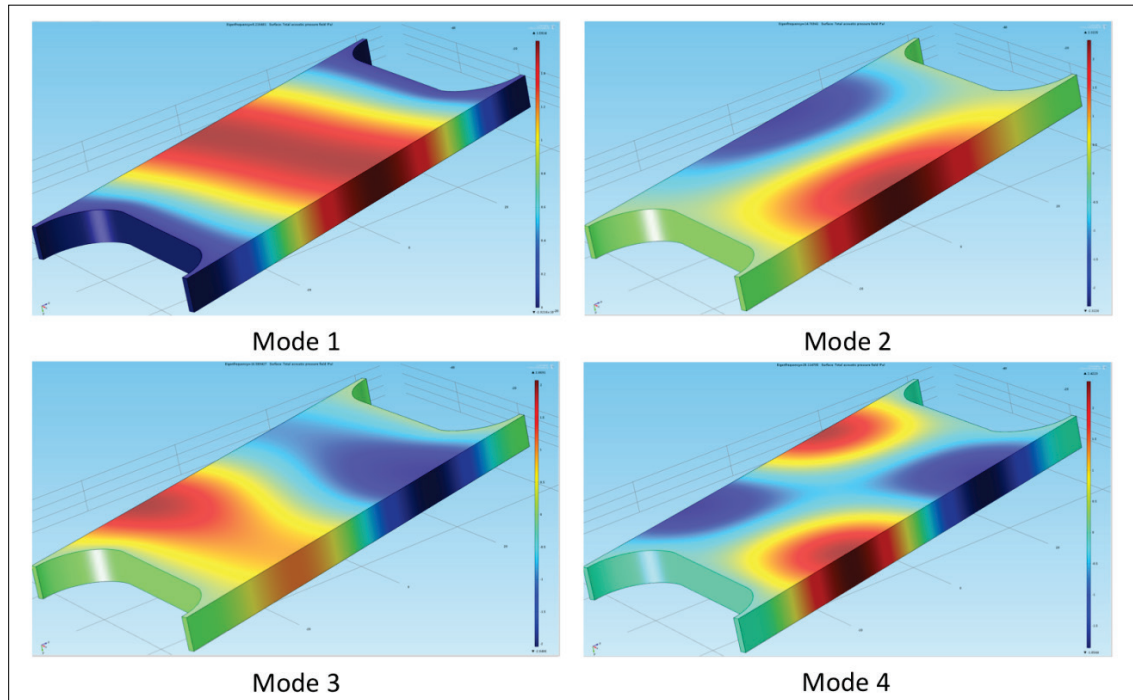
This was the same approach that was used to develop the Mockingbird Bridge model, which had similar shape and construction method as the Lovers Lane. The model had four main modes of vibration, 8.21 Hz, 14.76 Hz, 16.58 Hz, and 20.11 Hz (Table 6). The acoustic model is shown in Figure 27. The shapes of each of the modes are shown with the warmer the color the greater the acoustic pressure on the surface of the model. As expected, Lovers Lane has higher main vibrational modes than Mockingbird. The smaller is the more rigid structure, resulting in high

vibration frequencies representing low periods of vibrations (T). Further explanation is provided in “4.3.1 Lovers Lane technical specifications” section.

**Table 6. The four main vibrational modes identified from the acoustic model of the Lovers Lane Bridge.**

Mode	Frequency (Hz)
1	8.21
2	14.76
3	16.58
4	20.11

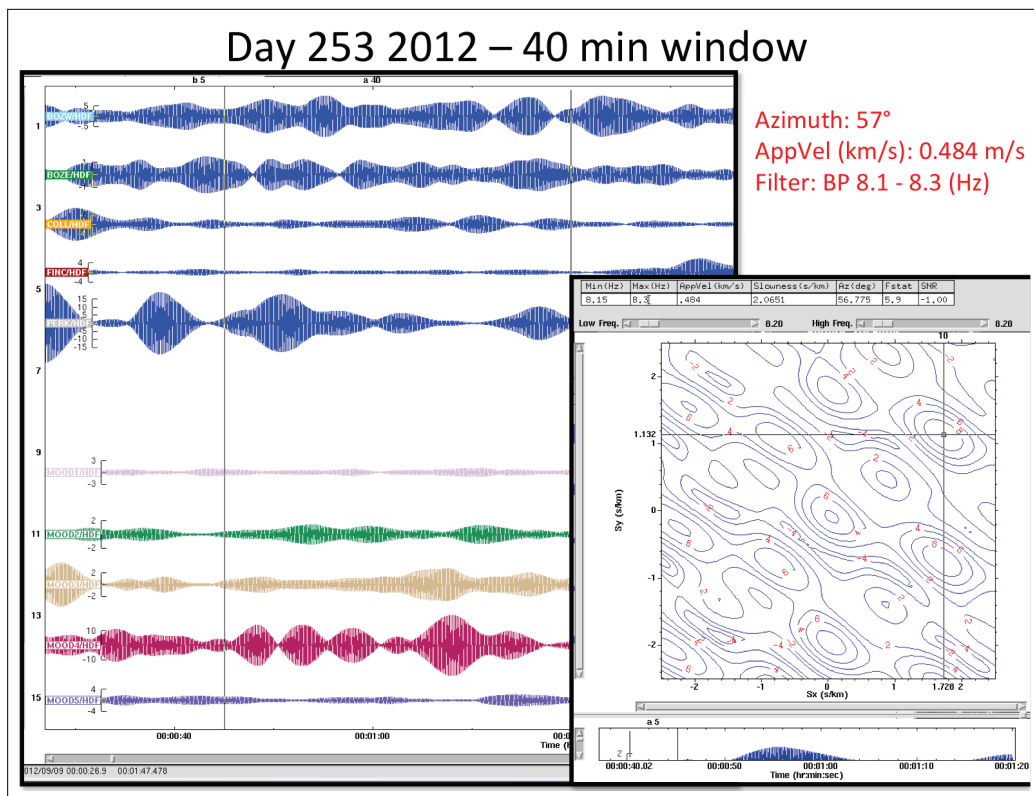
**Figure 27. Pressure acoustic model of Lovers Lane Bridge. The warmer the color, the greater pressure on the surface.**



Given the higher frequencies of the main vibration modes of the Lovers Lane Bridge, there is expected to be a greater effect of the urban landscape in the transmission of these wavelengths. The expected wavelength for Mode 1 at 8.21 Hz is 40.2 m, which will be more affected by scattering caused by larger buildings and other larger features in the urban landscape. These higher frequencies have greater loss of energy due to attenuation as compared to lower frequencies of the Mockingbird Bridge.

Subsequent to this analysis, Lovers Lane Bridge signals were identifiable on the rooftop arrays but only through targeted narrow band filtering at the identified first mode of the bridge. The data were filtered with a band-pass filter between 8.1 Hz and 8.3 Hz, and then a large window (40 min) was applied before the F-K analysis was completed (Figure 28). The F-K analysis indicated the source was at an azimuth of  $57^\circ$  with an apparent velocity of 0.484 km/s. A review of the F-K analysis plot indicates limited confidence in the results due to the number of local maxima on the plot. This is due to the design of the array layouts, which were discussed in the “Array response” section.

Figure 28. Narrow bandpass (BP) filter example for rooftop array data, which demonstrates the targeted data processing use to identify the Lovers Lane Bridge. Data processing specifications – bandpass filter: 8.1 - 8.3 Hz, window size: 40 min; Results – F-K analysis, azimuth:  $57^\circ$ , apparent velocity: .484 km/s.



#### 4.4 Wave propagation study

A wave propagation study in an urban environment is used to explore the effects of urban infrastructure on the acoustic signals. An urban terrain was developed based on spectroscopic aerial imagery of the area

surrounding the SMU campus (Figure 29). This model includes 3-D buildings with simplified roof structures, bridges, grassy areas, paved areas, and general topography to provide a realistic recreation of the urban propagation environment (Figure 30). The model space is 2.5 km by 2.5 km centered on the multi-rooftop array.

Figure 29. Overview map of model area. Green, purple and yellow circles mark array locations, pink rectangle marks source location, and orange color marks building locations.

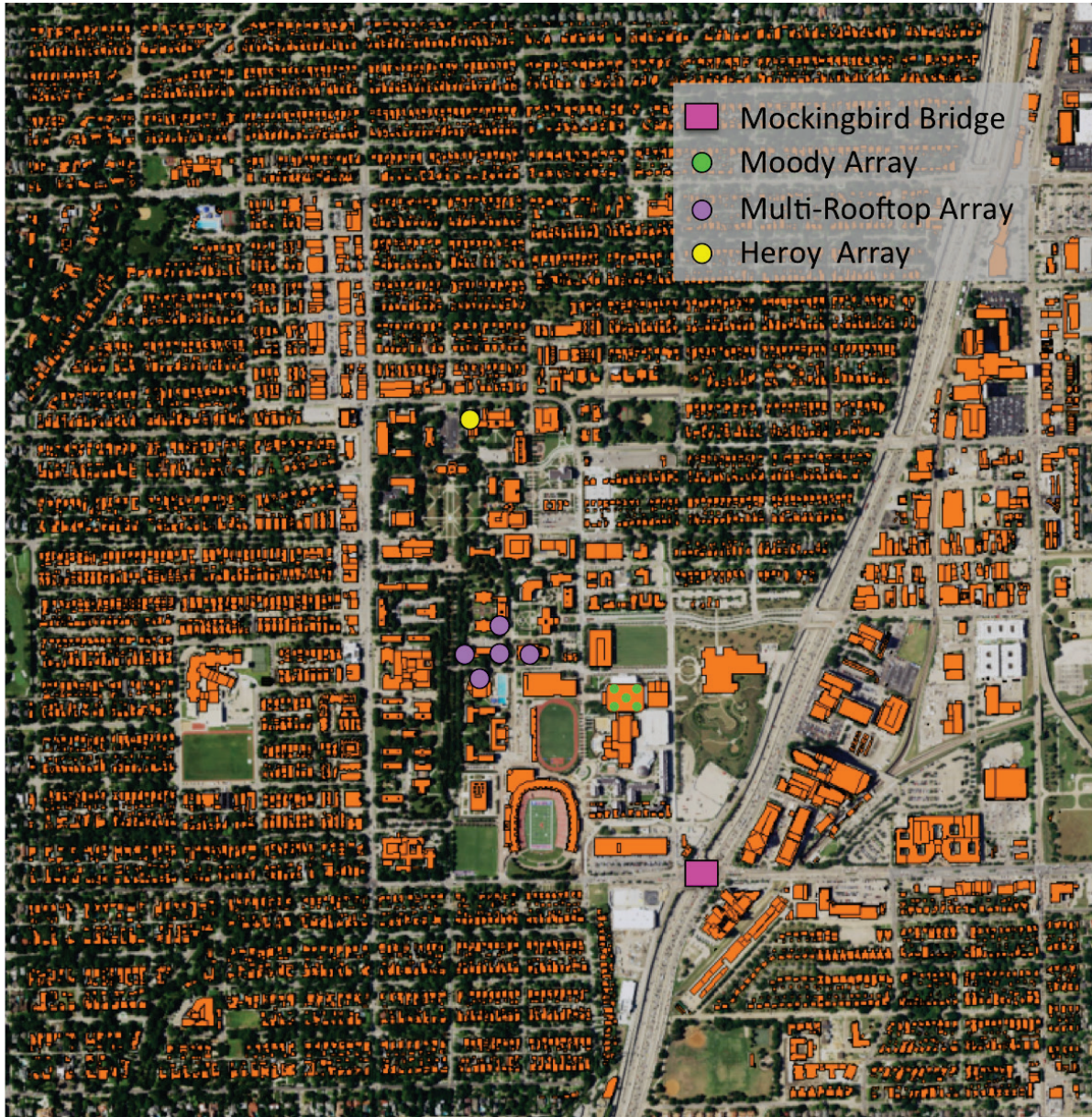
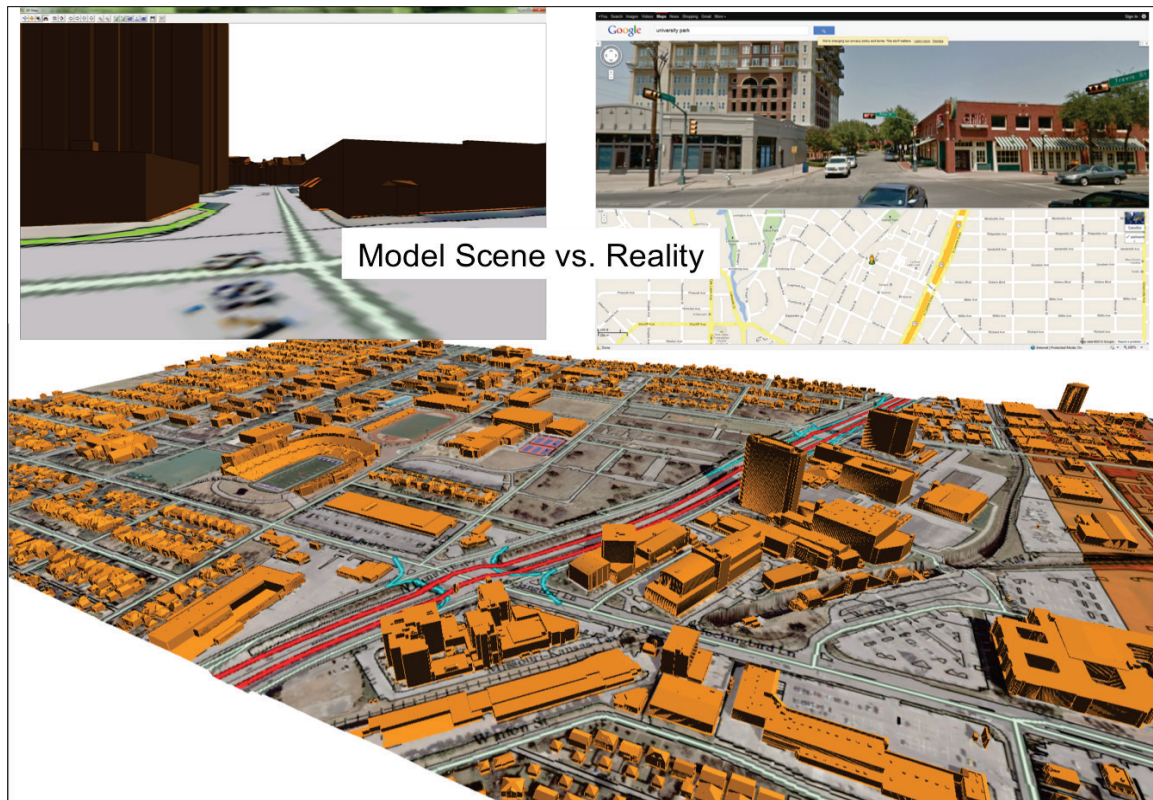


Figure 30. Upper-half of figure compares model output to Google Maps Street View. Comparison of roof heights and shapes are similar. Lower half of figure is a representative photograph of the 3-D terrain developed over the model space.



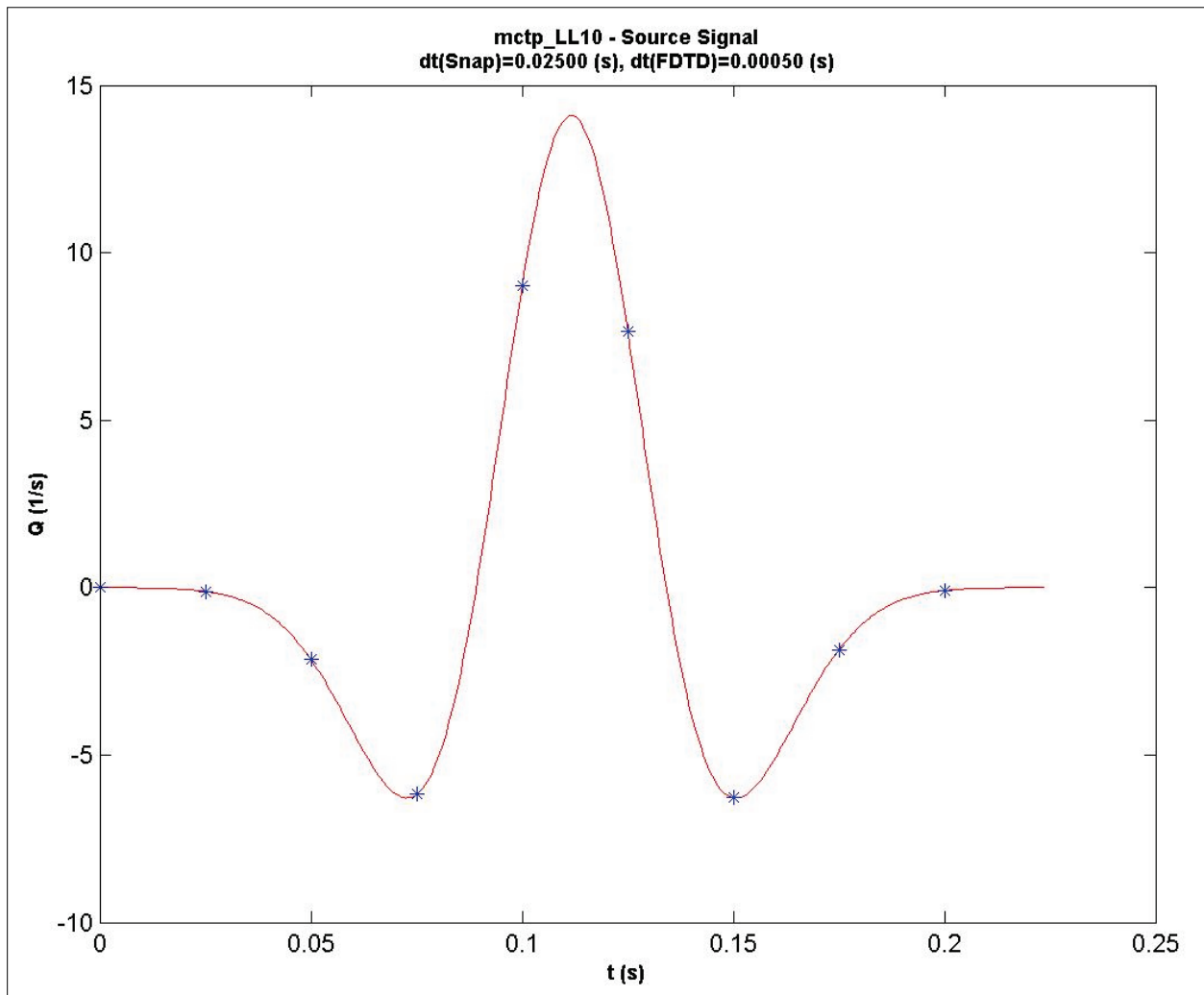
#### 4.4.1 Simplified atmosphere

This model had a simple atmosphere with three layers shown in Table 7. To explore, the model space runs, were completed with simple impulsive sources (5- and 10-Hz Ricker pulses) in the center and corners of the model space (northeast, southeast, southwest, and northwest). An additional validation model run was completed with a 1.66-Hz Ricker pulse at center at the Mockingbird Bridge. The atmosphere profile was fixed to ground in the model. These input sources' frequencies were selected to illustrate the range of previously observed and modeled sources as well as the frequency content of the data set. These frequencies are used to explore the propagation effects of infrasound in the urban terrain and determine if there is a frequency dependence on the effects. Figure 31 is an example of the model input source, which was similar for both the 5-Hz center frequency and 10-Hz center frequency. Model analysis was completed for 10.25 sec to develop peak energy maps over the model area. The peak energy maps are used to highlight spatial effects of the urban-scape, such as highlighting shadow or amplification zones.

Table 7. The simple atmospheric profile used in the propagation model.

Altitude (m)	Density (kg/m <sup>3</sup> )	Effective Sound Speed (m/s) (Temperature Only)
0-50	1.2	344
50-100	1.18	337
100-256	1.13	330

Figure 31. Example of model input source. Pictured is a 10-Hz center frequency Ricker Pulse source.



Limitations of this model are imposed by the grid spacing, the time-step, and the snap interval (sampling frequency) chosen for the simulation (Pace et al. 2015). The model was designed for a maximum frequency of interest of 15 Hz. The grid spacing was designed to capture the geometric detail of the buildings with a spacing of approximately 1 m in all directions, x, y, and z. A minimum of 10 grid nodes are required to capture a wavelength;

therefore, the minimum wavelength is represented by 10 times the maximum grid spacing. The maximum frequency that can be represented in the analysis of the model is 32.9 Hz given by Equation 4 where  $c_{min} = 330$  m/s and  $\Delta s_{max} \approx 1.001$  m. A time-step of 0.0005 sec was selected to account for stability due to the Courant time-step calculation and the instability effect of nonporous materials. The Courant time-step for stability required in x, y, z directions is 0.00175 sec, given by equation 5 with the even grid spacing and  $c_{max} = 330$  m/s. The max snap interval of 66.7 was computed given Equation 6 with the  $\Delta t = 0.0005$  sec and  $f_i = 15$  Hz; therefore a snap interval of 50 was selected. The limiting factors and the maximum analysis frequency for each factor are listed in Table 8. The minimum frequency of the limiting factors limits the model, which is the Snap Interval at 20 Hz.

Maximum frequency:

$$f_{max} = \frac{c_{min}}{10(\Delta s_{max})} \quad (4)$$

where

$c_{min}$  = minimum effective sound speed (m/s)  
 $\Delta s_{max}$  = maximum grid space (m)

Courant time-step:

$$\Delta t = \frac{1}{c_{max} \sqrt{\frac{1}{\Delta x^2} + \frac{1}{\Delta y^2} + \frac{1}{\Delta z^2}}} \quad (5)$$

where

$\Delta t$  = time-step (sec)  
 $c_{max}$  = maximum effective sound speed (m/s)  
 $\Delta x$  = minimum grid spacing x direction (m)  
 $\Delta y$  = minimum grid spacing y direction (m)  
 $\Delta z$  = minimum grid spacing z direction (m)

Snap Interval:

$$\text{Snap Interval} \leq \frac{1}{2 * \Delta t * f_I} \quad (6)$$

where

*Snap Interval* = number of samples that are taken per time-step

$\Delta t$  = time-step (sec)

$f_I$  = maximum frequency of interest (Hz)

**Table 8. The limiting factors for bounding frequency analysis of the simple atmosphere model.**

Limiting Factor	Maximum Frequency for Analysis (Hz)
Grid Spacing	32.9
Time-step	2000
Snap Interval	20

The peak pressure plots for each of the model runs are in Figures 32 through 36. Each of these Figures is for a single source location with the 10-Hz source in the right column and the 5-Hz source in the left column. Shadow zones are highlighted in all the source locations. The easiest to identify area with greatest signal attenuation (shadow zone) is located in the southeast, which is created by a clustering of tall buildings in the model space. The signal strength lost in the shadow zones is a maximum 5 db. The sunken Interstate 75 creates an amplification zone greatest in the higher frequencies, which is highlighted in Figure 36. This waveguide created by the urban-scape creates amplification of the signal up to 20 db. These types of plots can be used to help understand which features of the urban-scape have the greatest effect on infrasound propagation.

Figure 32. Peak pressure maps; Source Location: Center. Right: 10-Hz Source, Left: 5-Hz Source. Color scale - db relative to 1 Pa.

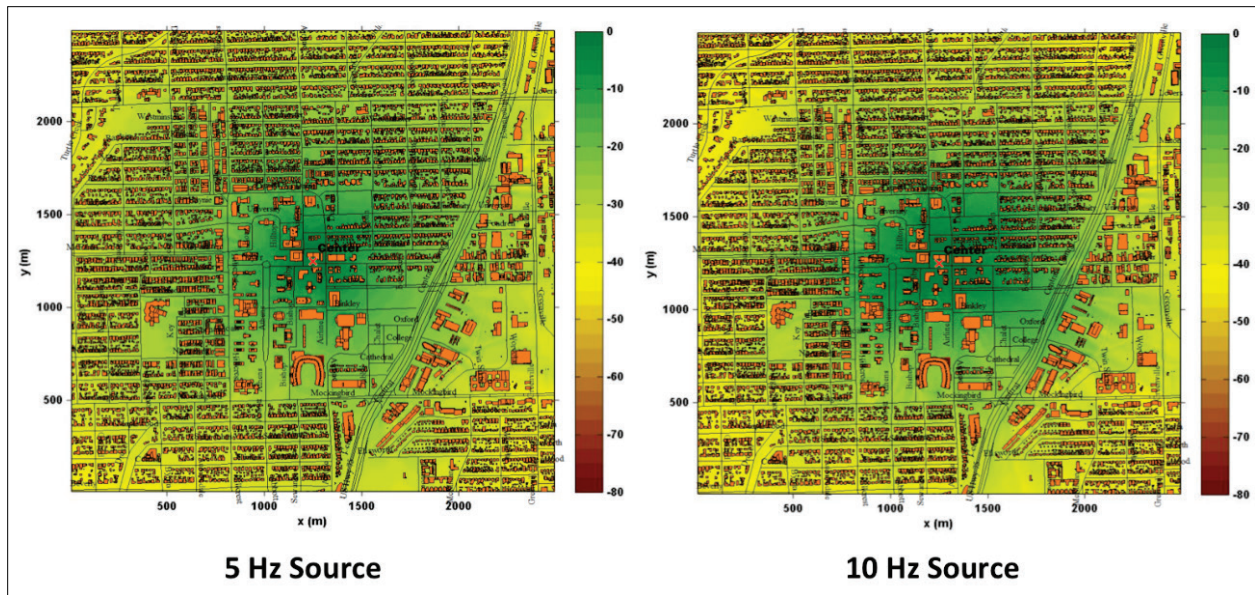


Figure 33. Peak pressure maps; Source Location: Southwest. Right: 10-Hz Source, Left: 5-Hz Source. Color scale - db relative to 1 Pa.

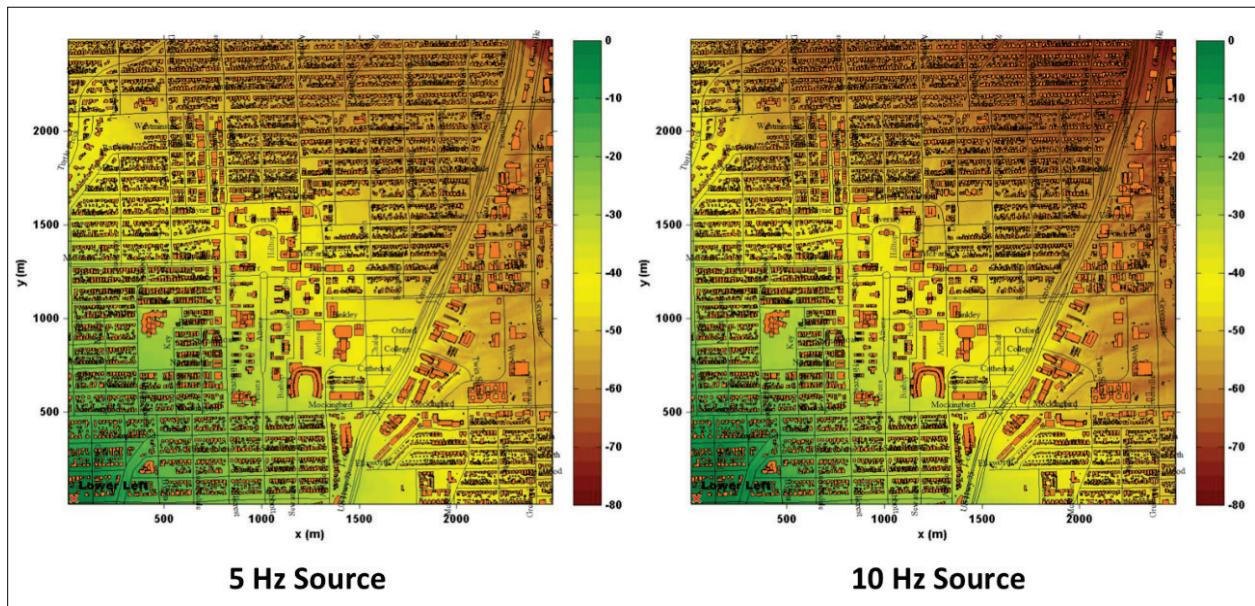


Figure 34. Peak pressure maps; Source Location: Southeast. Right: 10-Hz Source, Left: 5-Hz Source. Color scale – db relative to 1 Pa.

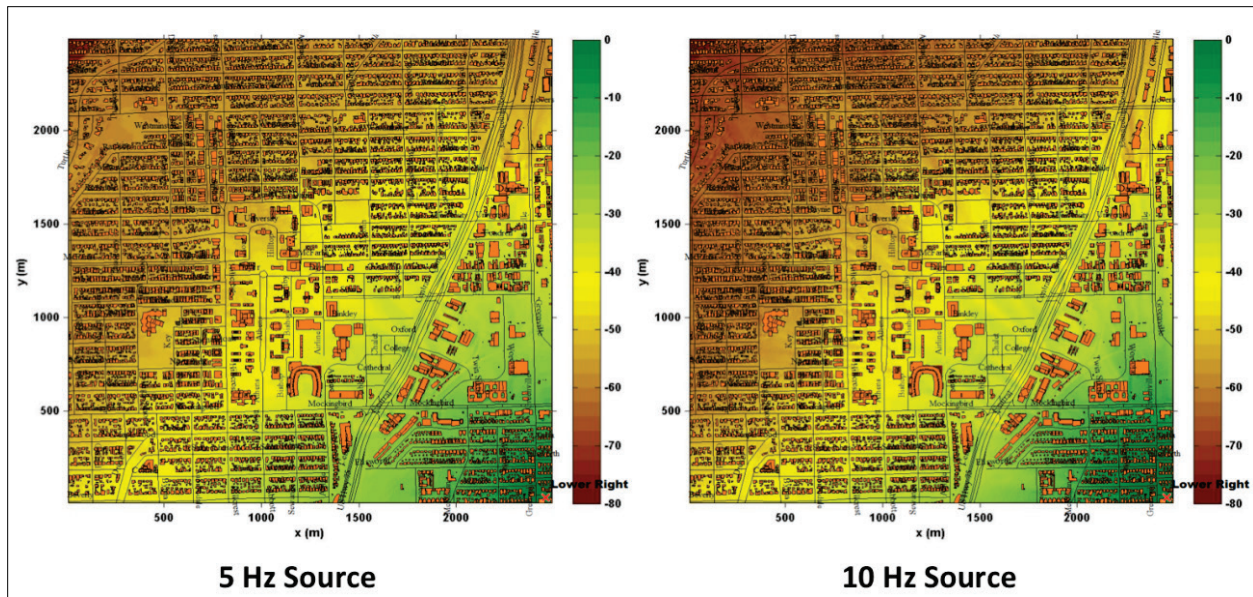


Figure 35. Peak pressure maps; Source Location: Northwest. Right: 10-Hz Source, Left: 5-Hz Source. Color scale – db relative to 1 Pa.

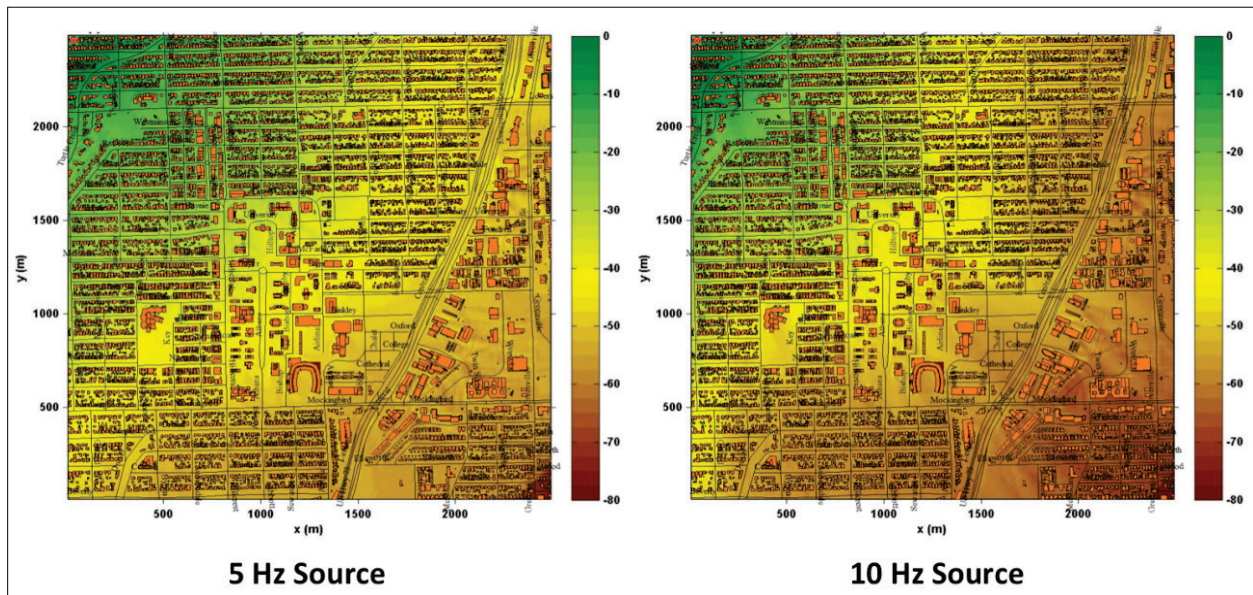
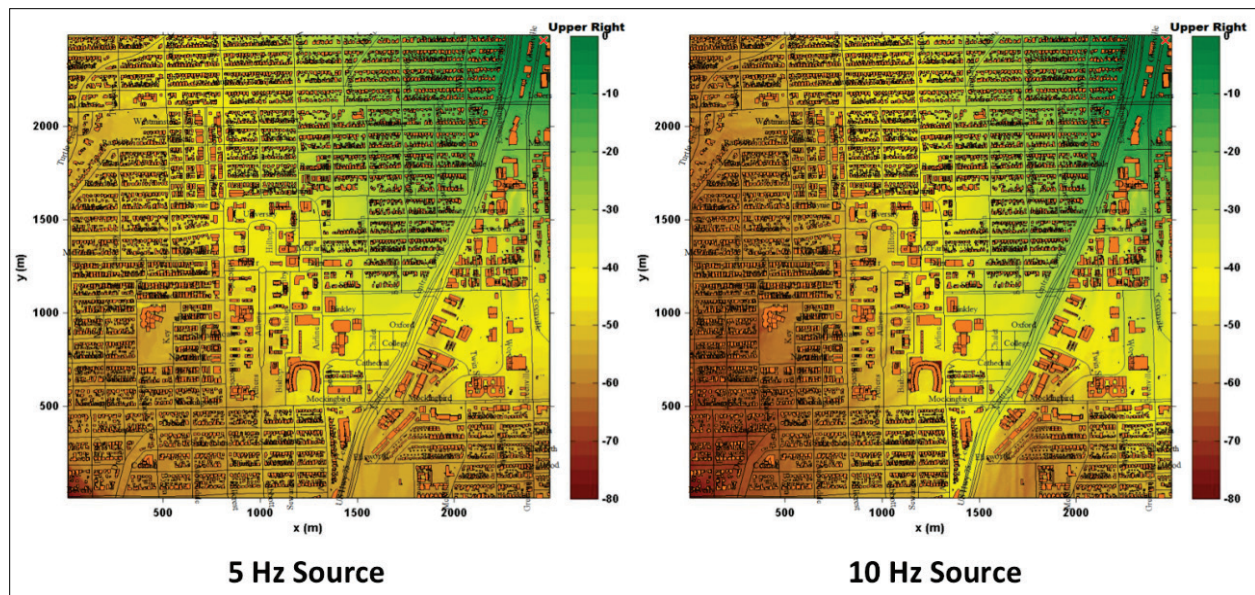


Figure 36. Peak pressure maps; Source Location: Northeast. Right: 10-Hz Source, Left: 5-Hz Source. Color scale – db relative to 1 Pa.



#### 4.4.1.1 Mockingbird Bridge – Wave propagation study

The Mockingbird Bridge source for this study is located in the southeast corner of the model, which is highlighted in pink on Figure 29. For purposes of focusing on propagation path effects, the input source used in the calculation is a Ricker pulse with a center frequency of 1.66 Hz, applied to the center of the north edge of the Mockingbird Bridge (Figure 37). The calculated time series had a length of 10.25 sec. This model allowed for two types of investigations: (1) comparison of model data and observed data and (2) prediction of peak energy over the model space.

##### *Model data versus observed data*

During model runs, receivers were positioned at the locations of the field array on the SMU campus and the associated time series was captured. Frequency analysis of infrasound data is key to identifying the structural source; therefore, the time series data were converted to the frequency domain to determine frequencies that were transmitted to the receivers. Figure 38 displays the modeled time series and power spectra for each building in the urban array. The frequencies with the largest power observed in the model align with the frequencies observed in the real world data. The broader nature of power spectra from the model are expected because of the impulsive nature of the input signal, which is different from

the continuous wave source of the bridge seen in the real world data (Smith 1997). The power spectra for the observed data were narrower since the source was a continuous signal centered on the modes of oscillation of the bridge. The model data spectral estimates may be improved by FT calculated on a shorter window centered on the impulsive signal.

Figure 37. Input source to wave propagation model is a Ricker pulse with a 1.66 Hz center frequency.

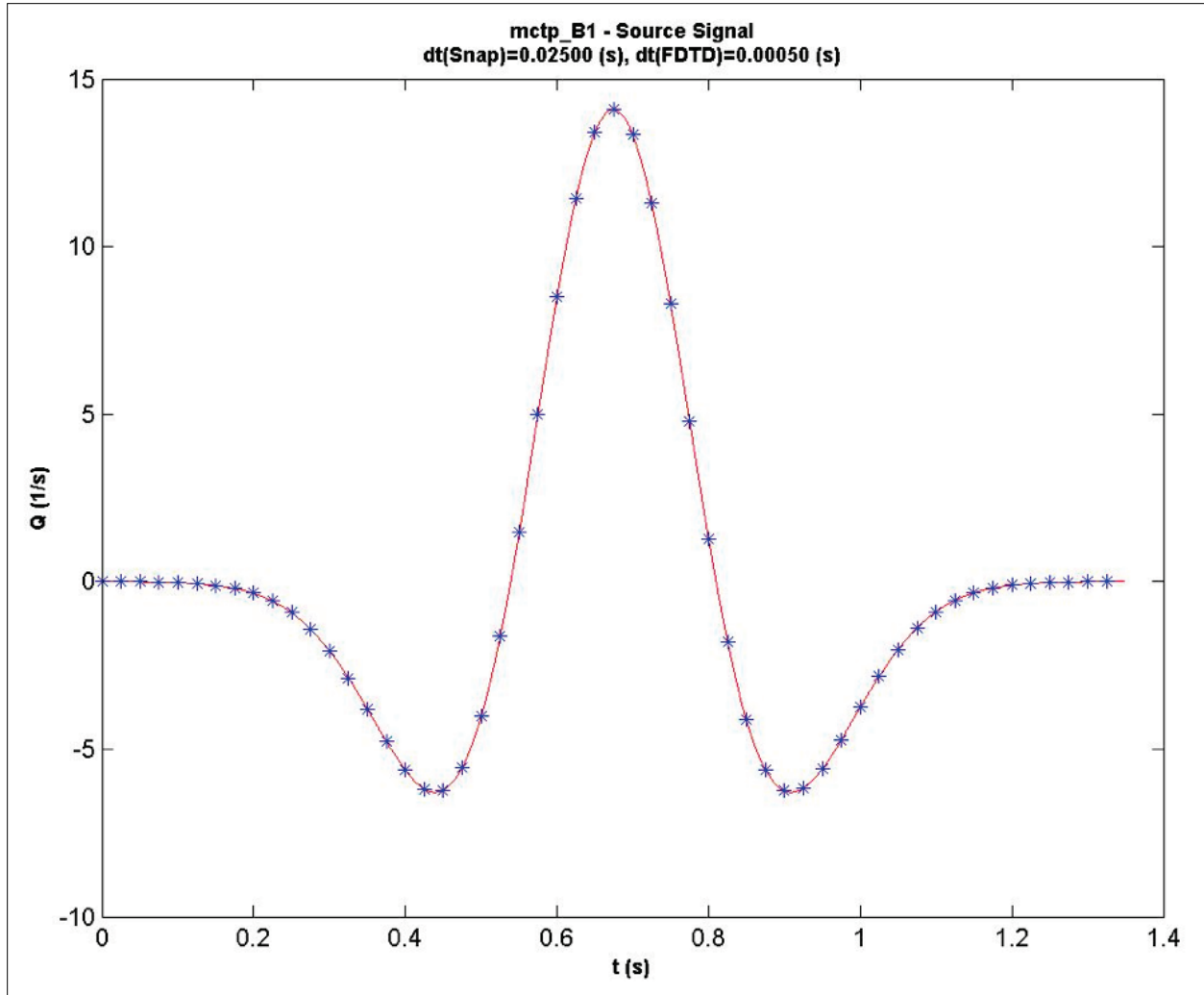
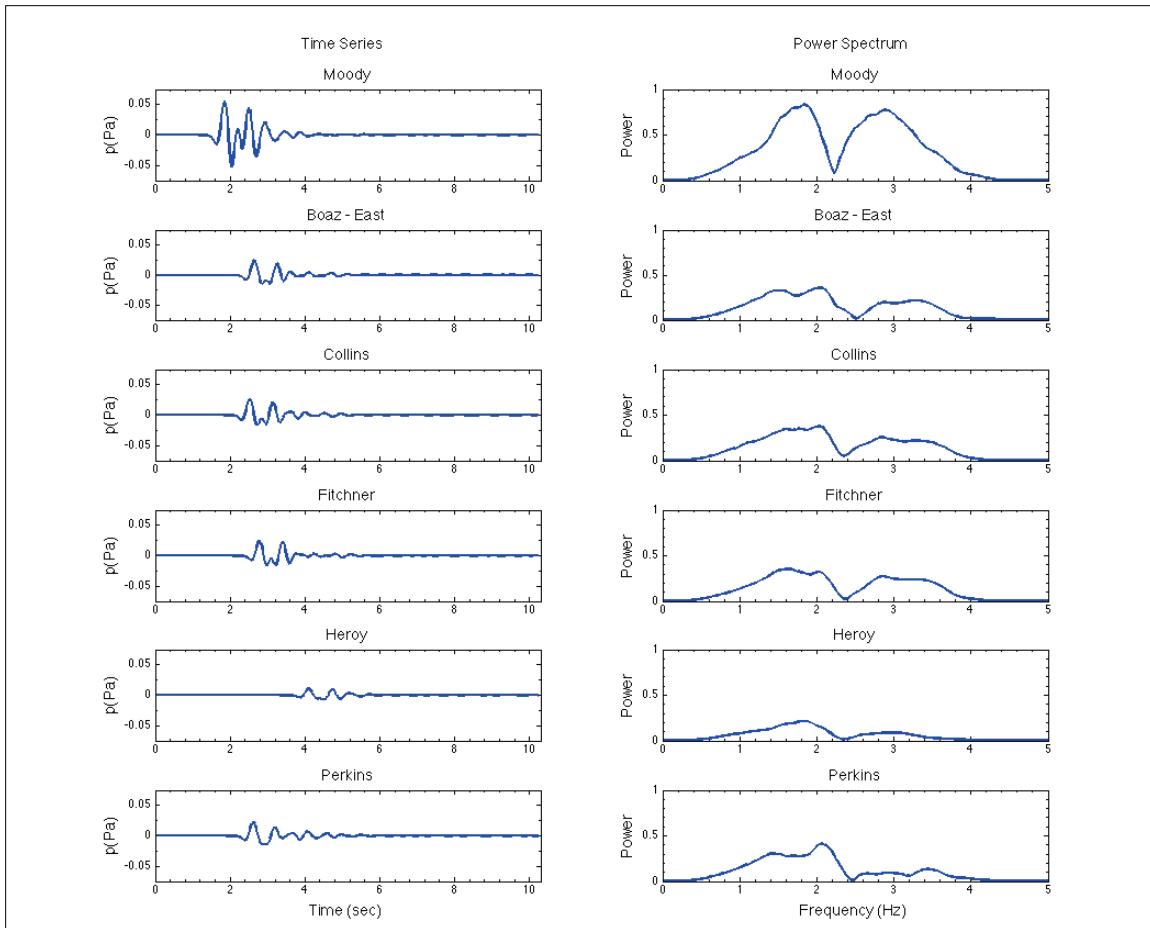


Figure 38. Model output time series and power spectrum for each building in the urban array.

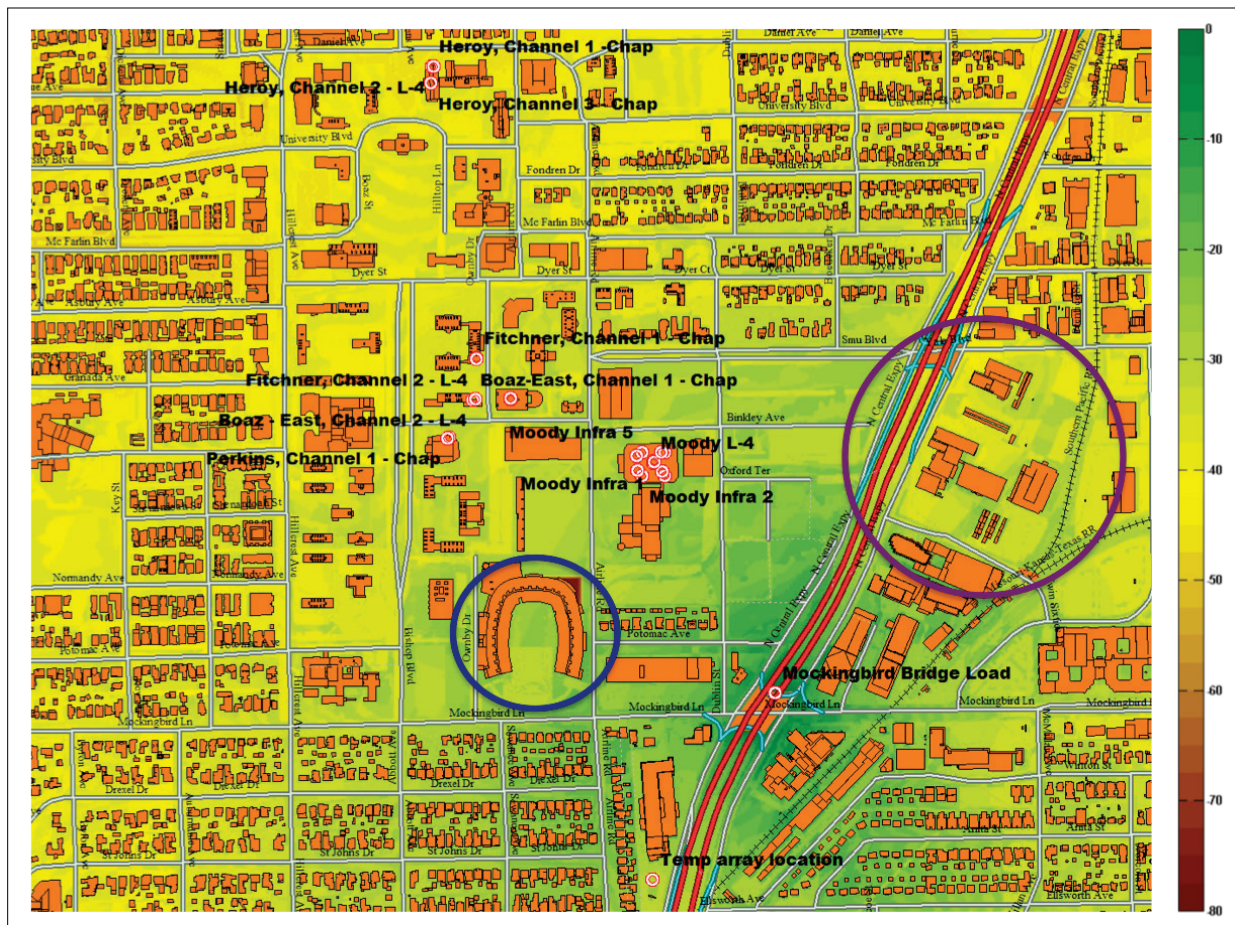


### *Peak energy*

The peak energy was captured over the entire model space for each model run in order to assess spatial effects. The peak energy map also highlights the shadow and amplification zones created in the urban terrain. The peak energy map for the Mockingbird Bridge wave propagation study is shown in Figure 39. Comparison of Moody and Heroy peak energy maps indicates that there would be a lower energy signal at Heroy, which is confirmed with the time series data in Figure 38. This fall-off of energy is expected, based on the spherical spreading of the source. The peak energy map (Figure 39) also highlights shadow and reflection zones created by the urban terrain. An example of a shadow zone is shown in Figure 39 inside the purple circle. This shadow zone is created by a high-rise building that blocks source signal and creates a zone of reduced signal level on the opposite side of the building from the source. An example of a reflection zone is shown in Figure 39 inside the blue circle. This reflection zone is created by the acoustic

energy reflecting off the hard surfaces of the SMU football stadium resulting in signal amplification at the center of the stadium. This type of map will be used for planning future array locations to determine optimum sensor locations. It will also be used after array deployment to determine the feasibility of detection of certain channel sources. The peak energy map helps improve the overall understanding of a how the urban terrain affects acoustic wave propagation.

Figure 39. Peak pressure output over model space zoomed to study area. Color bar is dB relative to 1 Pa. The purple circle highlights a shadow zone from a high-rise building. The blue circle highlights a reflection/amplification zone from the SMU football stadium.



#### 4.4.2 Realistic atmosphere

The realistic atmosphere used for the propagation model was determined through the National Oceanic and Atmospheric Administration (NOAA) Rapid Update Cycle (RUC) data sets, which are determined with horizontal resolution of 13 by 13 km and a variable vertical resolution with spacing

ranging between 30 and 415 m (156 m – 10273 m mean sea level (MSL)). The atmospheric profile input for the model was developed by averaging a subset of the RUC data sets with the ground measurement provided by Dallas Love Field Airport metrological station between 1 July 2013 and 6 July 2013 across the same times of day (Figure 40). The sets of data vary effective sound speed (temperature only) at the ground between 344.8 m/s and 351.4 m/s and at 1 km between 343.2 m/s and 351.4 m/s. There were eight inversions that occurred between the hours of 2300 and 0500 CST in the averaged data set (Figure 41). The effective sound speed (temperature only) data selected for the realistic model runs were the 0500 averaged data set, which contained an inversion. The atmospheric model profile was computed by spline fitting the effective sound speed (temperature only) data, which allows for a smoothly fit data set into 100 layers. The atmosphere profile was fixed to lowest point in model.

Limitations for the realistic atmosphere model vary from the simple model. The limitations still depend on grid spacing of the model, the time-step and the snap interval (sampling frequency) (Pace et al. 2015). The grid spacing in the x- and y-directions is uniformly spaced at approximately 1 m, but the z-grid spacing varies from 1- to 3-m spacing. The 1-m spacing is from grid points 0 to 256 where there is expected to be fine scaled effects from the buildings, grid points 256 – 280 where the spacing linearly increases from 1-m to 3-m spacing, and grid points 280 – 512 where the spacing is 3 m. The max frequency was computed to be 11.46 Hz, given by Equation 4 with  $c_{min} = 343.8$  m/s and  $\Delta s_{max} \approx 3$  m. The same time-step and snap interval will be used for the realistic model as the simple model. The limiting factors and the maximum analysis frequency for each factor are listed in Table 9. The minimum frequency of the limiting factors limits the model, which is the grid spacing at 11.46 Hz.

The effect of a realistic atmosphere as compared to the simplified atmosphere model was completed using the 5-Hz Ricker input pulse in the northeast corner of the urban terrain model. The simplified atmosphere was expanded to 1 km by extending the upper layer to 1 km, which allowed for direct comparison with the 1-km realistic atmosphere. The peak pressure output of the simplified atmosphere model (Figure 42) and the realistic atmosphere model (Figure 43) highlights increase in signal strength over the entire model space, starting at ~700-m radius from the source. The difference of the peak pressure outputs (Figure 44) referenced to the simplified atmosphere highlights the increase in peak pressure of 4 dB at

~100-m radius to the source location, then increase up to a maximum of 6 dB at ~500-m radius from source location. Cross sections of the peak pressure difference output (Figures 45 and 46) highlight two features, the Urban Heat Island Effect and directional effects.

Figure 40. Effective sound speed (temperature only) plots that were averaged hours for five days between 7/1/13 0:00 and 7/5/13 UTC (6/30/13 18:00 to 7/5/13 17:00 CST). The ground measurement is provided by the Love Field Airport metrological station and the upper points are provided by NOAA RUC data sets.

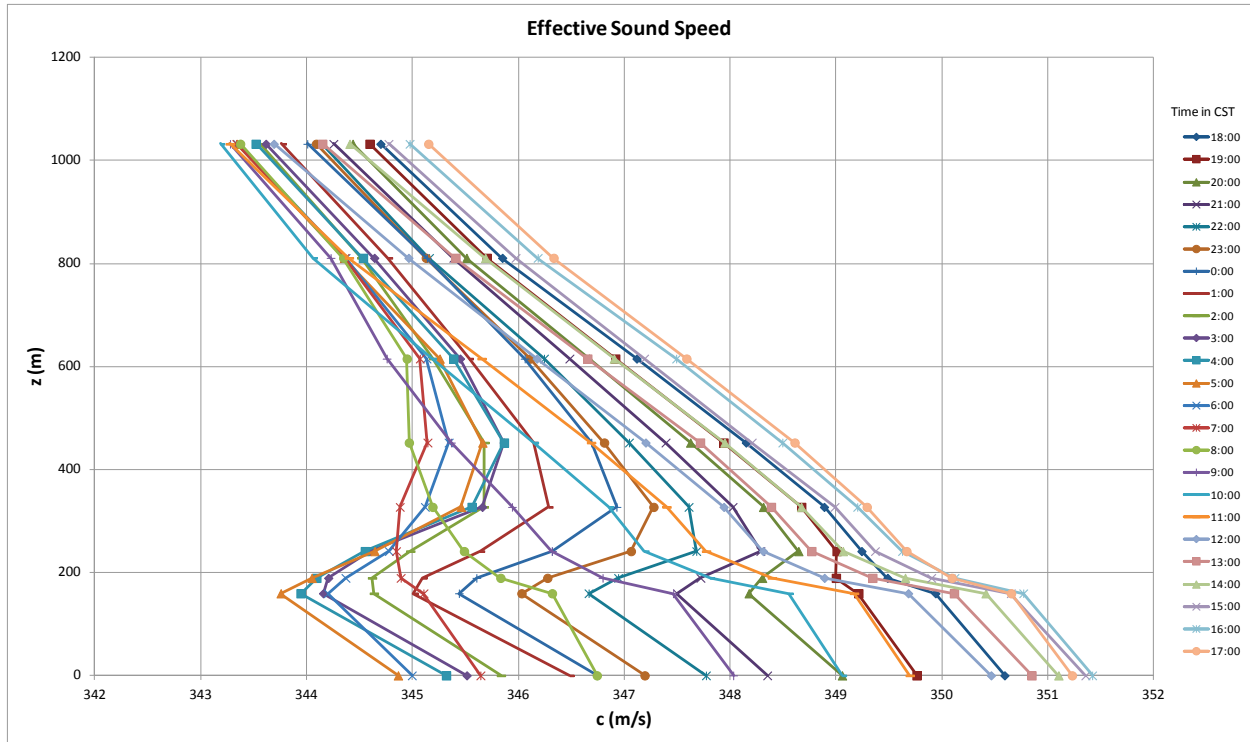


Figure 41. Effective sound speed (temperature only) plots that were averaged hours for five days between 7/1/13 0:00 and 7/5/13 UTC (6/30/13 18:00 to 7/5/13 17:00 CST). The ground measurement is provided by the Love Field Airport metrological station and the upper points are provided by NOAA RUC data sets.

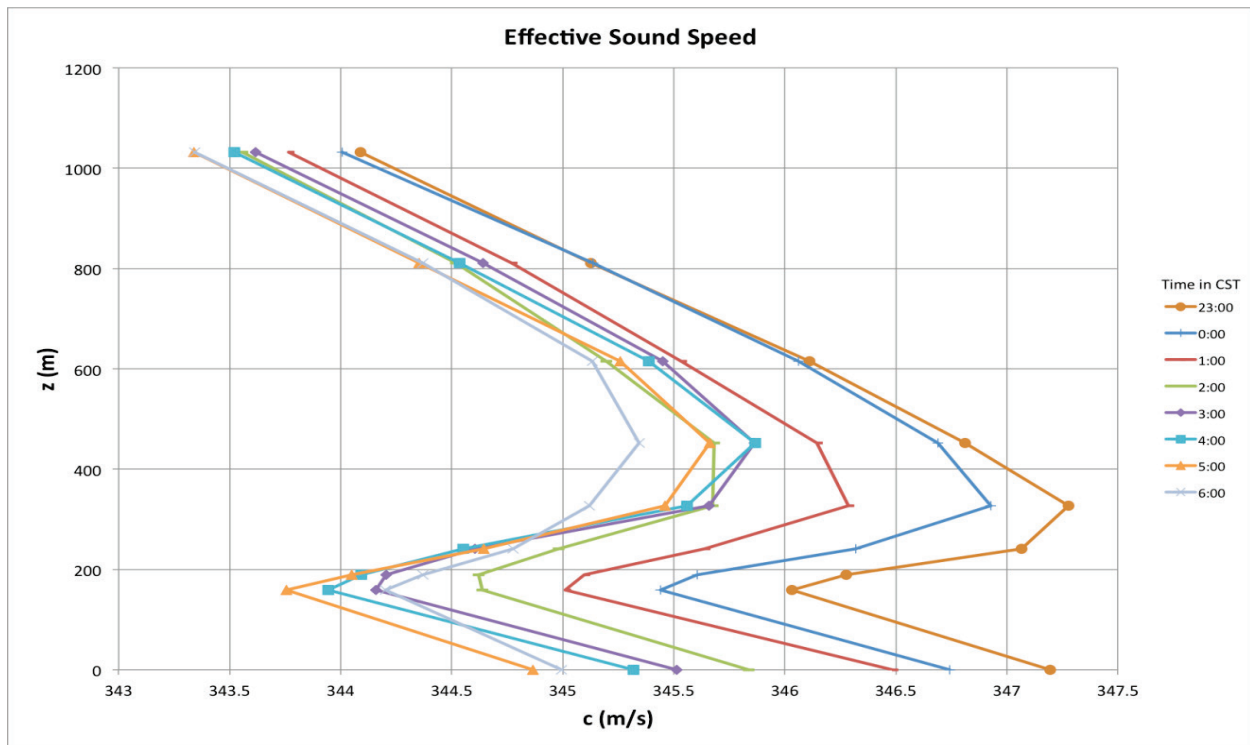


Table 9. The limiting factors for bounding frequency analysis of the realistic atmosphere model.

Limiting Factor	Maximum Frequency for Analysis (Hz)
Grid Spacing	11.46
Time-step	2000
Snap Interval	20





Figure 44. Peak pressure difference between the simplified atmosphere model and the realistic atmosphere model relative to the simplified model.

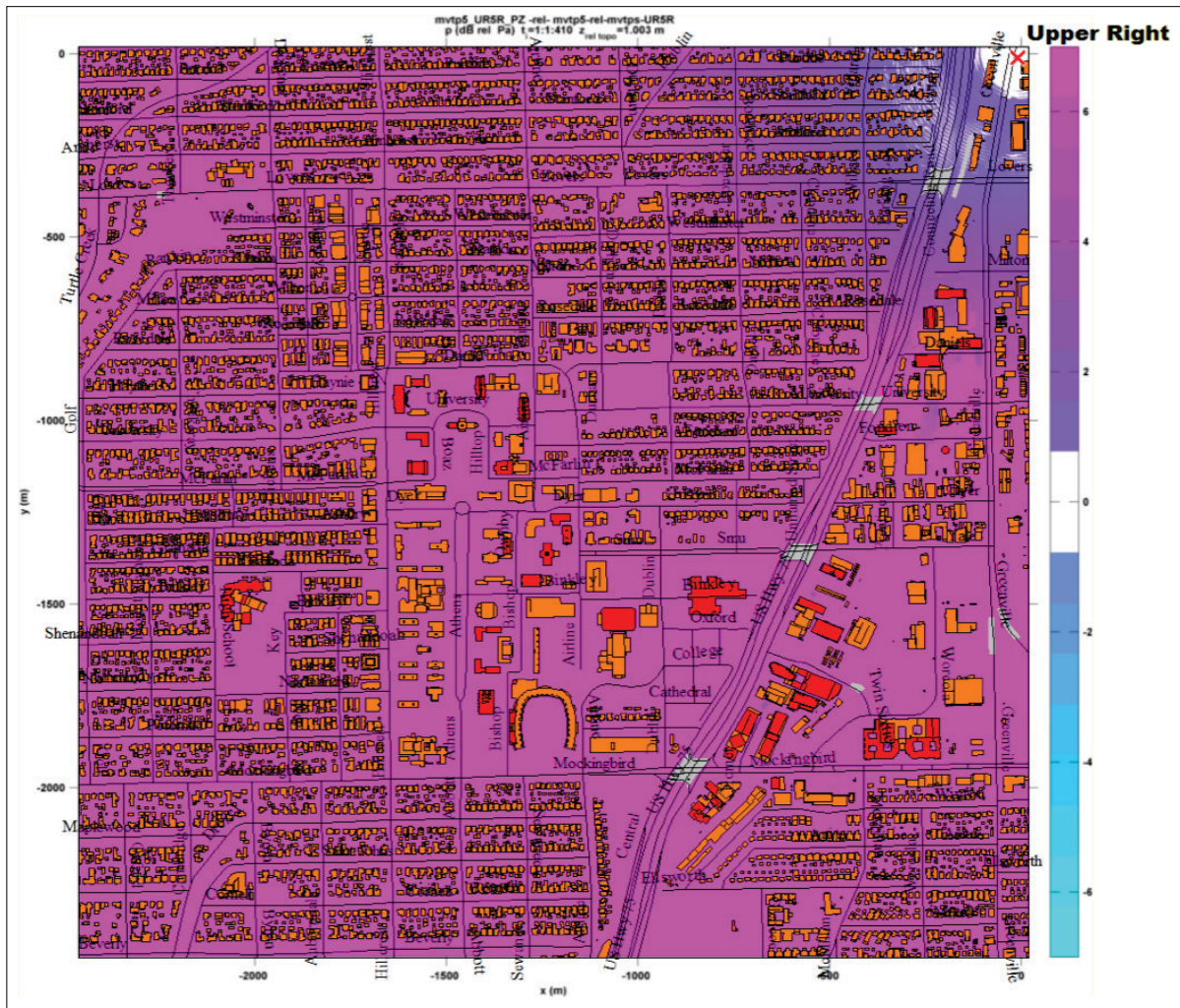


Figure 45. A cross-section view of the peak pressure difference between the simplified atmosphere model and the realistic atmosphere model; relative to the simplified model. The 0-m location is the northeast corner of the model and the 2,500-m location is the southeast corner of the model.

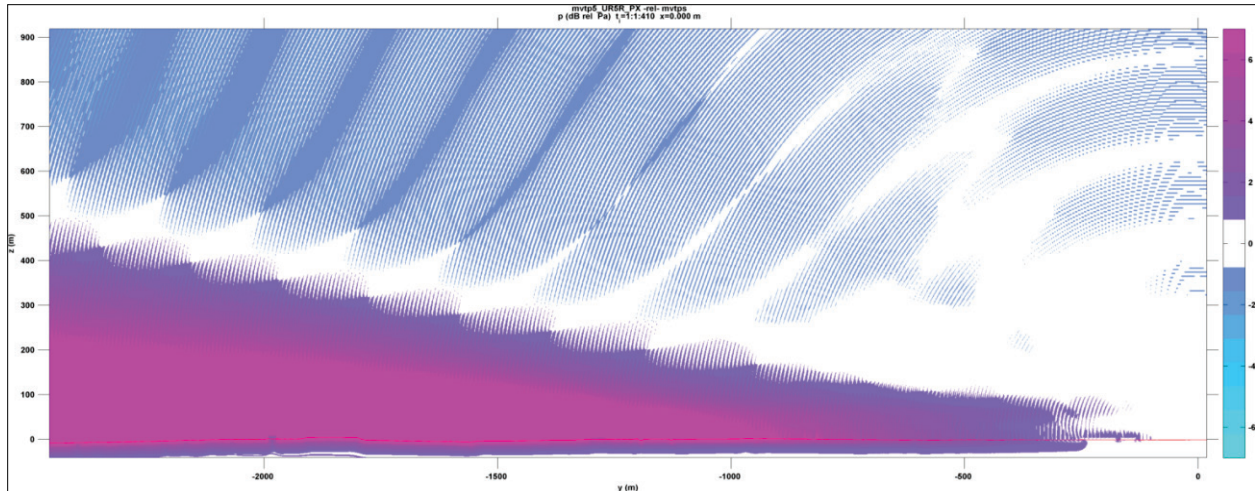
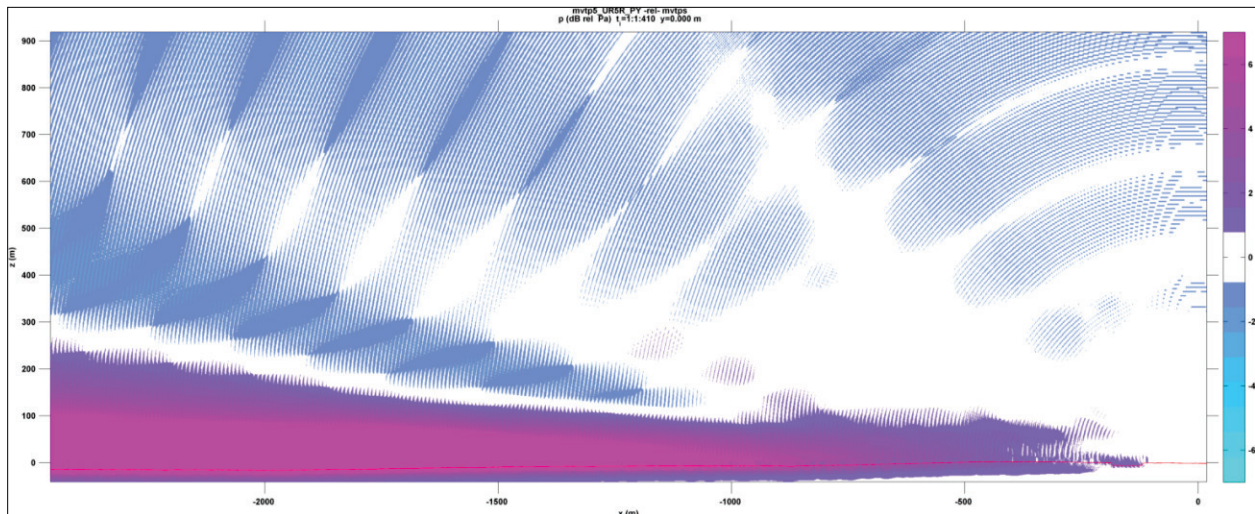


Figure 46. A cross-section view of the peak pressure difference between the simplified atmosphere model and the realistic atmosphere model; relative to the simplified model. The 0-m location is the northeast corner of the model and the 2,500-m location is the northwest corner of the model.



The Heat Island Effect is highlighted in these figures by the upper atmosphere having the majority of its energy dominated by the simplified atmosphere profile (blues on the color bar) and the lower atmosphere having the majority of its energy dominated by the realistic atmosphere profile (pinks and purples on the color bar). This energy dominated in the lower atmosphere is expected due to the low atmosphere inversion in the realistic atmosphere profile, which provides a pathway for energy to return to the ground.

The directional effects are highlighted in the northeast/southeast cross section with the linearly increasing elevation relationship between distance from source and increase in peak pressure output that is observed up to ~400-m elevation; and the northeast/southeast cross section with the increase in peak pressure extends up to approximately twice the observation on the northeast/northwest cross section. This directional dependence could be related to type of infrastructure or topography along the propagation path. The northeast/northwest cross section traverses mainly residential areas and decreases by ~50-ft<sup>1</sup> in elevation from northeast to northwest. The northeast/southeast cross section traverses commercial, residential, and open (parking lots, power substations, parks) areas and varies in elevation by ~25 ft with the highest point ~1 km from the northeast corner. These effects could be further explored with knowledge from Swearingen et al. 2013 investigation of forest density versus observed infrasound propagation path effects. The research indicated that forest layers provide a waveguide for energy, but the parameters of the waveguide depend on the spacing of trees in the forest. Perhaps these relationships could be further expanded to urban areas with various building spacing, such as dense residential, sparse commercial, or sparse residential.

---

<sup>1</sup> Elevation data was collected from Google Earth Pro digital elevation model.

## 5 Conclusions and Implications

This experiment has shown a rich infrasonic environment in the urban setting that can be successfully monitored using modified infrasound arrays located on building rooftops. The two arrays presented in this paper detected the fundamental vibrational modes of two bridges at a distance of approximately 2 km. These sources allowed for successful demonstration of detection and source verification techniques (modeling and direct measurement). While the data set indicated additional sources, these sources were not investigated for full source characterization due to the limited time and scope of this study.

The wave propagation study presented herein provides methods of evaluating sensor locations before array deployment to determine if the urban terrain will affect signal propagation. An example of this is given in Figure 39 where signal shadowing from high-rise structures and signal amplification/reflection from the horseshoe-shaped sunken stadium are observed in the wave propagation study. This study also highlighted the importance for understanding propagation effects unique to urban-scapes, such as the Urban Heat Island or terrain.

This research demonstrates the ability to effectively deploy infrasound arrays in an urban setting, an area traditionally thought closed due to the abundance of infrasonic sources and noise levels. The ability to deploy arrays in urban settings will allow the infrasound community to branch into new research areas such as infrastructure monitoring for post-event prioritization or pre-planning purposes.

### 5.1 Future work

#### 5.1.1 Rooftop arrays

Further study of the rooftop array data will be completed to determine seasonal trends of the overall ambient acoustical field after the trend analysis is completed. It will then be determined if the trends can be related to the Urban Heat Island Effect.

After further understanding of the seasonality of the ambient acoustic field, work could be completed on developing an automated detection algorithm for structural sources, which could be refined to identify structures that are currently below the background noise level.

### **5.1.2 Wave propagation study**

The urban terrain model developed for the wave propagation study currently has a significant level of detail in the buildings. During the next iteration of this study, there will be a review of how to reduce the level of detail required for buildings, looking towards breaking down urban areas into urban terrain zones. Within a given Urban Terrain Zone (UTZ), such as suburban, this research would develop a set of model properties to represent that area rather than define each individual building. This would allow for expedient modeling of urban areas at lower computational cost.

Urban terrain propagation effects will continue to be explored by varying the atmosphere profile for seasonality, such as a winter profile with a stronger inversion, and investigating the terrain/infrastructure effects that were observed in the realistic atmosphere model results.

## References

- Arrowsmith, S. J., and D. O. ReVelle. 2007. Infrasound monitoring of local, regional and global events. *Proceedings of the 29th monitoring research review: Ground-based nuclear explosion monitoring technologies*, Denver CO, 25-27 Sep 2007.
- Bedard, A. J., Jr. 2000. Detection of infrasound from natural and civilization sources: Measurement of complex signal/noise environments. *Geosciences and Remote Sensing Symposium. IGRASS 2000. IEEE 2000 International*, 3: 1195-1197, 2000.
- Bedard, A. J., Jr., and T. M. Georges. 2000. Atmospheric infrasound. *Physics Today* 53, 32.
- Campus, P., and D. R. Christie. 2010. Worldwide observations of infrasonic waves. In *Infrasound Monitoring for Atmospheric Studies*, ed. A. Le Pichon, E. Blanc, and A. Hauchecorne, 185-234, Springer Dordrecht.
- Chopra, A. 2001. *Dynamics of structures - Theory and applications to earthquake engineering*, 2nd ed., 844 pp., Upper Saddle River, NJ: Prentice Hall.
- Christie, D. R., and P. Campus. 2010. The IMS infrasound network: Design and establishment of infrasound stations. In *Infrasound monitoring for atmospheric studies*, ed. A. Le Pichon, E. Blanc, and A. Hauchecorne, 29-75, Springer Dordrecht.
- Coyne, J. M. and I. Henson 1995. Geotool sourcebook: User's manual. PL-TR-96-2021, Hanscom AFB MA: Phillips Laboratory, Directorate of Geophysics, Air Force Materiel Command.
- Donn, W. 1974. Atmospheric infrasound radiated by bridges. *Journal of the Acoustical Society of America*, 56:1367-1370.
- Drob, D. P., J. M. Picone, and M. Garcés. 2003. Global morphology of infrasound propagation. *Journal of Geophysical Research: Atmospheres* 108, -4680.
- Guzas, D., and V. Tricys. 2010. Noise in european railway under modernization and its reduction. *Journal of Vibroengineering* 12:649-656.
- Hedin, A. E., E. L. Flemming, A. H. Manson, F. J. Schmidlin, S.K. Avery, R. R. Clark, S. J. Franke, G. J. Fraser, T. Tsuda, F. Vial, and R. A. Vincent. 1996. Empirical wind model for the upper, middle and lower atmosphere. *J. Atmos. Terr. Phys.* 58:1421-1447.
- Hedlin, M. A. H., K. Walker, D. P. Drob, and C. D. de Groot-Hedlin. 2012. Infrasound: Connecting the Solid earth, oceans, and atmosphere, *The Annual Review of Earth and Planetary Sciences*, 327-354.
- Hidalgo, J., V. Masson, A. Baklanov, G. Pigeon, and L. Gimeno. 2008. Advances in urban climate modeling. *Ann. N. Y. Acad. Sci.* 1146:354-374.

- Intellicast.com. 2014. Intellicast.com - Historical averages Dallas, TX. 2014. <http://www.intellicast.com/Local/History.aspx?location=USTX0327>.
- Jacobs, W. 2008. Building periods: Moving forward (and backward), *Structure Magazine*, 24-27.
- Jordan, A. M., R. D. Costley, H. Diaz-Alvarez, M. H. McKenna, and C. P. Simpson. 2013. *Standoff assessment of infrastructure program: Analysis of barge impact with bridge pier*. ERDC/GSL TR-13-40. Vicksburg MS: U.S. Army Engineer Research and Development Center.
- Ketcham, S. A., J. Lacombe, T. S. Anderson, and M. L. Moran. 2005. Seismic propagation from humans in open and urban terrain. *Users Group Conference, DoD High Performance Computing Modernization Program, IEEE Computer Society*, 270-277.
- Ketcham, S. A., M. Q. Phan, R. S. Darling, and M. McKenna. 2013. Realization of state-space models for wave propagation simulations. *Advances in the Astronautical Sciences* 147.
- McKenna, M., B. Stump, S. Hayek, J. McKenna, and T. Stanton. 2007. Tele-infrasound studies of hard-rock mining explosions. *J. Acoust. Soc. Am.* 122:97-106.
- McKenna, M. H., B. W. Stump, and C. Hayward. 2008. Effect of time-varying tropospheric models on near-regional and regional infrasound propagation as constrained by observational data. *Journal of Geophysical Research: Atmospheres* 113:D11111.
- McKenna, M., A. Lester, and S. McComas. 2009a. *Infrasound assessment of infrastructure; Report 2, Experimental infrasound measurements of railroad bridge A.B 0.3, Ft. Leonard Wood, MO*, ERDC/GSL TR-09-16. Vicksburg MS: U.S. Army Engineer Research and Development Center.
- McKenna, M., K. Koppenhoefer, and A. Lester. 2009b. Numerical simulation of structural-acoustic (infrasound) coupling with validation from observational data. In *Proceedings of the 2009 Meeting of the Military Sensing Symposia Specialty Group on Battlespace Acoustic and Seismic, Magnetic and Electric Field Sensors, Laurel, MD, August, 2009*.
- McKenna, M. H., S. McComas, A. Lester, and P. Mlakar. 2009c. Infrasound measurements of a railroad bridge. *22nd Symp., Application of Geophysics to Engineering and Environmental Problems, Society of Exploration Geophysicists*, Fort Worth, TX.
- McKenna, M., J. Clay, D. Salzberg, and S. Clay. 2011. Infrasound hose-filter evaluation. In *Proceedings of the 2011 Meeting of the Military Sensing Symposia Specialty Group on Battlespace Acoustic and Seismic, Magnetic and Electric Field Sensors*, October, 2011.
- McKenna, M. H., R. G. Gibson, B. E. Walker, J. McKenna, N. W. Winslow, and A. S. Kofford. 2012. Topographic effects on infrasound propagation. *J. Acoust. Soc. Am.* 131:35-46.

- McKisic, J. M. 1997. *Infrasound and the infrasonic monitoring of atmospheric nuclear explosions: A literature review*. Phillips Laboratory Technical Report, PL-TR-96-2190, Hanscom AFB, MA.
- Pace, M. E., S. L. McComas, and M. H. McKenna. 2015. *Modeling an urban environment for acoustical analyses using the 3D finite-difference time-domain program PSTOP3D. Report 1*. ERDC TR-15-5. Vicksburg MS: U.S. Army Engineer Research and Development Center
- Picone, J. M., A. E. Hedin, D. P. Drob, and A. C. Aikin. 2002. NRLMSISE-00 empirical model of the atmosphere: Statistical comparisons and scientific issues, *Journal of Geophysical Research: Space Physics* 107, - 1468.
- Rost, S., and C. Thomas. 2002. Array seismology: Methods and applications. *Reviews of Geophysics* 40, 2-1-2-27.
- Schweitzer, J., J. Fyen, S. Mykkeltveit, S. Gibbons, M. Pirli, D. Kuhn, and T. Kvaerna. 2011. Chapter 9 - Seismic arrays. In *New manual of seismological observatory practice (NMSOP-2)*, 2<sup>nd</sup> ed., ed. German Research Centre for Geosciences.
- Smith, S. 1997. *The scientist and engineer's guide to digital signal processing*. San Diego, CA: California Technical Publishing.
- Stubbs, C., M. Brenner, L. Blidsten, P. Dimotakis, S. Flatte, J. Goodman, B. Hearing, C. Max, R. Schwitters, and J. Tonry. 2005. Tactical Infrasound. *JSR-03-520*. McLean, VA: The MITRE Corp.
- Swearingen, M. E., M. J. White, S. A. Ketcham, and M. H. McKenna. 2013. Use of a porous material description of forests in infrasonic propagation algorithms. *J. Acoust. Soc. Am.* 134(4):2647-2659, doi: <http://dx.doi.org/10.1121/1.4818742>.
- Taylor, O., R. Whitlow, and M. McKenna. 2013. Scour detection and riverine health assessment using infrasound. In *Proceedings of the 26<sup>th</sup> Symposium on the Application of Geophysics to Engineering and Environmental Problems*, Denver, CO, April 2013.
- TX DOT. 1993. As Built Drawings: Dallas County US 75 Section S-2 (State Project C47-7-120), Jan 2013. Austin TX: Texas Department of Transportation.
- Whitlow, R., O. Taylor, M. McKenna, and M. Quinn. 2013. *Infrasound assessment of infrastructure; Report 4: Scour detection and riverine health assessment using infrasound*. ERDC/GSL TR-09-16. Vicksburg, MS: U.S. Army Engineer Research and Development Center.
- Wilson, D., and L. Liu. 2004. *Finite-difference, time-domain simulation of sound propagation in a dynamic atmosphere*. ERDC-CRREL Technical Report TR04-12. Hanover, NH: U.S. Army Engineer Research and Development Center.
- Wunderground.com. 2012. Weather underground - History for Dallas Love, TX, 2013, <http://www.wunderground.com/history/airport/KDAL/>.

## Appendix A: Field Deployment Photographs

Appendix A has full size photographs of Moody and multi-rooftop array deployments.

Figure A1. Overview map for array deployment sites, highlighting building names.

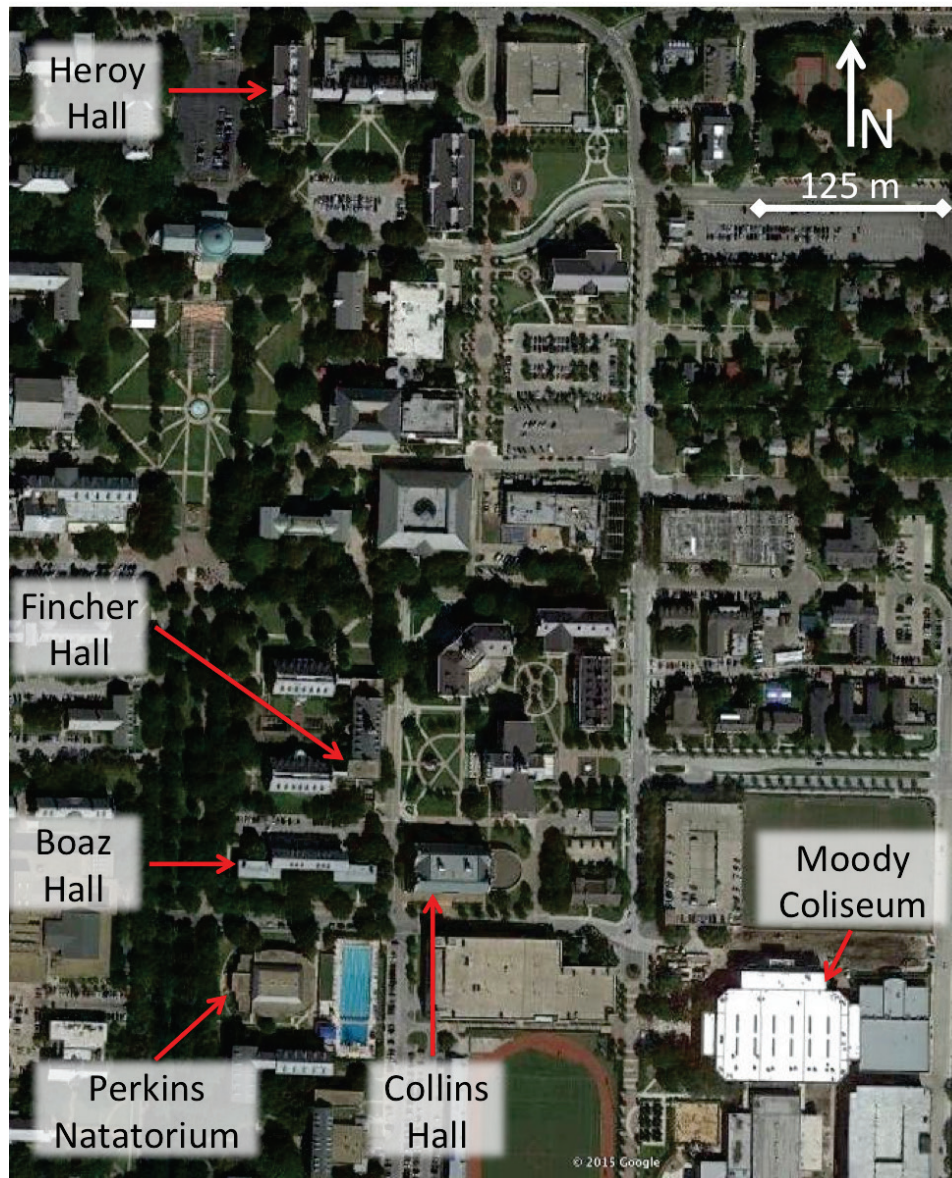


Figure A2. Moody array – Channel 1.



Figure A3. Moody array – Channel 2.



Figure A4. Moody array – Channel 3.



Figure A5. Moody array – Channel 4.



Figure A6. Moody array – Channel 5.



Figure A7. Multi-rooftop array at Perkins Hall.



Figure A8. Multi-rooftop array at Boaz Hall.



Figure A9. Multi-rooftop array Collins Hall.



Figure A10. Multi-rooftop array at Finchner Hall.



## **Appendix B: Channel Map**

Table B1. Rooftop array installation locations and the channel map for each array elements.

Location	Latitude	Longitude	Altitude (km)	Digitizer S/N	Digitizer Channel Number	Sensor Type	Sensor S/N
Boaz-East, Channel 1 - Chap	32.8413921	-96.7837202	0.1876	9EAF	1	Chaparral	5
Boaz - East, Channel 2 - L-4	32.8413991	-96.7836789	0.1854	9EAF	2	Mark L-4 Vertical	8071
Moody, Channel 1 - Chap	32.8404129	-96.7805363	0.1926	98E4	1	Chaparral	14
Moody, Channel 2 - Chap	32.8402667	-96.780836	0.196	98E4	2	Chaparral	13
Moody, Channel 3 - Chap	32.8402571	-96.7803901	0.1965	98E4	3	Chaparral	11
Moody, Channel 6 - L-4	32.8404006	-96.7805331	0.1989	98E4	6	Mark L-4 Vertical	8069
Moody, Channel 4 - Chap	32.840546	-96.7803973	0.1965	98E4	4	Chaparral	9
Moody, Channel 5 - Chap	32.8405029	-96.7808413	0.1955	98E4	5	Chaparral	8
Collins, Channel 1 - Chap	32.8413933	-96.7830514	0.1996	9473	1	Chaparral	10
Collins, Channel 2 - L-4	32.8414041	-96.783057	0.1996	9473	2	Mark L-4 Vertical	3121
Fincher, Channel 1 - Chap	32.8420106	-96.7836498	0.1883	9FD9	1	Chaparral	2
Fincher, Channel 2 - L-4	32.8420064	-96.7836486	0.1888	9FD9	2	Mark L-4 Vertical	8101
Heroy, Channel 1 - Chap	32.8464328	-96.7843327	0.2073	9C28	1	Chaparral	n/a
Heroy, Channel 2 - L-4	32.8464298	-96.7842936	0.2073	9C28	2	Mark L-4 Vertical	n/a
Heroy, Channel 3 - Chap	32.8461754	-96.7843457	0.2073	9C28	3	Chaparral	12
Perkins, Channel 1 - Chap	32.8408288	-96.7841517	0.1727	9E29	1	Chaparral	3
Perkins, Channel 2 - L-4	32.840815	-96.7841941	0.1741	9E29	2	Mark L-4 Vertical	8067
Boaz - West, Channel 1 - Chap	32.8413867	-96.7845217	0.1876	9C2A	1	Chaparral	n/a
Boaz - West, Channel 2 - L-4	32.8413867	-96.7845217	0.1876	9C2A	2	Mark L-4 Vertical	n/a

## **Appendix C: Detection Data**

Metadata for detection data

- Channel Label HDF indicates 200 Hz sampled channel
- Time recorded in Coordinated Universal Time (UTC)
- Event Type - Continuous Wave (CW), Impulsive (IMP), Other (OTH)

Table C1. Detection data from rooftop arrays.

ID	Related ID	BOZE	BOZW	COLL	FNC	PERK	MOOD1	MOOD2	MOOD3	MOOD4	MOOD5	Date	Julian Day	Start time	Duration	End time	Noise Start time	Event type	Frequencies (Hz)	Apparent Velocity (km/sec)	Azimuth	F-stat	SNR	
1							HDF	HDF	HDF	HDF	HDF	2/1/13	032	07:40:18.00	00:00:15.00	07:40:33.00	07:39:16.30	CW	1.6602	0.300	441.55	0.90	2.01	
2							HDF	HDF	HDF	HDF	HDF	9/9/12	253	00:06:37.28	00:00:06.00	00:06:43.28	00:06:30.99	CW	1.6602	0.319	152.301	5.00	1.38	
3							HDF	HDF	HDF	HDF	HDF	9/9/12	253	00:11:20.00	00:00:10.00	00:11:21.00	00:11:40.00	CW	1.6602	0.343	136.094	9.80	2.25	
4							HDF	HDF	HDF	HDF	HDF	9/9/12	253	00:16:56.20	00:00:08.00	00:17:04.20	00:16:47.00	CW						
5							HDF	HDF	HDF	HDF	HDF	9/9/12	253	00:40:49.80	00:00:15.00	00:41:04.80	00:40:33.90	CW						
6							HDF	HDF	HDF	HDF	HDF	9/9/12	253	01:02:20.00	00:00:09.00	01:02:29.00	01:02:20.00	CW	1.6602	0.316	133.583	11.70	3.12	
7	77						HDF	HDF	HDF	HDF	HDF	9/9/12	253	01:17:42.09	00:00:06.00	01:17:42.09	01:17:25.42	CW	1.6602-1.7578	0.384	135.983	6.00	2.49	
8	88						HDF	HDF	HDF	HDF	HDF	9/9/12	253	01:22:53.68	00:00:12.50	01:23:06.18	01:22:39.70	CW	1.6602	0.350	142.406	10.10	2.67	
9	89						HDF	HDF	HDF	HDF	HDF	9/9/12	253	01:38:34.38	00:00:10.00	01:38:44.38	01:38:11.65	CW	1.6602	0.445	146.605	10.10	2.67	
10							HDF	HDF	HDF	HDF	HDF	9/9/12	253	01:48:59.98	00:00:05.00	01:49:04.98	01:49:07.07	CW	1.6602	0.330	137.760	38.60	2.99	
11	1111						HDF	HDF	HDF	HDF	HDF	9/9/12	253	01:48:59.98	00:00:05.00	01:49:04.98	01:49:07.07	CW	1.6602-1.7578	0.494	137.161	8.00	2.72	
12	1212						HDF	HDF	HDF	HDF	HDF	9/9/12	253	01:52:11.01	00:00:03.00	01:52:14.01	01:52:15.90	CW	1.6602	0.339	147.619	22.20	2.55	
13							HDF	HDF	HDF	HDF	HDF	9/9/12	253	01:57:18.50	00:00:08.40	01:57:26.90	01:57:04.31	CW	1.6602	0.439	134.618	12.70	2.41	
14	1414						HDF	HDF	HDF	HDF	HDF	9/9/12	253	02:05:33.19	00:00:05.00	02:05:38.19	02:05:40.98	CW	1.6602-1.7578	0.325	136.281	18.50	2.49	
15	1515						HDF	HDF	HDF	HDF	HDF	9/9/12	253	02:12:45.08	00:00:05.00	02:12:50.08	02:12:28.52	CW	1.6602-1.7578	0.392	138.315	7.60	3.91	
16	1616						HDF	HDF	HDF	HDF	HDF	9/9/12	253	02:19:04.90	00:00:05.00	02:19:09.90	02:19:12.69	CW	1.6602-1.7578	0.343	134.421	16.70	2.80	
17	1717						HDF	HDF	HDF	HDF	HDF	9/9/12	253	02:24:24.86	00:00:02.78	02:24:27.64	02:24:21.57	CW	1.7578	0.350	134.409	14.30	2.65	
18	1818						HDF	HDF	HDF	HDF	HDF	9/9/12	253	02:43:25.82	00:00:03.50	02:43:28.82	02:43:21.16	CW	1.6602-1.7578	0.334	136.680	21.40	3.28	
19	1919						HDF	HDF	HDF	HDF	HDF	9/9/12	253	02:50:02.47	00:00:03.00	02:50:05.47	02:49:58.06	CW	1.6602-1.7578	0.327	135.516	29.70	2.51	
20	2020						HDF	HDF	HDF	HDF	HDF	9/9/12	253	03:02:40.94	00:00:04.00	03:02:44.94	03:02:36.64	CW	1.6602-1.7578	0.417	169.992	20.70	4.44	
21							HDF	HDF	HDF	HDF	HDF	9/9/12	253	03:32:44.94	00:00:04.00	03:32:48.94	03:32:36.64	CW	1.6602-1.7578	0.417	169.992	20.70	4.44	
22							HDF	HDF	HDF	HDF	HDF	9/9/12	253	03:38:32.82	00:00:03.68	03:38:36.82	03:38:30.02	CW	1.5625-1.7578	0.339	137.261	11.40	3.88	
23	2424						HDF	HDF	HDF	HDF	HDF	9/9/12	253	04:15:55.49	00:00:04.00	04:16:00.49	04:16:00.04	CW	1.5625-1.7578	0.327	133.771	10.40	3.23	
24	2424						HDF	HDF	HDF	HDF	HDF	9/9/12	253	01:28:13.30	00:00:06.00	01:28:19.90	01:28:20.79	CW	1.6602	0.369	148.181	18.00	3.35	
25	2525						HDF	HDF	HDF	HDF	HDF	9/9/12	253	01:22:53.69	00:00:12.50	01:23:06.19	01:22:39.70	CW	1.6602	0.448	136.766	10.60	1.67	
26							HDF	HDF	HDF	HDF	HDF	9/9/12	253	01:17:34.09	00:00:08.00	01:17:42.09	01:17:25.42	CW	1.6602-1.7578	0.494	149.913	12.60	2.23	
27	77						HDF	HDF	HDF	HDF	HDF	9/9/12	253	01:48:59.98	00:00:05.00	01:49:04.98	01:49:07.07	CW	1.6602-1.7578	0.380	150.593	26.00	3.21	
28	88						HDF	HDF	HDF	HDF	HDF	9/9/12	253	01:50:43.28	00:00:07.00	01:50:50.28	01:50:59.90	CW	1.6602-1.7578	0.278	140.477	2.30	2.18	
29	89						HDF	HDF	HDF	HDF	HDF	9/9/12	253	01:57:18.50	00:00:08.40	01:57:26.90	01:57:04.31	CW	1.6602	0.328	155.202	13.60	2.44	
30							HDF	HDF	HDF	HDF	HDF	9/9/12	253	02:05:33.19	00:00:03.60	02:05:38.19	02:05:40.98	CW	1.6602-1.7578	0.470	146.725	11.40	2.44	
31	1515						HDF	HDF	HDF	HDF	HDF	9/9/12	253	02:12:45.08	00:00:06.00	02:12:50.08	02:12:28.52	CW	1.6602-1.7578	0.360	156.305	8.80	2.58	
32	1616						HDF	HDF	HDF	HDF	HDF	9/9/12	253	02:19:04.90	00:00:05.00	02:19:09.90	02:19:12.69	CW	1.6602-1.7578	0.425	158.861	29.80	2.84	
33	1717						HDF	HDF	HDF	HDF	HDF	9/9/12	253	02:24:24.86	00:00:03.78	02:24:27.64	02:24:21.57	CW	1.6602-1.7578	0.425	158.861	29.80	2.84	
34							HDF	HDF	HDF	HDF	HDF	9/9/12	253	03:02:40.94	00:00:03.78	03:02:44.94	03:02:36.64	CW	1.6602-1.7578	0.470	169.994	14.10	3.05	
35	1919						HDF	HDF	HDF	HDF	HDF	9/9/12	253	03:32:44.94	00:00:03.50	03:32:48.94	03:32:36.64	CW	1.6602	0.315	133.404	16.90	3.73	
36							HDF	HDF	HDF	HDF	HDF	9/9/12	253	04:15:55.49	00:00:03.50	04:16:00.49	04:15:59.49	CW	1.6602	0.334	136.315	24.90	3.86	
37	38						HDF	HDF	HDF	HDF	HDF	9/9/12	253	07:05:07.50	00:00:06.00	07:05:13.50	07:05:21.70	CW	1.6602	0.334	136.315	24.90	3.86	
38	39						HDF	HDF	HDF	HDF	HDF	9/9/12	253	08:15:59.50	00:00:01.50	08:15:59.50	08:16:00.00	IMP	1.6625-16.4062	0.717	174.857	22.80	2.39	
39							HDF	HDF	HDF	HDF	HDF	9/9/12	253	08:22:36.30	00:00:04.60	08:22:40.90	08:22:42.30	CW	1.6625-1.7578	0.323	132.637	30.50	5.49	
40	41						HDF	HDF	HDF	HDF	HDF	9/9/12	253	08:22:36.30	00:00:04.60	08:22:40.90	08:22:42.30	CW	1.6625-1.7578	0.529	164.228	12.40	4.28	
41	42						HDF	HDF	HDF	HDF	HDF	9/9/12	253	08:00:29.10	00:00:07.50	08:00:36.60	08:00:47.90	CW	1.6602	0.315	133.695	45.00	5.98	
42	43						HDF	HDF	HDF	HDF	HDF	9/9/12	253	08:00:29.10	00:00:07.50	08:00:36.60	08:00:47.90	CW	1.6602	0.325	154.592	35.70	5.07	
43	44						HDF	HDF	HDF	HDF	HDF	9/9/12	253	09:02:38.50	00:00:01.50	09:02:38.50	09:02:41.40	IMP	1-3.5156	0.327	126.870	23.10	3.75	
44	45						HDF	HDF	HDF	HDF	HDF	9/9/12	253	10:12:57.10	00:00:04.00	10:12:57.10	10:12:48.10	CW	1.5625-1.7578	0.378	153.838	51.80	3.88	
45	46						HDF	HDF	HDF	HDF	HDF	9/9/12	253	11:04:03.30	00:00:01.00	11:04:03.30	11:04:03.30	IMP	2.3436-6.6438	0.926	130.913	30.00	3.22	
46	47						HDF	HDF	HDF	HDF	HDF	9/9/12	253	11:04:03.30	00:00:01.00	11:04:03.30	11:04:03.30	IMP	1.6602	0.350	130.913	30.00	3.22	
47	48						HDF	HDF	HDF	HDF	HDF	9/9/12	253	11:03:58.44	00:00:05.25	11:04:03.69	11:04:03.31	CW	1.6602	0.460	157.043	52.80	3.89	
48	49						HDF	HDF	HDF	HDF	HDF	9/9/12	253	11:12:51.22	00:00:04.40	11:12:55.62	11:12:56.89	CW	1.6602-1.7578	0.388	154.125	49.60	6.17	
49	50						HDF	HDF	HDF	HDF	HDF	9/9/12	253	11:21:31.21	00:00:01.75	11:21:32.96	11:21:31.21	IMP	1-3.9062	0.356	132.597	28.50	3.23	
50	51						HDF	HDF	HDF	HDF	HDF	9/9/12	253	12:22:33.21	00:00:01.75	12:22:34.96	12:22:36.61	IMP	1.6602	0.315	130.030	12.90	3.76	
51	52						HDF	HDF	HDF	HDF	HDF	9/9/12	253	12										



ID	Related ID	BOZE	BOZW	COLL	FINC	PERK	MOOD1	MOOD2	MOOD3	MOOD4	MOOD5	Date	Julian Day	Start time	Duration	End time	Noise Start time	Event type	Frequencies (Hz)	Apparent Velocity (km/sec)	Azimuth	F-stat	SNR
145							HDF	HDF	HDF	HDF	HDF	10/31/12	305	04:44:20.50	00:00:04.30	04:44:24.80	04:44:25.10	CW	1.5625-1.7578	0.379	165.671	8.10	2.29
146							HDF	HDF	HDF	HDF	HDF	10/31/12	305	05:32:28.10	00:00:04.10	05:32:32.20	05:32:32.90	CW	1.5625-1.7578	0.366	154.737	9.90	3.72
147							HDF	HDF	HDF	HDF	HDF	10/31/12	305	07:00:34.40	00:00:05.20	07:00:39.60	07:00:34.40	CW	1.5625-1.6602	0.356	155.871	9.50	3.51
148	149						HDF	HDF	HDF	HDF	HDF	10/31/12	305	07:00:25.90	00:00:05.20	07:00:31.10	07:00:34.40	CW	1.5625-1.6602	0.351	155.871	9.50	3.51
149	148						HDF	HDF	HDF	HDF	HDF	10/31/12	305	07:00:25.90	00:00:05.20	07:00:31.10	07:00:34.40	CW	1.5625-1.6602	0.351	155.871	9.50	3.51
150							HDF	HDF	HDF	HDF	HDF	10/31/12	305	08:32:49.20	00:00:06.00	08:32:55.20	08:32:49.20	CW	1.5625-1.6602	0.348	137.108	16.60	3.19
151							HDF	HDF	HDF	HDF	HDF	10/31/12	305	08:32:49.20	00:00:06.00	08:32:55.20	08:32:49.20	CW	1.5625-1.6602	0.348	137.108	16.60	3.19
152							HDF	HDF	HDF	HDF	HDF	10/31/12	305	08:32:49.20	00:00:06.00	08:32:55.20	08:32:49.20	CW	1.5625-1.6602	0.348	137.108	16.60	3.19
153							HDF	HDF	HDF	HDF	HDF	10/31/12	305	09:19:26.00	00:00:01.50	09:19:27.50	09:19:26.00	IMP	1.6602-1.7578	0.322	153.455	29.60	3.52
154							HDF	HDF	HDF	HDF	HDF	10/31/12	305	09:19:26.00	00:00:01.50	09:19:27.50	09:19:26.00	IMP	1.6602-1.7578	0.322	153.455	29.60	3.52
155							HDF	HDF	HDF	HDF	HDF	10/31/12	305	15:59:36.70	00:00:06.00	15:59:42.70	15:59:36.70	CW	1.0000-3.0000	0.306	136.204	23.60	2.21
156							HDF	HDF	HDF	HDF	HDF	10/31/12	305	15:59:36.70	00:00:06.00	15:59:42.70	15:59:36.70	CW	1.0000-3.0000	0.306	136.204	23.60	2.21
157							HDF	HDF	HDF	HDF	HDF	10/31/12	305	16:41:05.30	00:00:06.10	16:41:11.40	16:41:05.30	CW	1.5625-1.6602	0.401	163.484	23.90	3.98
158							HDF	HDF	HDF	HDF	HDF	10/31/12	305	16:42:02.30	00:00:06.10	16:42:08.40	16:42:02.30	CW	1.6602	4.992	333.690	32.80	4.19
159							HDF	HDF	HDF	HDF	HDF	10/31/12	305	17:08:56.90	00:00:03.30	17:09:00.20	17:08:56.90	IMP	0.6000-1.5000	0.473	339.228	46.30	4.24
160							HDF	HDF	HDF	HDF	HDF	10/31/12	305	17:08:56.90	00:00:03.30	17:09:00.20	17:08:56.90	IMP	0.6000-1.5000	0.473	339.228	46.30	4.24
161							HDF	HDF	HDF	HDF	HDF	10/31/12	305	18:47:51.20	00:00:04.00	18:47:55.20	18:47:51.20	IMP	1.6602	1.079	340.750	16.90	4.24
162							HDF	HDF	HDF	HDF	HDF	10/31/12	305	18:47:51.20	00:00:04.00	18:47:55.20	18:47:51.20	IMP	1.6602	1.079	340.750	16.90	4.24
163							HDF	HDF	HDF	HDF	HDF	10/31/12	305	20:08:59.00	00:00:05.00	20:09:04.00	20:08:59.00	OTH	0.4000-3.4000	0.344	205.968	6.50	9.92
164							HDF	HDF	HDF	HDF	HDF	10/31/12	305	20:08:59.00	00:00:05.00	20:09:04.00	20:08:59.00	OTH	0.4000-3.4000	0.344	205.968	6.50	9.92
165							HDF	HDF	HDF	HDF	HDF	10/31/12	305	21:25:14.10	00:00:02.40	21:25:16.50	21:25:16.90	OTH	4.6875-5.0781	0.358	243.069	32.00	44.19
166							HDF	HDF	HDF	HDF	HDF	10/31/12	305	21:25:14.10	00:00:02.40	21:25:16.50	21:25:16.90	OTH	4.6875-5.0781	0.358	243.069	32.00	44.19
167	168						HDF	HDF	HDF	HDF	HDF	10/31/12	305	22:07:59.00	00:00:07.50	22:08:06.50	22:07:59.00	CW	1.5625-1.7578	0.393	134.384	8.70	2.90
168	167						HDF	HDF	HDF	HDF	HDF	10/31/12	305	22:07:59.00	00:00:07.50	22:08:06.50	22:07:59.00	CW	1.5625-1.7578	0.393	134.384	8.70	2.90
169							HDF	HDF	HDF	HDF	HDF	10/31/12	305	22:34:32.10	00:00:02.80	22:34:34.90	22:34:32.10	CW	1.5625-1.7578	0.387	152.038	8.50	2.49
170							HDF	HDF	HDF	HDF	HDF	10/31/12	305	22:34:32.10	00:00:02.80	22:34:34.90	22:34:32.10	CW	1.5625-1.7578	0.387	152.038	8.50	2.49
171							HDF	HDF	HDF	HDF	HDF	10/31/12	305	23:35:29.80	00:00:02.00	23:35:31.80	23:35:29.80	IMP	2.3438-4.6923	0.367	171.652	7.80	3.63
172							HDF	HDF	HDF	HDF	HDF	10/31/12	305	23:35:29.80	00:00:02.00	23:35:31.80	23:35:29.80	IMP	2.3438-4.6923	0.367	171.652	7.80	3.63
173							HDF	HDF	HDF	HDF	HDF	10/31/12	305	23:58:15.40	00:00:06.20	23:58:21.60	23:58:15.40	CW	1.5625-1.7578	0.372	204.734	10.20	3.99
174							HDF	HDF	HDF	HDF	HDF	10/31/12	305	23:58:15.40	00:00:06.20	23:58:21.60	23:58:15.40	CW	1.5625-1.7578	0.372	204.734	10.20	3.99
175							HDF	HDF	HDF	HDF	HDF	10/31/12	305	01:00:42.60	00:00:04.50	01:00:47.10	01:00:42.60	CW	1.7578	0.486	138.071	24.60	2.52
176							HDF	HDF	HDF	HDF	HDF	10/31/12	305	01:00:42.60	00:00:04.50	01:00:47.10	01:00:42.60	CW	1.7578	0.486	138.071	24.60	2.52
177							HDF	HDF	HDF	HDF	HDF	10/31/12	305	03:28:39.80	00:00:05.00	03:28:44.80	03:28:39.80	CW	1.7578	0.401	158.436	5.70	1.10
178							HDF	HDF	HDF	HDF	HDF	10/31/12	305	03:28:39.80	00:00:05.00	03:28:44.80	03:28:39.80	CW	1.7578	0.401	158.436	5.70	1.10
179	180						HDF	HDF	HDF	HDF	HDF	10/31/12	305	10:08:48.00	00:00:16.00	10:08:47.70	10:08:48.00	CW	1.709	0.334	150.402	7.10	3.27
180	179						HDF	HDF	HDF	HDF	HDF	10/31/12	305	10:08:48.00	00:00:16.00	10:08:47.70	10:08:48.00	CW	1.709	0.334	150.402	7.10	3.27
181	183						HDF	HDF	HDF	HDF	HDF	10/31/12	305	11:19:25.10	00:00:09.50	11:19:25.10	11:19:25.30	CW	1.7578	0.685	122.179	3.90	1.51
182	184						HDF	HDF	HDF	HDF	HDF	10/31/12	305	11:19:25.10	00:00:09.50	11:19:25.10	11:19:25.30	CW	1.7578	0.685	122.179	3.90	1.51
183	186						HDF	HDF	HDF	HDF	HDF	10/31/12	305	12:14:37.50	00:00:19.20	12:14:37.50	12:14:37.50	OTH	0.1000-0.3000	0.393	146.136	12.30	2.77
184	186						HDF	HDF	HDF	HDF	HDF	10/31/12	305	12:14:37.50	00:00:19.20	12:14:37.50	12:14:37.50	OTH	0.1000-0.3000	0.393	146.136	12.30	2.77
185	184						HDF	HDF	HDF	HDF	HDF	10/31/12	305	13:26:36.70	00:00:19.00	13:26:36.70	13:26:36.70	OTH	0.8000-1.7000	0.807	167.053	2.70	1.31
186	184						HDF	HDF	HDF	HDF	HDF	10/31/12	305	13:26:36.70	00:00:19.00	13:26:36.70	13:26:36.70	OTH	0.8000-1.7000	0.807	167.053	2.70	1.31
187							HDF	HDF	HDF	HDF	HDF	10/31/12	305	15:28:43.50	00:00:07.60	15:28:43.50	15:28:43.50	CW	1.6602	0.386	170.437	8.80	3.46
188							HDF	HDF	HDF	HDF	HDF	10/31/12	305	15:28:43.50	00:00:07.60	15:28:43.50	15:28:43.50	CW	1.6602	0.386	170.437	8.80	3.46
189							HDF	HDF	HDF	HDF	HDF	10/31/12	305	16:37:22.40	00:00:14.20	16:37:22.40	16:37:22.40	CW	1.6602-1.7578	0.533	155.521	7.80	1.93
190							HDF	HDF	HDF	HDF	HDF	10/31/12	305	16:37:22.40	00:00:14.20	16:37:22.40	16:37:22.40	CW	1.6602-1.7578	0.533	155.521	7.80	1.93
191							HDF	HDF	HDF	HDF	HDF	10/31/12	305	17:04:31.70	00:00:29.30	17:04:31.70	17:04:31.70	CW	1.6602-1.7578	0.477	146.902	8.00	3.26
192							HDF	HDF	HDF	HDF	HDF	10/31/12	305	17:04:31.70	00:00:29.30	17:04:31.70	17:04:31.70	CW	1.6602-1.7578	0.477	146.902	8.00	3.26
193							HDF	HDF	HDF	HDF	HDF	10/31/12	305	18:42:53.50	00:00:14.00	18:42:53.50	18:42:53.50	CW	1.709	0.517	147.907	7.60	2.89
194							HDF	HDF	HDF	HDF	HDF	10/31/12	305	18:42:53.50	00:00:14.00	18:42:53.50	18:42:53.50	CW	1.709	0.517	147.907	7.60	2.89
195							HDF	HDF	HDF	HDF	HDF	10/31/12	305	19:49:11.80	00:00:06.00	19:49:11.80	19:49:11.80	CW	1.6602-1.7578	0.471	145.206	17.50	2.39
196							HDF	HDF	HDF	HDF	HDF	10/31/12	305	19:49:11.80	00:00:06.00	19:49:11.80	19:49:11.80	CW	1.6602-1.7578	0.471	145.206	17.50	2.39
197	198						HDF	HDF	HDF	HDF	HDF	10/31/12	305	20:41:30.40	00:00:07.00	20:41:37.40	20:41:37.80	OTH	0.7812-5.1758	0.344	119.729	38.70	10.29
198	197						HDF	HDF	HDF	HDF	HDF	10/31/12	305	20:41:30.40	00:00:07.00	20:41:37.40	20:41:37.80	OTH	0.7812-5.1758	0.344	119.729	38.70	10.29
199							HDF	HDF	HDF	HDF	HDF	10/31/12	305	21:01:29.60	00:00:09.00	21:01:29.60	21:01:29.60	CW	1.7578	0.823	100.539	6.40	1.68
200							HDF	HDF	HDF	HDF	HDF	10/31/12	305	21:01:29.60	00:00:09.00	21:01:29.60	21:01:29.60	CW	1.7578	0.823	100.539	6.40</	



ID	Related ID	BOZE	BOZW	COLL	FINC	PERK	MOOD1	MOOD2	MOOD3	MOOD4	MOOD5	Date	Julian Day	Start time	Duration	End time	Noise Start time	Event type	Frequencies (Hz)	Apparent Velocity (km/sec)	Azimuth	F-stat	SNR
309	308	HDF	HDF	HDF	HDF	HDF	HDF	HDF	HDF	HDF	HDF	8/15/12	228	20:03:41.40	00:00:05.00	20:03:46.40	20:30:46.60	CW	1.5625-1.7578	0.368	141.432	12.70	2.88
310		HDF	HDF	HDF	HDF	HDF	HDF	HDF	HDF	HDF	HDF	8/15/12	228	21:23:09.30	00:00:05.00	21:23:09.30	21:23:09.30	CW	1.7578	0.394	156.100	16.40	2.21
311		HDF	HDF	HDF	HDF	HDF	HDF	HDF	HDF	HDF	HDF	8/15/12	228	22:25:48.60	00:00:05.00	22:25:48.60	22:25:48.60	CW	1.6602	0.416	149.526	16.30	2.66
312		HDF	HDF	HDF	HDF	HDF	HDF	HDF	HDF	HDF	HDF	8/15/12	228	23:25:48.90	00:00:05.00	23:25:48.90	23:25:48.90	CW	1.6602	0.360	149.526	16.30	2.66
313		HDF	HDF	HDF	HDF	HDF	HDF	HDF	HDF	HDF	HDF	8/15/12	135	02:41:02.80	00:00:07.00	02:41:09.80	02:41:09.80	CW	1.7578	0.309	135.522	2.90	1.88
314		HDF	HDF	HDF	HDF	HDF	HDF	HDF	HDF	HDF	HDF	8/15/12	135	03:26:46.90	00:00:14.00	03:27:00.90	03:27:00.90	CW	1.6602	0.333	134.626	7.40	2.54
315		HDF	HDF	HDF	HDF	HDF	HDF	HDF	HDF	HDF	HDF	8/15/12	135	05:36:50.00	00:00:04.00	05:36:54.00	05:36:54.00	CW	1.5625-1.7578	0.307	130.681	6.80	1.61
316		HDF	HDF	HDF	HDF	HDF	HDF	HDF	HDF	HDF	HDF	8/15/12	135	14:45:53.00	00:00:06.00	14:45:59.00	14:46:01.60	CW	1.6602	0.379	141.189	2.30	1.49
317		HDF	HDF	HDF	HDF	HDF	HDF	HDF	HDF	HDF	HDF	8/15/12	135	01:24:34.80	00:00:07.00	01:24:34.80	01:24:34.80	CW	1.6648	0.687	164.505	5.10	1.39
318		HDF	HDF	HDF	HDF	HDF	HDF	HDF	HDF	HDF	HDF	8/15/12	060	02:31:46.30	00:00:07.00	02:31:54.30	02:31:54.30	CW	1.6602	0.412	168.690	2.10	1.73
319		HDF	HDF	HDF	HDF	HDF	HDF	HDF	HDF	HDF	HDF	8/15/12	060	02:31:59.10	00:00:05.00	02:32:04.10	02:32:08.80	CW	1.6602	0.412	153.875	6.70	2.88
320		HDF	HDF	HDF	HDF	HDF	HDF	HDF	HDF	HDF	HDF	8/15/12	060	03:16:45.30	00:00:07.00	03:16:52.30	03:16:52.30	CW	1.5625-1.6602	0.580	163.610	4.20	1.45
321	323	HDF	HDF	HDF	HDF	HDF	HDF	HDF	HDF	HDF	HDF	8/15/12	060	03:22:52.20	00:00:07.00	03:23:01.20	03:23:01.20	CW	1.5625-1.6602	0.313	128.710	5.00	2.70
322	322	HDF	HDF	HDF	HDF	HDF	HDF	HDF	HDF	HDF	HDF	8/15/12	060	04:11:38.20	00:00:05.00	04:11:44.20	04:11:44.20	CW	1.6602	0.416	162.810	9.10	1.90
323		HDF	HDF	HDF	HDF	HDF	HDF	HDF	HDF	HDF	HDF	8/15/12	060	04:37:01.40	00:00:05.00	04:37:01.40	04:37:01.40	CW	1.5625-1.7578	0.381	165.140	19.80	3.22
324		HDF	HDF	HDF	HDF	HDF	HDF	HDF	HDF	HDF	HDF	8/15/12	060	04:59:31.50	00:00:08.00	04:59:39.50	04:59:39.50	CW	1.5625-1.6602	0.403	155.875	8.80	3.51
325	326	HDF	HDF	HDF	HDF	HDF	HDF	HDF	HDF	HDF	HDF	8/15/12	060	05:11:33.40	00:00:04.00	05:11:33.40	05:11:33.40	CW	1.5625	0.520	148.178	11.90	2.23
326	327	HDF	HDF	HDF	HDF	HDF	HDF	HDF	HDF	HDF	HDF	8/15/12	060	05:18:03.30	00:00:05.00	05:18:03.30	05:18:03.30	CW	1.5625	0.413	151.966	20.30	3.86
327	326	HDF	HDF	HDF	HDF	HDF	HDF	HDF	HDF	HDF	HDF	8/15/12	060	07:08:14.40	00:00:17.00	07:08:31.40	07:08:32.00	CW	1.5625-1.6113	0.297	133.163	14.50	4.69
328	328	HDF	HDF	HDF	HDF	HDF	HDF	HDF	HDF	HDF	HDF	8/15/12	060	08:56:01.90	00:00:07.60	08:56:09.50	08:56:09.50	CW	1.5625-1.6113	0.407	161.873	12.40	4.13
329	328	HDF	HDF	HDF	HDF	HDF	HDF	HDF	HDF	HDF	HDF	8/15/12	060	08:56:01.90	00:00:07.60	08:56:09.50	08:56:09.50	CW	1.5625-1.6602	0.310	134.301	16.40	4.10
330	329	HDF	HDF	HDF	HDF	HDF	HDF	HDF	HDF	HDF	HDF	8/15/12	060	09:58:21.00	00:00:09.00	09:58:30.00	09:58:30.00	CW	1.5625-1.6602	0.342	161.986	15.10	5.01
331	331	HDF	HDF	HDF	HDF	HDF	HDF	HDF	HDF	HDF	HDF	8/15/12	060	10:51:20.20	00:00:05.00	10:51:20.20	10:51:20.20	CW	1.5625	0.342	164.624	17.60	4.66
332	332	HDF	HDF	HDF	HDF	HDF	HDF	HDF	HDF	HDF	HDF	8/15/12	060	10:51:20.20	00:00:05.00	10:51:20.20	10:51:20.20	CW	1.5625	0.304	131.915	21.40	3.91
333	334	HDF	HDF	HDF	HDF	HDF	HDF	HDF	HDF	HDF	HDF	8/15/12	060	11:45:05.00	00:00:08.00	11:45:14.00	11:45:14.00	CW	1.5625-1.6602	0.384	160.017	53.30	3.42
334	333	HDF	HDF	HDF	HDF	HDF	HDF	HDF	HDF	HDF	HDF	8/15/12	060	11:45:05.00	00:00:08.00	11:45:14.00	11:45:14.00	CW	1.5625-1.6602	0.296	133.002	21.90	3.14
335	335	HDF	HDF	HDF	HDF	HDF	HDF	HDF	HDF	HDF	HDF	8/15/12	060	12:34:42.70	00:00:14.00	12:34:42.70	12:34:42.70	CW	1.5625-1.6602	0.341	158.048	39.90	3.15
336	336	HDF	HDF	HDF	HDF	HDF	HDF	HDF	HDF	HDF	HDF	8/15/12	060	13:07:19.40	00:00:05.00	13:07:19.40	13:07:19.40	CW	1.5625	0.358	155.863	31.30	2.76
337	338	HDF	HDF	HDF	HDF	HDF	HDF	HDF	HDF	HDF	HDF	8/15/12	060	13:07:19.40	00:00:05.00	13:07:19.40	13:07:19.40	CW	1.5625	0.306	133.628	20.30	2.78
338	337	HDF	HDF	HDF	HDF	HDF	HDF	HDF	HDF	HDF	HDF	8/15/12	060	14:34:26.70	00:00:05.00	14:34:32.10	14:34:32.10	OTH	1.5625	0.405	156.759	35.10	2.92
339	340	HDF	HDF	HDF	HDF	HDF	HDF	HDF	HDF	HDF	HDF	8/15/12	060	14:48:39.50	00:00:05.00	14:48:42.50	14:48:42.50	OTH	0.3906-0.9766	0.800	335.714	12.00	2.27
340	339	HDF	HDF	HDF	HDF	HDF	HDF	HDF	HDF	HDF	HDF	8/15/12	060	15:07:56.60	00:00:03.00	15:08:01.60	15:08:02.30	OTH	0.1953-0.9766	0.312	330.101	13.60	3.25
341	342	HDF	HDF	HDF	HDF	HDF	HDF	HDF	HDF	HDF	HDF	8/15/12	060	15:07:56.60	00:00:03.00	15:08:01.60	15:08:02.30	OTH	0.3906-0.9766	0.788	323.095	9.70	2.74
342	341	HDF	HDF	HDF	HDF	HDF	HDF	HDF	HDF	HDF	HDF	8/15/12	060	15:10:31.50	00:00:04.00	15:10:35.50	15:10:36.10	IMP	0.7812-2.7384	0.362	331.758	9.00	2.96
343	343	HDF	HDF	HDF	HDF	HDF	HDF	HDF	HDF	HDF	HDF	8/15/12	060	15:10:31.50	00:00:04.00	15:10:35.50	15:10:36.10	IMP	0.3906-1.3672	0.316	320.870	16.50	3.15
344	343	HDF	HDF	HDF	HDF	HDF	HDF	HDF	HDF	HDF	HDF	8/15/12	060	16:01:48.40	00:00:03.30	16:01:51.70	16:01:52.10	IMP	1.5625-1.6602	0.378	153.435	9.70	3.15
345	345	HDF	HDF	HDF	HDF	HDF	HDF	HDF	HDF	HDF	HDF	8/15/12	060	17:22:31.50	00:00:05.00	17:22:36.90	17:22:36.90	IMP	1.5625-1.7578	0.429	325.931	8.30	5.24
346	346	HDF	HDF	HDF	HDF	HDF	HDF	HDF	HDF	HDF	HDF	8/15/12	060	17:22:31.50	00:00:05.00	17:22:36.90	17:22:36.90	IMP	1.5625-1.7578	0.435	136.988	18.90	3.21
347	347	HDF	HDF	HDF	HDF	HDF	HDF	HDF	HDF	HDF	HDF	8/15/12	060	17:29:38.40	00:00:02.00	17:29:40.40	17:29:41.10	IMP	1.5625-6.6406	0.417	191.701	6.80	3.21
348	348	HDF	HDF	HDF	HDF	HDF	HDF	HDF	HDF	HDF	HDF	8/15/12	060	17:29:38.40	00:00:02.00	17:29:40.40	17:29:41.10	IMP	1.9531-6.6406	0.334	201.801	24.80	3.85
349	350	HDF	HDF	HDF	HDF	HDF	HDF	HDF	HDF	HDF	HDF	8/15/12	060	17:29:49.60	00:00:01.00	17:29:50.60	17:29:50.60	IMP	1.5625-6.2500	0.359	198.886	36.80	2.10
350	349	HDF	HDF	HDF	HDF	HDF	HDF	HDF	HDF	HDF	HDF	8/15/12	060	17:33:14.20	00:00:03.00	17:33:17.20	17:33:17.20	IMP	1.5625-3.9062	0.452	240.701	9.70	9.25
351	351	HDF	HDF	HDF	HDF	HDF	HDF	HDF	HDF	HDF	HDF	8/15/12	060	17:33:43.10	00:00:05.00	17:33:48.10	17:33:48.10	IMP	0.5659-4.8828	0.446	238.162	24.80	9.56
352	352	HDF	HDF	HDF	HDF	HDF	HDF	HDF	HDF	HDF	HDF	8/15/12	060	17:33:43.10	00:00:05.00	17:33:48.10	17:33:48.10	IMP	0.5659-4.8828	0.406	235.525	50.90	8.88
353	353	HDF	HDF	HDF	HDF	HDF	HDF	HDF	HDF	HDF	HDF	8/15/12	060	17:34:09.40	00:00:02.50	17:34:11.90	17:34:12.50	IMP	1.5625-4.6675	0.423	242.931	18.90	1.67
354	354	HDF	HDF	HDF	HDF	HDF	HDF	HDF	HDF	HDF	HDF	8/15/12	060	18:35:52.90	00:00:07.00	18:35:59.90	18:36:00.60	IMP	1.5625-1.7719	0.391	235.620	10.70	1.22
355	355	HDF	HDF	HDF	HDF	HDF	HDF	HDF	HDF	HDF	HDF	8/15/12	060	18:55:57.60	00:00:06.00	18:56:05.60	18:56:06.10	IMP	1.5625-1.6602	0.462	292.620	44.90	18.54
356	356	HDF	HDF	HDF	HDF	HDF	HDF	HDF	HDF	HDF	HDF	8/15/12	060	21:41:03.30	00:01:00.00	21:42:03.30	21:42:04.40	OTH	1.5625-1.6				

ID	Related ID	BOZE	BOZW	COLL	FINC	PERK	MOOD1	MOOD2	MOOD3	MOOD4	MOOD5	Date	Julian Day	Start time	Duration	End time	Noise Start time	Event type	Frequencies (Hz)	Apparent Velocity (m/sec)	Azimuth	F-stat	SNR
381		HDF	HDF	HDF	HDF	HDF	HDF	HDF	HDF	HDF	HDF	12/01/12	336	05:45:37.60	00:00:04.00	05:45:41.60	05:45:42.20	CW	1.5625-1.7578	0.848	147.995	11.90	1.99
382		HDF	HDF	HDF	HDF	HDF	HDF	HDF	HDF	HDF	HDF	12/01/12	336	07:28:07.10	00:00:06.00	07:28:13.10	07:28:13.60	CW	1.5625-1.6602	0.910	176.379	4.40	1.42
383		HDF	HDF	HDF	HDF	HDF	HDF	HDF	HDF	HDF	HDF	12/01/12	336	10:07:50.00	00:00:05.00	10:07:55.00	10:07:55.80	CW	1.5625-1.6602	0.842	147.995	6.50	1.88
384		HDF	HDF	HDF	HDF	HDF	HDF	HDF	HDF	HDF	HDF	12/01/12	336	12:52:52.50	00:00:06.00	12:52:58.50	12:52:58.80	CW	1.5625-1.6602	0.946	156.473	6.50	1.88
385		HDF	HDF	HDF	HDF	HDF	HDF	HDF	HDF	HDF	HDF	12/01/12	336	13:02:43.10	00:00:06.00	13:02:49.10	13:02:49.60	CW	1.5625-1.6602	0.399	163.755	18.60	4.26
386		HDF	HDF	HDF	HDF	HDF	HDF	HDF	HDF	HDF	HDF	12/01/12	336	14:15:32.80	00:00:06.00	14:15:38.80	14:15:39.90	CW	1.5625-1.6602	0.439	144.778	11.60	1.93
387		HDF	HDF	HDF	HDF	HDF	HDF	HDF	HDF	HDF	HDF	12/01/12	336	23:52:04.50	00:00:06.00	23:52:10.50	23:52:11.20	CW	1.5625-1.6602	0.363	152.013	7.40	2.14
388		HDF	HDF	HDF	HDF	HDF	HDF	HDF	HDF	HDF	HDF	9/01/12	245	00:01:34.10	00:00:05.00	00:01:39.10	00:01:39.50	CW	1.6602-1.7578	0.513	169.330	7.30	1.87
389	400	HDF	HDF	HDF	HDF	HDF	HDF	HDF	HDF	HDF	HDF	9/01/12	245	00:01:34.10	00:00:05.00	00:01:39.10	00:01:39.50	CW	1.5625-1.7578	0.330	131.655	25.60	4.01
400	399	HDF	HDF	HDF	HDF	HDF	HDF	HDF	HDF	HDF	HDF	9/01/12	245	00:10:12.80	00:00:33.00	00:10:45.80	00:10:46.50	CW	1.5625-1.7578	0.364	148.639	25.50	3.90
401		HDF	HDF	HDF	HDF	HDF	HDF	HDF	HDF	HDF	HDF	9/01/12	245	01:38:13.10	00:00:08.00	01:38:21.10	01:38:21.60	CW	1.7622-2.578	0.860	75.466	21.40	7.71
402	403	HDF	HDF	HDF	HDF	HDF	HDF	HDF	HDF	HDF	HDF	9/01/12	245	01:38:13.10	00:00:08.00	01:38:21.10	01:38:21.60	CW	1.6602-1.7578	0.837	153.788	25.40	3.12
403		HDF	HDF	HDF	HDF	HDF	HDF	HDF	HDF	HDF	HDF	9/01/12	245	02:14:38.40	00:00:04.00	02:14:42.40	02:14:43.00	CW	1.5625-1.7578	0.327	134.079	22.30	3.01
404	405	HDF	HDF	HDF	HDF	HDF	HDF	HDF	HDF	HDF	HDF	9/01/12	245	02:14:38.40	00:00:04.00	02:14:42.40	02:14:43.00	CW	1.5625-1.7578	0.376	155.308	18.50	2.60
405	404	HDF	HDF	HDF	HDF	HDF	HDF	HDF	HDF	HDF	HDF	9/01/12	245	03:10:20.50	00:00:08.00	03:10:28.50	03:10:29.10	CW	1.6602	0.336	132.921	17.10	3.01
406	407	HDF	HDF	HDF	HDF	HDF	HDF	HDF	HDF	HDF	HDF	9/01/12	245	04:16:10.60	00:00:07.00	04:16:17.60	04:16:17.90	CW	1.6602-1.7578	0.378	150.668	9.90	2.69
407	406	HDF	HDF	HDF	HDF	HDF	HDF	HDF	HDF	HDF	HDF	9/01/12	245	05:01:11.60	00:00:08.00	05:01:19.60	05:01:12.70	IMP	1.6602-1.7578	0.454	161.222	5.10	3.59
408	410	HDF	HDF	HDF	HDF	HDF	HDF	HDF	HDF	HDF	HDF	9/01/12	245	05:01:03.80	00:00:08.00	05:01:11.60	05:01:12.70	IMP	0.6977-1.000	0.323	28.405	17.60	####
409	409	HDF	HDF	HDF	HDF	HDF	HDF	HDF	HDF	HDF	HDF	9/01/12	245	05:01:03.80	00:00:08.00	05:01:11.60	05:01:12.70	IMP	0.6977-1.000	1.765	233.937	2.00	####
410	409	HDF	HDF	HDF	HDF	HDF	HDF	HDF	HDF	HDF	HDF	9/01/12	245	11:04:56.80	00:00:05.00	11:05:01.80	11:05:02.40	CW	1.5625-1.7578	0.388	158.939	7.30	2.68
411	412	HDF	HDF	HDF	HDF	HDF	HDF	HDF	HDF	HDF	HDF	9/01/12	245	11:04:56.80	00:00:05.00	11:05:01.80	11:05:02.40	CW	1.5625-1.7578	0.388	158.939	7.30	2.68
412		HDF	HDF	HDF	HDF	HDF	HDF	HDF	HDF	HDF	HDF	9/01/12	245	11:18:04.80	00:00:06.00	11:18:10.80	11:18:11.20	CW	1.5625-1.7578	0.321	132.291	12.00	3.16
413		HDF	HDF	HDF	HDF	HDF	HDF	HDF	HDF	HDF	HDF	9/01/12	245	12:18:51.70	00:00:04.00	12:18:55.70	12:18:56.00	CW	1.5625-1.7578	0.445	154.385	28.80	2.71
414		HDF	HDF	HDF	HDF	HDF	HDF	HDF	HDF	HDF	HDF	9/01/12	245	13:23:30.40	00:00:04.00	13:23:34.80	13:23:35.40	CW	1.5625-1.7578	0.427	156.935	4.30	3.48
415		HDF	HDF	HDF	HDF	HDF	HDF	HDF	HDF	HDF	HDF	9/01/12	245	17:59:16.10	00:00:03.00	17:59:19.10	17:59:19.40	CW	1.7578	0.331	156.975	4.30	3.28
416		HDF	HDF	HDF	HDF	HDF	HDF	HDF	HDF	HDF	HDF	9/01/12	245	19:02:56.20	00:00:06.00	19:03:04.20	19:03:04.60	CW	1.6602-1.7578	0.345	154.418	14.90	2.87
417		HDF	HDF	HDF	HDF	HDF	HDF	HDF	HDF	HDF	HDF	9/01/12	245	20:57:34.80	00:00:04.00	20:57:38.80	20:57:39.60	CW	1.7578	0.515	162.884	5.70	2.80
418		HDF	HDF	HDF	HDF	HDF	HDF	HDF	HDF	HDF	HDF	9/01/12	245	21:43:43.90	00:00:06.00	21:43:49.90	21:43:50.30	CW	1.6602-1.7578	0.461	162.893	17.90	2.86
419		HDF	HDF	HDF	HDF	HDF	HDF	HDF	HDF	HDF	HDF	9/01/12	245	22:13:50.70	00:00:14.00	22:13:58.70	22:13:52.10	CW	1.7688	0.434	153.890	9.50	2.31
420		HDF	HDF	HDF	HDF	HDF	HDF	HDF	HDF	HDF	HDF	9/01/12	245	22:13:50.70	00:00:14.00	22:13:58.70	22:13:52.10	CW	1.7688	0.434	153.890	9.50	2.31

# REPORT DOCUMENTATION PAGE

*Form Approved*  
**OMB No. 0704-0188**

Public reporting burden for this collection of information is estimated to average 1 hour per response, including the time for reviewing instructions, searching existing data sources, gathering and maintaining the data needed, and completing and reviewing this collection of information. Send comments regarding this burden estimate or any other aspect of this collection of information, including suggestions for reducing this burden to Department of Defense, Washington Headquarters Services, Directorate for Information Operations and Reports (0704-0188), 1215 Jefferson Davis Highway, Suite 1204, Arlington, VA 22202-4302. Respondents should be aware that notwithstanding any other provision of law, no person shall be subject to any penalty for failing to comply with a collection of information if it does not display a currently valid OMB control number. **PLEASE DO NOT RETURN YOUR FORM TO THE ABOVE ADDRESS.**

<b>1. REPORT DATE (DD-MM-YYYY)</b> November 2016		<b>2. REPORT TYPE</b> Report 2 of a series		<b>3. DATES COVERED (From - To)</b>	
<b>4. TITLE AND SUBTITLE</b>  Persistent Monitoring of Urban Infrasound Phenomenology; Report 2: Investigation of Structural Infrasound Signals in an Urban Environment				<b>5a. CONTRACT NUMBER</b>	
				<b>5b. GRANT NUMBER</b>	
				<b>5c. PROGRAM ELEMENT NUMBER</b>	
<b>6. AUTHOR(S)</b> Sarah L. McComas, Michael E. Pace, Henry Diaz-Alvarez, Chris Simpson, and Mihan H. McKenna				<b>5d. PROJECT NUMBER</b> 451182	
				<b>5e. TASK NUMBER</b>	
				<b>5f. WORK UNIT NUMBER</b> J62BH4	
<b>7. PERFORMING ORGANIZATION NAME(S) AND ADDRESS(ES)</b>  U.S. Army Engineer Research and Development Center Geotechnical and Structures Laboratory 3909 Halls Ferry Road Vicksburg, MS 39180-6199				<b>8. PERFORMING ORGANIZATION REPORT NUMBER</b>  ERDC TR-15-5	
<b>9. SPONSORING / MONITORING AGENCY NAME(S) AND ADDRESS(ES)</b> Headquarters, U.S. Army Corps of Engineers Washington, DC 20314-1000				<b>10. SPONSOR/MONITOR'S ACRONYM(S)</b>	
				<b>11. SPONSOR/MONITOR'S REPORT NUMBER(S)</b>	
<b>12. DISTRIBUTION / AVAILABILITY STATEMENT</b> Approved for public release; distribution is unlimited.					
<b>13. SUPPLEMENTARY NOTES</b>					
<b>14. ABSTRACT</b> Historically, infrasound arrays have been deployed in rural environments where anthropological noise sources are limited. As interest in monitoring sources at local distances grows in the infrasound community, it is vital to understand how to monitor infrasound sources in an urban environment. Arrays deployed in urban centers have to overcome the decreased signal-to-noise ratio and the reduced amount of real estate available to deploy an array. To advance the understanding of monitoring infrasound sources in urban environments, local and regional infrasound arrays were deployed on rooftops of the campus of Southern Methodist University (SMU) to collect data for one seasonal cycle. The data were evaluated for structural source signals (continuous-wave packets). When a signal was identified, the back azimuth to the source was determined through frequency wavenumber analysis. This information was used to identify hypothesized structural sources; these sources were verified through direct measurement followed by structural numerical modeling. Wave propagation modeling was completed to understand how the urban infrastructure affects infrasound propagation by tying the direct source measurements to the original infrasound observations. The wave propagation study was focused on a single season. This study demonstrated that infrasound arrays deployed in urban environments could detect structural sources with success.					
<b>15. SUBJECT TERMS</b> Acoustics Remote sensing – Data processing			Signal processing - Mathematics Source separation (Signal processing) Cities and towns		Infrasound
<b>16. SECURITY CLASSIFICATION OF:</b>			<b>17. LIMITATION OF ABSTRACT</b>	<b>18. NUMBER OF PAGES</b>  95	<b>19a. NAME OF RESPONSIBLE PERSON</b>
<b>a. REPORT</b> UNCLASSIFIED	<b>b. ABSTRACT</b> UNCLASSIFIED	<b>c. THIS PAGE</b> UNCLASSIFIED			<b>19b. TELEPHONE NUMBER (include area code)</b>